Exploration of the Cold-Wall CVD Synthesis of Monolayer MoS_2 and WS_2

by

Chad Lunceford

A Dissertation Presented in Partial Fulfillment
of the Requirements for the Degree
Doctor of Philosophy

Approved June 2019 by the
Graduate Supervisory Committee:

Jeff Drucker, Chair
David Smith
José Menéndez
Peter Rez

ARIZONA STATE UNIVERSITY

August 2019

ABSTRACT

A highly uniform and repeatable method for synthesizing the single-layer transition metal dichalcogenides (TMDs) molybdenum disulfide, MoS_2, and tungsten disulfide, WS_2, was developed. This method employed chemical vapor deposition (CVD) of precursors in a custom built cold-wall reaction chamber designed to allow independent control over the growth parameters. Iterations of this reaction chamber were employed to overcome limitations to the growth method. First, molybdenum trioxide, MoO_3, and S were co-evaporated from alumina coated W baskets to grow MoS_2 on SiO_2/Si substrates. Using this method, films were found to have repeatable coverage, but unrepeatable morphology. Second, the reaction chamber was modified to include a pair of custom bubbler delivery systems to transport diethyl sulfide (DES) and molybdenum hexacarbonyl (MHC) to the substrate as a S and Mo precursors. Third, tungsten hexacarbonyl (WHC) replaced MHC as a transition metal precursor for the synthesis of WS_2 on Al_2O_3, substrates. This method proved repeatable in both coverage and morphology allowing the investigation of the effect of varying the flow of Ar, varying the substrate temperature and varying the flux of DES to the sample. Increasing each of these parameters was found to decrease the nucleation density on the sample and, with the exception of the Ar flow, induce multi-layer feature growth. This combination of precursors was also used to investigate the reported improvement in feature morphology when NaCl is placed upstream of the substrate. This was found to have no effect on experiments in the configurations used. A final effort was made to adequately increase the feature size by switching from DES to hydrogen sulfide, H_2S, as a source of S. Using H_2S and WHC to grow WS_2 films on Al_2O_3, it was found that increasing the substrate

temperature and increasing the H_2S flow both decrease nucleation density. Increasing the H_2S flow induced bi-layer growth. Ripening of synthesized WS_2 crystals was demonstrated to occur when the sample was annealed, post-growth, in an Ar, H_2, and H_2S flow. Finally, it was verified that the final H_2S and WHC growth method yielded repeatability and uniformity matching, or improving upon, the other methods and precursors investigated.

ACKNOWLEDGMENTS

I would like to start this acknowledgement by thanking Jim Forsman, adjunct physics and astronomy instructor at Paradise Valley Community College, for going off-curriculum so we could spend half a semester building a particle detector in Phy 101. That invaluable experience introduced me to what it was to be a physicist (I was an English major at the time). I would also like to thank the other extraordinary professors I have had along the way: Casey Durandet, who guided my early steps and gave me tons of great material to learn; Steven Nicoloff, who to date is the best math teacher I've had; and Steve Desche, who got me programming in my first research role.

Of course, this document would not be possible without the years of support, guidance, instruction and assistance from my advisor, Jeff Drucker. TA-ing for him, working with him as an undergraduate and then as a graduate student, I have known Dr. Drucker for a long time. Over that time, I like to think I was able to learn his F.W.I.T.I.W. attitude, his "get the manual and take it apart" approach and his tireless tenacity for progressing the field in meaningful ways. A big thank you to him. I would also like to thank my lab mates over the years: Mark Wirth, Dexin Kong, Somilkumar Rathi, Emmanuel Borcean and Shantanu Das.

Thanks are also owed to the army of individuals on hand, maintaining tools, providing guidance and sometimes, just a laugh. I would like to thank Christian Poweleit, David Wright, Tim Karcher, Mark Mangus, Diana Convey, Stefen Myhajlenko, Carrie Sinclair, and Axel Whittmann. I would specifically like to thank David Wright for all furnaces, none of which he ever got back.

I am also grateful to Neal Woodbury for the opportunity he gave me to use lasers on photosynthetic bacteria. Though I returned to materials research, I learned a great deal under his advisement and from that experience. From my time there, I would also like to thank the time-resolved laser spectroscopy expert, Su Lin, my lab mate at the time, Brent Driscoll, and the many others there that assisted in my efforts.

Most importantly, I would like to thank my family: my two wonderful parents, Russell and Alicann, who helped in every way they could, every step of the way; my incredible kids, Mykala and Jace, that amaze me on daily basis; and the unmistakably best of the two of us, my wife, Myken. This really couldn't have happened without her support and encouragement along the way.

Finally, I acknowledge the funding for this research. Portions of this work were supported by a seed grant from the College of Liberal Arts and Sciences at Arizona State University. Additional support was provided by the National Science Foundation under Grant No. DMR-1409280.

TABLE OF CONTENTS

Page

LIST OF TABLES ix

LIST OF FIGURES.. x

CHAPTER

1 INTRODUCTION 1

1.1 Introduction to 2D Materials 2

1.2 Introduction to TMDs 4

1.3 Properties of MoS_2 and WS_2 8

1.4 Current Synthesis Methods 10

1.4.1 Mechanical Exfoliation 10

1.4.2 Hot-Wall CVD 13

1.4.3 Other Methods: Dip Coating Thermolysis, MBE, ALD and Cold-Wall CVD 17

1.5 Importance of Understanding and Controlling Growth 18

1.6 Dissertation Layout 20

2 ANALYTICAL METHODS USED THROUGHOUT 22

2.1 Atomic Force Microscopy 22

2.2 Scanning Electron Microscopy 26

2.3 Rutherford Backscattering Spectrometry 31

2.4 Raman and Photoluminescence Spectroscopy 34

2.5 Auger Electron Spectroscopy 37

3 SYNTHESIS OF MoS_2 USING MoO_3 and S 40

Chapter Page

3.1 Experimental Methods 40

3.1.1 Chamber Configuration 40

3.1.2 Sample Preparation 45

3.1.3 Growth Parameters and Procedure 45

3.1.4 Characterization Methods Used 47

3.2 Results and Discussion 49

3.3 Limitations and Motivation for Configuration Change 68

4 SYNTHESIS OF MoS_2 USING MoO_3, MHC and DES 70

4.1 Experimental Methods 71

4.1.1 Chamber Configuration 71

4.1.1.1 'Bubbler' System for Delivery of Source Vapors 71

4.1.1.2 Implementation of the 'Bubbler' System 74

4.1.1.3 Addition of MHC 76

4.1.1.4 Preparation and Cooling of Precursors 78

4.1.1.5 Automation of the Growth Process 81

4.1.2 Sample Preparation and Heating 83

4.1.3 Growth Preparation, Parameters and Procedure 91

4.2 Results and Discussion 95

4.3 Limitations and Motivation for Configuration Change 98

5 SYNTHESIS OF WS_2 USING WHC and DES 100

5.1 Experimental Methods 100

5.1.1 Switch from MHC to WHC 101

Chapter Page

5.1.2 Use of Cold-Bath Chillers 101

5.1.3 Addition of NaCl to the Gas Inlet 103

5.1.4 Growth Preparation, Parameters and Procedure 103

5.1.5 Characterization Methods Used 105

5.2 Results and Discussion 106

5.3 Limitations and Motivation for Configuration Change 118

6 SYNTHESIS OF WS_2 USING WHC and H_2S 120

6.1 Experimental Methods 120

6.1.1 Switch from DES to H_2S 121

6.1.2 Updates to the LabVIEW Control Program 123

6.1.3 New Heater Design 123

6.1.4 Growth Procedure and Parameters 129

6.1.5 Characterization Methods Used 132

6.2 Results and Discussion 133

6.3 Conclusion 143

7 CONCLUSIONS AND FUTURE WORK 147

REFERENCES 160

APPENDIX

A THERMOELECTRIC-COOLED LIQUID BATH CHILLER CAPABLE OF UNATTENDED OPERATION AT -28 °C 169

A.1 Introduction 170

A.2 Experimental Methods 172

Chapter Page

A.3 Results and Discussion 178

A.4 Conclusion 183

LIST OF TABLES

Table Page

1.1 Lists the Different X-M-X Combinations of TMDs and their Respective Electronic and Magnetic Properties in the Single-Layer 7

3.1 Summary of Coverages Measured by SEM and RBS at the Center of the Substrate, with Average MoS_2 Nanocrystal Size and Nucleation Density for the Samples 61

4.1 Shows the Cold-Bath "Slurry" Solutions Used to Cool the Precursors.................. 81

5.1 Summary of the Percentages of the Sample Covered, Average WS_2 Nanocrystal Size and Nucleation Density for Samples Grown with WHC and DES 118

6.1 Summary of the Percentages of the Sample Covered, Average WS_2 Nanocrystal Size and Nucleation Density for Samples Grown with WHC and H_2S................ 145

LIST OF FIGURES

Figure Page

1.1 Ball-and-Stick Representation of the 1H Crystal Structure of the Transition Metal Dichalcogenide (TMD) MoS_2. Shows the Hexagonal Symmetry of the 1H Structure and Shows the 2H Stacking Structure of Multi-Layer MoS_2 5

1.2 Change in Band Structure of MoS_2 as it is Thinned from Bulk to Single-Layer 9

1.3 Band Structure of MoS_2 at the 6 Corners of the Brillouin Zone 11

1.4 MoS_2 and WS_2 Films Obtained by Mechanical Exfoliation 12

1.5 Typical Schematic of Hot-Wall CVD Synthesis and Characteristic Films 15

2.1 Simplified Schematic of the Basic Components of AFM 24

2.2 Schematic of the Scanner Tube Used in AFM Operation 25

2.3 Resolution Difference Between "Blunt" and "Sharp" AFM Tips 27

2.4 Schematic Showing the Main Components of the Hitachi 4700 FESEM 28

2.5 Spectrum Representative of the Electron Energy Spectrum 30

2.6 Typical RBS Spectra of $MoS_2/SiO_2/Si$ and WS_2/Al_2O_3 33

2.7 Raman-Active Phonon Modes in MoS_2, with Corresponding Peaks in the Raman Shift Spectrum. Shows how the Peaks Shift as a Function of MoS_2 Layers 36

3.1 Cold-Wall CVD Reactor Used for MoS_2 Synthesis Using the Precursors MoO_3 and S 41

3.2 Custom Flange Designed to Position the Source Basket Close to the Substrate 44

3.3 Sample and Source Temperature vs. Time for a Characteristic MoS_2 Growth....... 48

3.4 MoS_2 Film Characteristic of those Grown with MoO_3 and S. Shows the Raman and PL Spectra of the Film 50

Figure | Page

3.5 Height Mode AFM Images of Single-Layer and Bi-layer MoS_2 Nanocrystals Grown with MoO_3 and S 53

3.6 SEM Images of a Low Pressure MoS_2 Growth with MoO_3 and S 55

3.7 Plot of Mo Coverage vs. MoO_3 Source Basket Temperature with Corresponding Images 58

3.8 SEM of 3D MoS_2 Nanocrystal Grown at a High MoO_3 Temperature 59

3.9 SEM Images of Identically Grown Samples Using MoO_3 and S 60

3.10 dN/dE AES Spectra of Bulk and Synthesized MoS_2 64

3.11 SEM Images Across the Length of a Sample to Show Film Uniformity. Shows Average Feature Size, Feature Density and Fractional Coverage of MoS_2 Nanocrystals vs. Position Along the Sample 65

3.12 Plot of the Variation of Temperature Along the Length of the Substrate 67

4.1 Schematic of the Bubbler System Used to Deliver Precursor Vapor to the Substrate 73

4.2 Schematic of the Growth Chamber Used for the MoO_3 and DES Sourced MoS_2 Growths 75

4.3 Plot of Vapor Pressure as a Function of Temperature for MHC and DES 77

4.4 Schematic of the Growth Chamber Used for the MHC and DES Sourced MoS_2 Growths 79

4.5 Photograph of the Custom Instrumentation Boxes Designed and Created for the Automation of the Growth Process 84

4.6 Height Mode AFM Images Showing the Effect of Annealing Al_2O_3 at 1000 °C ... 86

Figure Page

4.7 SEM and Height Mode AFM Images of the Semi-Triangular Patterning Occasionally Observed After Annealing Al_2O_3 Samples 87

4.8 SEM Images of MoS_2 Grown on Al_2O_3 Substrates Exhibiting the Semi-Triangular Patterning in Fig. 4.7 89

4.9 Schematic of the Method of Sn Bonding an Al_2O_3 Substrate to a Si Heater Strip to Allow for Heating the Al_2O_3 90

4.10 Plot of the Temperature Difference Between the Al_2O_3 Surface and the Si Heater Strip as a Function of the Temperature of the Si Strip, Using the Method Shown in Fig. 4.9 92

4.11 SEM and Height Mode AFM Images of MoS_2 Films Characteristic of Those Grown Using MHC and DES. Shows the Effect of Substrate Temperature on Growth 96

5.1 Plot of Vapor Pressure as a Function of Temperature for WHC, MHC and DES 102

5.2 Height Mode AFM of WS_2 Films Typical of Those Grown using WHC and DES. Plots Show the Effect of Increased Main Ar Flow on Growth 107

5.3 Height Mode AFM Images of WS_2 Films Grown Using WHC and DES at Different Substrate Temperatures. Plots Show the Effect of Substrate Temperature on Growth.. 109

5.4 Height Mode AFM Images of WS_2 Films Grown Using WHC and DES at Different Ar Flows Through the DES Bubbler. Plots Show the Effect of Ar Flow Through the DES Bubbler on Growth.. 112

5.5 Height Mode AFM Images of WS_2 Films Grown Using WHC and DES With and

Figure Page

Without NaCl in the Gas Line 116

5.6 Height Mode AFM Images of Identically Grown WS_2 Films Using WHC and DES to Show Repeatability of the Method 117

6.1 Schematic and Photograph of the H_2S Control System Used to Introduce H_2S into the Chamber 122

6.2 Schematic and Photograph of the Custom Heater Designed and Fabricated to Employ a W Heater Strip to Heat the Al_2O_3 Growth Substrates 126

6.3 Plot of the Temperature Difference Between the Al_2O_3 Surface and the W Heater Strip as a Function of the Temperature of the W Strip, Using the Heater Shown in Fig. 6.2 128

6.4 Height Mode AFM Images of WS_2 Films Grown Using WHC and H_2S at Different Substrate Temperatures. Plot Shows the Effect of Substrate Temperature on Growth 135

6.5 Height Mode AFM Images of WS_2 Films Grown Using WHC and H_2S at Different H_2S Flows. Plots Show the Effect of H_2S Flow on Growth 137

6.6 Height Mode AFM Images of WS_2 Films Grown Using WHC and H_2S with Different H_2S Annealing Times. Plot Shows the Effect of H_2S Anneal Time on the Island Size Distribution 141

6.7 SEM Images Across the Length of a Sample to Show Film Uniformity. Shows Average Feature Size, Feature Density and Fractional Coverage of WS_2 Nanocrystals vs. Position Along the Sample 144

A.1 Photograph and Cross-Sectional Schematic of the Thermoelectric-Cooled Liquid

Figure Page

Bath Chiller Designed, Built and Tested 173

A.2 Plot of Bath Temperature vs. Power Dissipated in the Thermoelectric Elements for the Four Different Thermoelectric Element Configurations Investigated 180

A.3 Plots of Bath Temperature vs. Total Power at Different Recirculating Chiller Temperatures and Bath Temperature vs. Flow Through the Liquid Heat Exchanger 182

CHAPTER 1

INTRODUCTION

Until very recently, the desire to maintain the scaling predicted by Moore's Law has driven research and development in the semiconductor industry. The ambition to miniaturize devices to increasingly smaller scales has led to tremendous advances in nanotechnology and engineering. The scientific world has, for now at least, begun to see the limits on such miniaturization. Heat accumulated in the confined spaces occupied by modern devices and quantum effects, such as tunneling, are among these. The realization of the limits on device miniaturization has begun to drive the semiconductor industry in new directions [1]. Of course, research labs continue to shrink the scale of semiconductor devices, but for many, the focus of research has shifted to materials whose role-specific properties are, in whole, superior to those of their predecessors. Under this exploration, a promising group of materials was discovered.

In 2004, it was shown by Andre Geim and Konstantin Novoselov that a single layer of graphite could be mechanically exfoliated from bulk material using nothing more than scotch tape. With these single-atom thick graphene films they were able to demonstrate that the single-layer material had different electronic properties than the bulk [2]. This groundbreaking discovery earned them a Nobel Prize in Physics in 2010 and a great deal of research has since been conducted to better understand how to grow and utilize graphene. From the idea that a single, '2-dimensional' (2D), layer of a material has properties unique from its bulk counterpart has spawned an entire field of materials research: 2D materials. This field encompasses graphene, topological insulators, transition metal dichalcogenides (TMDs), MXenes, organic 2D materials and many more.

Among the more intensely studied of these 2D materials are the TMDs. Like graphene, these materials are easily exfoliated from bulk material, and have interesting properties when isolated as a single layer. Because TMDs are formed of transition metals and chalcogens, there exists a sizeable matrix of TMDs available, each with its own unique electronic properties. This makes them very exciting from the perspective of device engineering. To realize the device engineering potential of these materials, however, it is necessary to move beyond scotch tape exfoliation and begin the careful study of how to synthesize them. Thus far, the majority of the efforts to produce synthetic single-layer TMD films have neither been convincingly repeatable nor controllable. For this reason, much stands to be learned about how these materials grow two-dimensionally, and their potential in electronic devices has yet to be realized.

In this dissertation, we describe our efforts to develop a rational synthesis method for growing single-layer TMDs. We begin by introducing 2D materials, then move on to introduce the class of 2D materials we investigated, TMDs. This work focuses on molybdenum disulfide (MoS_2) and tungsten disulfide (WS_2), whose properties are then outlined. The chapter continues by describing the methods currently used to obtain and synthesize single-layer TMDs, their successes and their limitations. Finally, we conclude the chapter with a description of the layout of this dissertation.

1.1 Introduction to 2D Materials

Many, often contradictory, definitions of '2D materials' have been offered. In this work, we refer to a 2D material as a material whose vertical dimension is as thin as it can get, while maintaining its identity as that material. Graphene, defined as a single layer of C atoms arranged in a hexagonal 2D net, was the first to show the potential of 2D

materials. It is a semi-metal and its covalent in-plane bonds are much stronger than its out-of-plane van der Waals interactions. The relatively weak out-of-plane interaction is what allows graphene to be so easily exfoliated from a bulk material with scotch tape, a process more casually referred to as 'the scotch tape method'. Though the out-of-plane interaction between layers is relatively weak, it still has an effect on the band structure of graphite. As layers are removed from bulk graphite, quantum confinement effects shift the band structure from a metal to a semi-metal [2]. These layer-dependent properties are one hallmark of 2D materials.

Where graphene is exciting, there exists a vast array of 2D materials with unique electrical properties in the single layer. Hexagonal boron nitride, for instance, is an insulating 2D material with a bandgap of 5.96 eV [3]. MoS_2 and WS_2 are direct bandgap semiconductors with bandgaps in the visible range [4-7]. Phosphorene is semiconductor with a bandgap of ~ 0.3 eV [8]. These are only a few of the many known 2D materials, and only considers the materials in their pure, un-doped, un-alloyed and un-strained forms. Doping, alloying and applying strain have been shown to alter the band structure of nearly all 2D materials, further widening the electronic properties available for device engineering. Having few-atom-thick materials with a myriad of available electrical properties is a potential game changer for device fabrication. Imagining vertical nanoarrays of 2D electronics and optically transparent window coatings that serve as photovoltaic cells, is no longer a topic reserved for science fiction. They are now realizable ideas and all that remains to be discovered is a straightforward method of reliable and repeatable synthesis. For this reason, discovering how to synthesize the vast

range of 2D materials on a production scale and with an industry level of repeatability has become paramount to this generation of materials research.

1.2 Introduction to TMDs

The range of available electronic properties in 2D materials was significantly broadened by the discovery that isolation of single-layer TMDs changed their electronic properties. Like many 2D materials, TMDs are not new materials, but rather the novelty of their properties in the single layer was discovered. For instance, bulk MoS_2 has been used in high-temperature lubricants for decades. In fact, the single-layer crystal structure of MoS_2 was investigated on Au(111) [9] and single-layer MoS_2 films were isolated using the scotch tape method [10] before the Nobel Prize winning work on graphene was published. It was not until 2010, however, that the full potential of single-layer MoS_2 was experimentally discovered, when it was shown in *Physical Review Letters* that mechanically exfoliated monolayer films of MoS_2 behave as direct bandgap semiconductors [6]. If MoS_2 showed exciting properties in the single layer, why not the other TMDs? Interest in single-layer TMDs boomed.

TMDs are comprised of a single, atomically flat transition metal layer (M), which is sandwiched between two atomically flat chalcogen layers (X), in the configuration X-M-X, as shown for MoS_2 in Fig. 1.1(a). In the single-layer, only two stable crystal structures exist: 1H and 1T, where H uses Ramsdell notation to indicate a hexagonal unit cell and T a trigonal unit cell. Each exhibits its own electronic properties. In the case of MoS_2, 1H is semiconducting and 1T is metallic [11]. Because the 1H film is significantly more stable, it is by far the most commonly observed of the two. Fig. 1.1(b) shows the

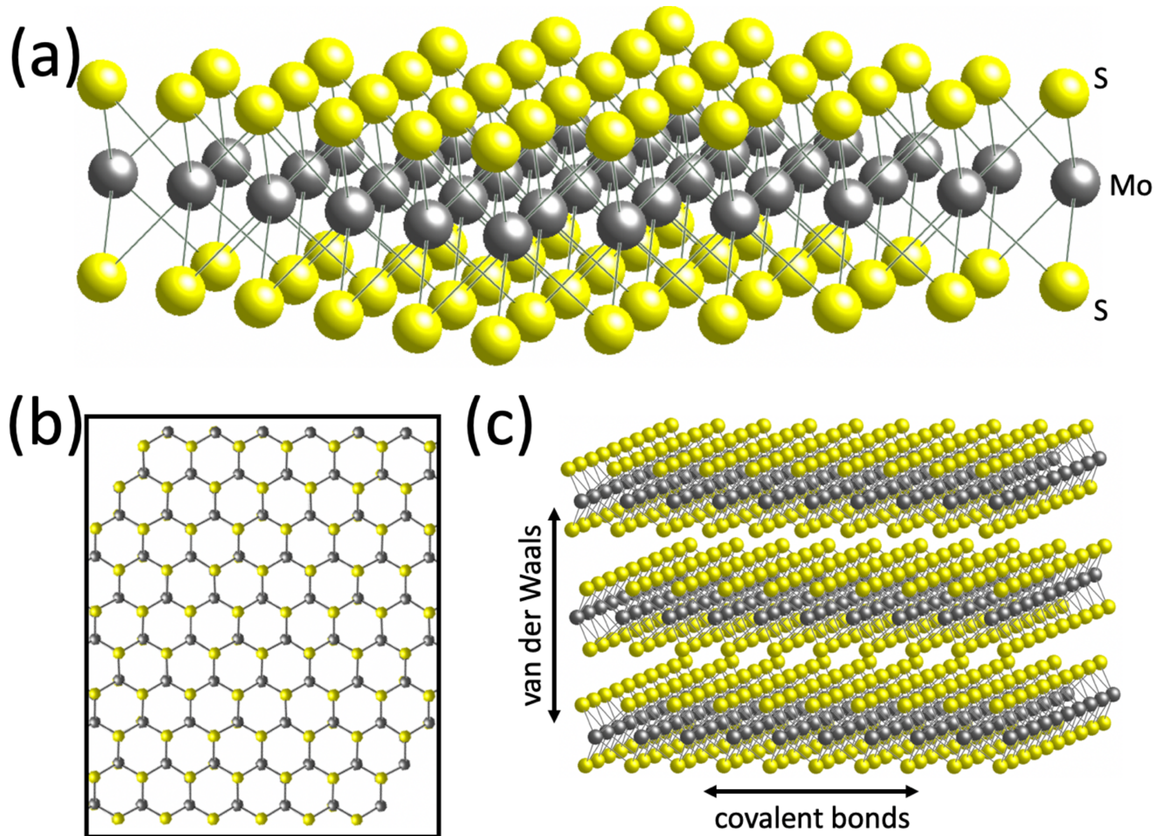

Figure 1.1: (a) Ball-and-stick representation of the 1H crystal structure of the transition metal dichalcogenide (TMD) MoS_2. A single layer of transition metal atoms, Mo, is sandwiched between two layers of chalcogen atoms, S. (b) Shows the hexagonal symmetry of the 1H structure. S and Mo atoms align in the vertical direction. (c) Shows the 2H stacking structure of multi-layer MoS_2. 3R stacking (not shown) is also possible. Regardless of the stacking structure, weak van der Waals interactions out-of-plane, compared to strong, covalent in-plane bonds, allow easy exfoliation of single-layer films.

hexagonal symmetry of the 1H structure. Multi-layer TMD films exist in stacks of the 1H structure, where the possible stacking arrangements between layers, yield different polytypes of the multi-layer TMD. Two polytypes exist: the 2H polytype, 2 layers included in a hexagonal unit cell, and the 3R, 3 layers in a rhombohedral unit cell. Fig. 1.1(c) shows the stacking of MoS_2 films in the 2H polytype. In single-layer films, of course, the stacking sequence of multiple layers does not directly concern us.

As mentioned above, a sizeable matrix of TMDs is possible under the X-M-X formulation. Since the discovery that single-layer MoS_2 has electronic properties distinct from the bulk material, the single-layer properties of the available TMDs have been predicted theoretically and, in many cases, verified experimentally. A list of some of these materials and their electronic properties is given in Table 1.1 [11]. The reader will notice the immense variety of electronic properties, spanning the range of metals, semimetals, direct bandgap semiconductors and superconductors.

All known TMDs share the X-M-X configuration, are available in the same single-layer crystalline structure (1H) and some have very similar lattice constants. Beyond the obvious device engineering potential evident by the numerous electronic properties available, shown in Table 1.1, combinations of synthesized materials with similar lattice constants should produce low-strain alloys (i.e. $Mo_{1-x}W_xS_2$ and $MoS_{2-x}Se_x$). Citing Vegard's law, the lattice constant, a, of an alloy of two materials, $A_{(1-x)}B_x$, with lattice constants a_A and a_B, is given as a function of the concentration, x, by equation (1).

$$a_{A_{(1-x)}B_x} = (1-x)a_A + xa_B \quad (1)$$

If a_A and a_B are similar, the resulting lattice constant should be similar to that of the two materials in their un-alloyed form. The bandgap, E_g, of the alloy behaves in much the

same way. Typically, $E_{g,AB}$ for an alloy of two materials can be represented by the relationship given in (1), with E_g in place of a, and with an additional term

$$E_{g,AB} = (1-x)E_{g,A} + xE_{g,B} + bx(1-x) \quad (2)$$

where b is known as the bowing parameter. This value has been determined theoretically and experimentally for a number of possible TMD alloys. TMD alloys of materials with very similar lattice constants, such as $MoS_{2(1-x)}Se_{2x}$, have a near-zero bowing parameter ($b = 0.05$ for the alloy $MoS_{2(1-x)}Se_{2x}$) [12]. Furthermore, growing low-strain, in-plane junctions between two such similar materials, termed "lateral heterostructures", should be easily achievable. Some such alloys and heterostructures have already been realized and are mentioned in the 'Current synthesis methods' section below.

M	X	Properties
Ti, Hf, Zr	S, Se, Te	Semiconducting (E_g = 0.2~2eV). Diamagnetic.
V, Nb, Ta	S, Se, Te	Metals (ρ~10^{-4} Ωcm) or semimetals. Superconducting. Paramagnetic, antiferromagnetic or diamagnetic.
Mo, W	S, Se, Te	Sulfides and selenides are semiconducting (E_g~1eV). Tellurides are semimetals (ρ~10^{-3} Ωcm). Diamagnetic.
Tc, Re	S, Se, Te	Small-gap semiconductors. Diamagnetic.
Pd, Pt	S, Se, Te	Sulfides and selenides are semiconducting (E_g~0.4eV) and diamagnetic. Tellurides are metallic and paramagnetic. $PdTe_2$ is superconducting.

Table 1.1: Lists the different X-M-X combinations of TMDs and their respective electronic and magnetic properties in the single-layer. This thesis focuses on the TMDs MoS_2 and WS_2. This data is reproduced from Chowalla et al. *Nature Chem.*, 2013 [11].

1.3 Properties of MoS_2 and WS_2

Though the possible TMD combinations, X-M-X, available to the researcher are many, this work focuses on the synthesis of MoS_2 and WS_2. Atomic force microscopy (AFM) measurements of both MoS_2 and WS_2 single layers report thicknesses to be between 0.6 nm and 0.9 nm thick, where theoretical studies predict them to be 0.7 nm thick [13-14]. Variation between the measured values is likely due to surface roughness and the interaction between the surface and the film. As stated above, single-layer TMDs have distinct band structures from their bulk counterparts. Both MoS_2 and WS_2 are indirect bandgap semiconductors in bulk, and, as layers are removed, the band structure shifts under quantum confinement. Once a single layer is isolated, the band structure has fully shifted from an indirect to a direct bandgap semiconductor. Fig. 1.2 shows this shift in the band structure of MoS_2 as a function of layers. MoS_2 and WS_2 single layers have bandgap energies in the visible range, 1.8 eV and 1.9 eV, respectively [4-7]. Because direct bandgap materials require only photonic excitation to excite electrons from the valence band maximum to the conduction band minimum, and because photons are emitted when excitons relax, they are ideal for optoelectronic applications. Furthermore, purely from the perspective of synthesis research, direct bandgap materials are nice because photoluminescence spectroscopy (PL) provides a ready check of the quality of the material.

Beyond the potential for use in what might be called 'traditional' electronic devices, TMDs with M = Mo and W, such as MoS_2 and WS_2, have shown tremendous promise in the budding field of 'valleytronics,' a subfield of quantum computation which relies on selectively exciting electrons or holes to specific minima in the conduction

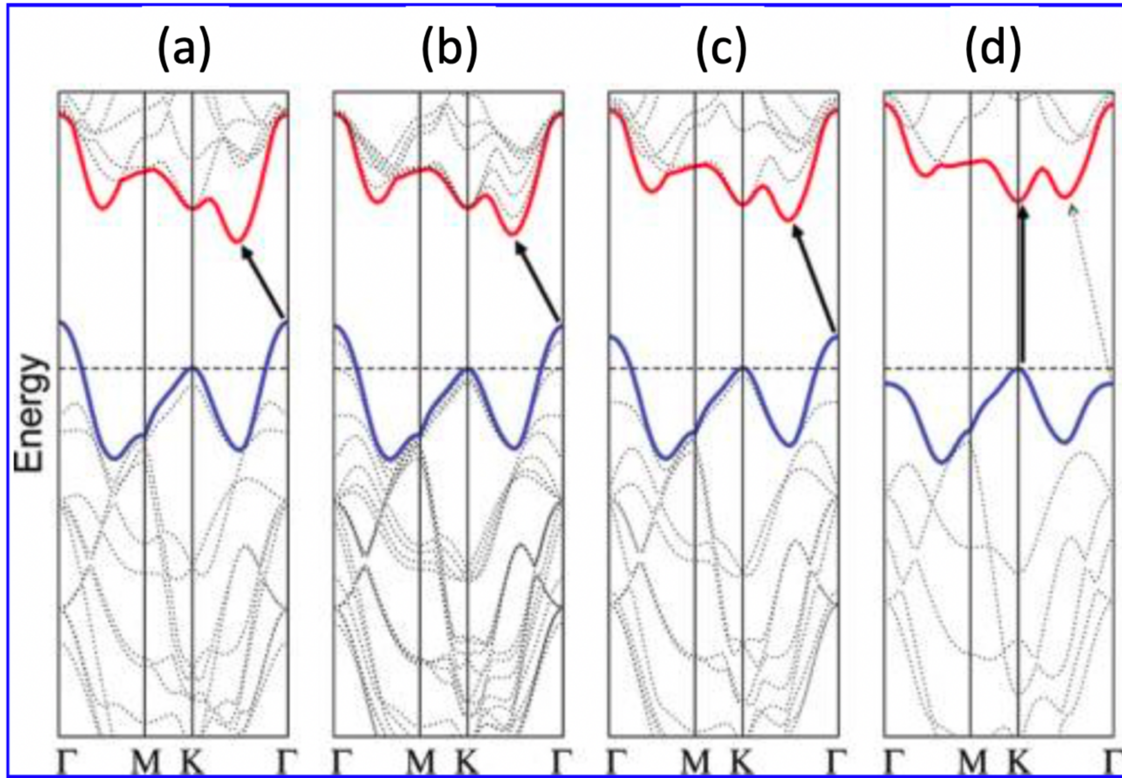

Fig. 1.2: Shows the change in band structure of MoS_2 as it is thinned from (a) bulk to (b) four layers, (c) two layers and (d) single layer. The alignment of the valence band maximum and the conduction band minimum in (d) shows the direct bandgap nature of single-layer MoS_2. This data is reproduced from Splendiani et al. *Nano Lett.* 10, 1271, 2010 [5].

band, referred to as 'valleys.' In MoS_2 and WS_2 these valleys exist at the corners of the Brillouin zone, the +K and -K points (shown in Fig. 1.3), where +K and -K refer to spin-up and spin-down valence electrons most easily excited to the conduction band [15]. Because of the anti-symmetry of the spin-orbit coupling shown in Fig. 1.3, electrons at either +K or -K can be excited to their respective conduction valleys. Which valley is populated is determined by the orientation (right hand or left hand) of a circularly polarized excitation. When the excitons relax, the emission exhibits the same circular polarization as the excitation beam [16]. This is an exciting property because it shows the ability of the single-layer MoX_2 and WX_2 TMDs to preserve information and their potential for use in valleytronic switching devices.

1.4 Current Synthesis Methods

1.4.1 Mechanical Exfoliation

Like graphene, mechanical exfoliation was the first experimentally realized method for production of single-layer films for nearly all 2D materials. TMDs are no exception. While not a scalable synthesis method, the process of mechanically exfoliating layers has allowed many of the electronic properties listed in Table 1.1 to be experimentally observed and is still used today as a facile method of obtaining samples for study. Though straightforward and inexpensive to perform, this method is severely limited by the randomness of the crystals obtained, both in terms of size, distribution and thickness. Fig. 1.4 shows this randomness, presenting (a) optical microscope and (b) scanning electron microscope images of mechanically exfoliated (a) MoS_2 and (b) WS_2 crystals, justly representative of the majority of those found in the literature.

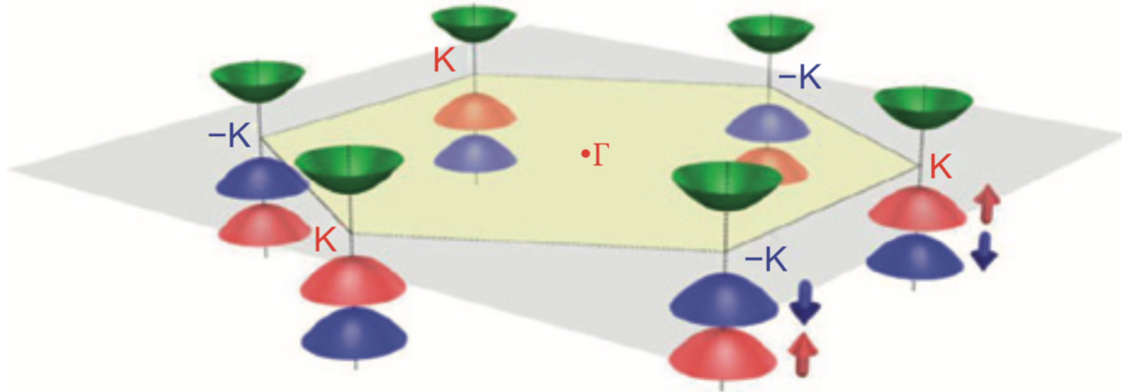

Fig. 1.3: Shows the band structure of MoS_2 with the 6 corners of the Brillouin zone. The spin orbit splitting in the maxima of the valence band is shown as the blue and red peaks, for spin-down and spin-up states, respectively. The green valley directly above show the conduction band minima at each of the +K and -K points. This figure is reproduced from D. Xiao et al. *Phys. Rev. Lett.* 108, 196802, 2012 [15].

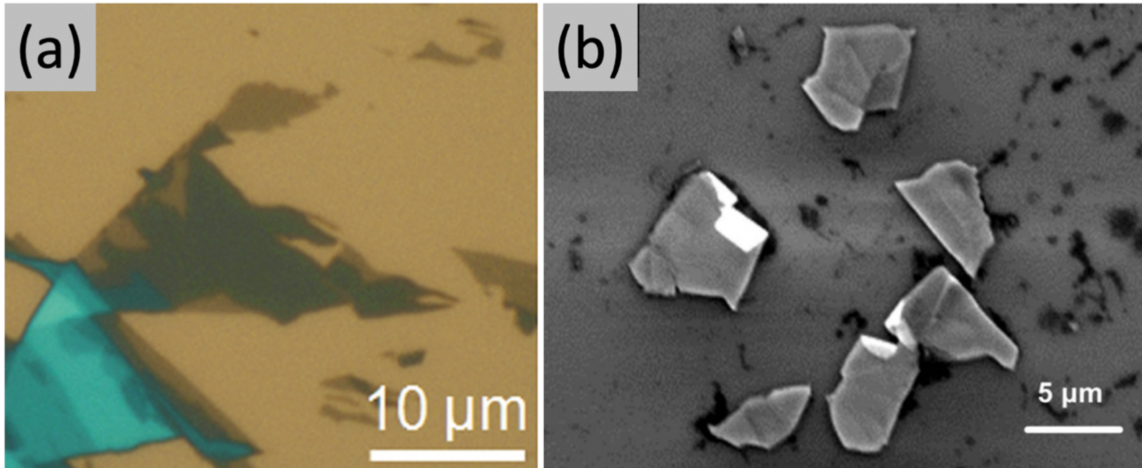

Fig. 1.4: Shows films typical of those exfoliated from bulk material for (a) MoS_2 [17] and (b) WS_2 [18]. Note the unpredictable distribution of features and film thickness inherent to this method of obtaining TMD films. In (a), for example, the contrast in the cyan color is proportional to the thickness, with lighter hues corresponding to many-layer thick regions and the regions slightly darker than the gold-colored substrate are single-layer. Images have been reproduced from references (a) 17 and (b) 18.

Other methods of exfoliation have been explored as well, including chemical [19] and solvent assisted [20] exfoliation. Each is an improvement upon mechanical exfoliation in uniformity of the layers produced. Groups have worked very hard at perfecting the craft of exfoliation and have even been able to successfully produce vertical heterostructures (out-of-plane junctions between two distinct films) of many different 2D materials [21]. This heterostructure formation of exfoliated films is most commonly accomplished by a mechanical transfer process, where one exfoliated film is lifted via adhesive tape or poly(methyl methacrylate) (PMMA) and carefully stacked on top of another. After stacking the film lifting material is dissolved in a solvent, such as acetone, or by etch removal [21]. In spite of these efforts, exfoliation, in all its forms, has the major limitation of being a "top-down" process, meaning small features are taken from a larger whole and a more flexible and scalable process is required to better realize these materials' potential.

1.4.2 Hot-Wall CVD

To satisfy the need for a more flexible and scalable process, a number of synthesis methods have emerged. Because of the novelty of these materials, the general aim of research, with very few exceptions, has been to (a) demonstrate synthesis while (b) growing the largest possible area single-layer crystal, either by the synthesis of a single large-area crystal [14,22-23], or by growing large area films consisting of smaller coalesced grains [24-25]. Foremost among the emergent synthesis methods is hot-wall tube furnace chemical vapor deposition (CVD).

For the synthesis of all TMDs synthesized to date, substrates (SiO_2/Si, SiC, or Al_2O_3) are placed in a hot-wall tube furnace downstream from a flowing carrier gas

source. In the case of MoS_2, a pure S and a powder molybdenum-oxide source (MoO_x, most commonly MoO_3, exceptions are given below) are placed upstream of the sample [26-32]. The carrier gas is flowed through the chamber for an extended period of time to purge the furnace of ambient impurities. The furnace is then heated to a programed set-point above the sublimation point of S, where there is an adequate vapor pressure from the MoO_3. The carrier gas acts to dilute the gas-borne sources, carry the sources to the substrate and apply an ambient pressure at the substrate. Given the low melting point and high vapor pressure of S, it has been justly speculated that Mo deposits on the substrate, and subsequently gives arriving S a low energy site to bond to [33]. Fig 1.5(a) is given as a schematic for a typical tube-furnace CVD method described.

Repeatability and uniformity are major limitations of hot-wall CVD growth. Though rarely discussed in the literature, contradictions in growth trends and the lack of results investigating the effect of various growth parameters on crystal size and density imply that run-to-run consistency is a problem. Conversation with a number of these researchers has confirmed this suspicion. Uniformity is another limitation. Typically, in order to obtain large-area single-layer features, films are grown that exhibit a dramatic gradient from multi-layer full-coverage regions to sub-monolayer regions where single-layer crystals are found, imaged and analyzed. Fig. 1.5(b) and (d) shows films typical to those published in the literature [33-34]. Such images are rarely presented, however, and only one or two "ideal" crystals are shown, giving no information about the uniformity of the film. The paper from which Fig. 1.5(c) was taken is a stark exception to this and shows the features available to the microscopist at different points along the 2 cm x 2 cm sample[34]. Where much progress has been made in the 2D materials field using hot-wall

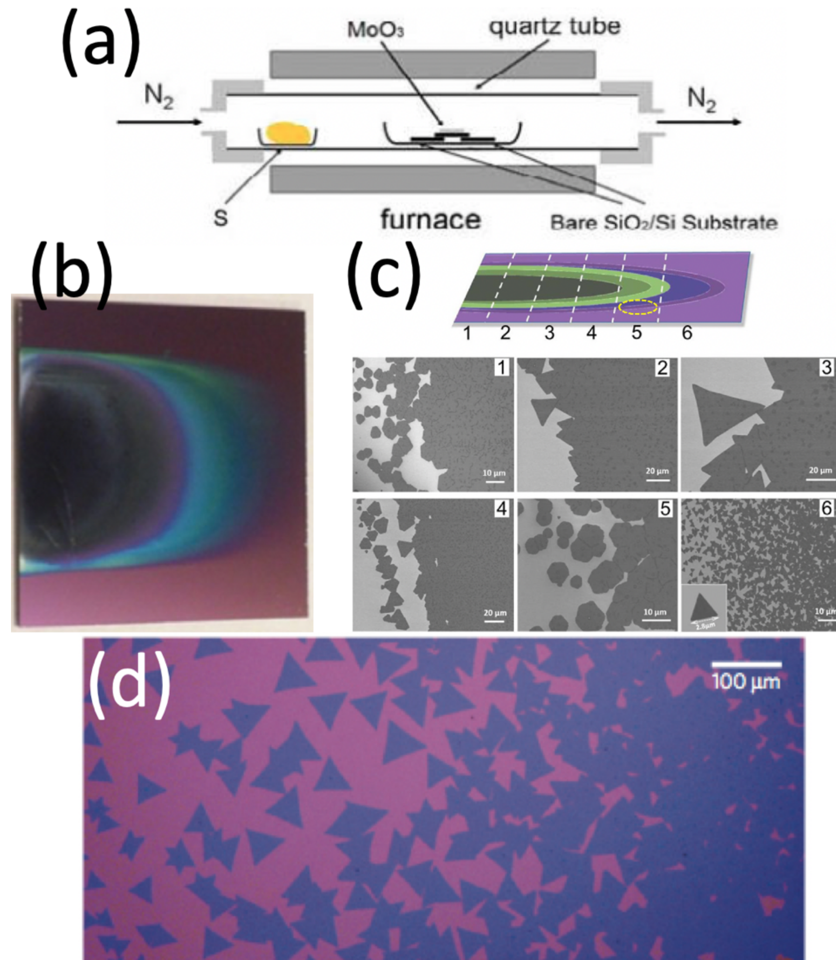

FIG 1.5: (a) Typical schematic of the hot-wall CVD system employed to evaporate MoO_3 and S, which condense at the substrate forming MoS_2 [26]. (b) Shows a typical film grown by this method on a 2 cm x 2 cm SiO_2/Si substrate. The pink background is the substrate and the black area is many-layer growth of MoS_2. As the film spreads to the right side of the image, the layers thin until single-layer films, almost indistinguishable from the substrate, are present. (c) a series of scanning electron microscope images taken from various points along the sample [32]. (d) Optical microscope image of another film grown by this method, where the purple triangles are MoS_2 on a pink SiO_2/Si substrate [33]. (a) is reproduced from reference 31, (b) and (c) from reference 32 and (d) from reference 33.

CVD, non-uniform films such as these make the process of device engineering cumbersome, if not impossible on a large scale, and improvements remain necessary.

In addition to the dramatic layer gradient and lack of repeatability of most hot-wall-grown films, the process provides little control over the temperatures the source materials actually reach. Indeed, this could be the culprit for the lack of repeatability and careful growth studies. In most cases, the sources are placed a distance from the hot center of the furnace, at which a temperature has been previously measured. Some groups even slide the sources closer to, or farther away from the hot center of the furnace to achieve some control over the temperature. To circumvent this problem, some groups have, with varied success, switched to gas phase and high vapor pressure precursors delivered from outside the furnace. Focusing on MoS_2, a variety of source materials have been used: molybdenum chloride ($MoCl_5$) [35-38] and molybdenum hexacarbonyl ($Mo(CO)_6$) [39] have been used as Mo precursors, and hydrogen sulfide (H_2S) [40], diethyl sulfide ($C_4H_{10}S$) [39-40] and dimethyl sulfide (C_2H_6S) [41] have been used for S. Each of these variations on the hot-wall CVD growth method have met with varied success, but still fail to produce a cohesive data set demonstrating the effects of the growth parameters on synthesis. Note that W and Se counterparts to these precursors have been used to synthesize the other TMDs, with similar results. The synthesis of MoS_2 is highlighted here to avoid confusion, redundancies and because it is the most commonly grown TMD.

Other CVD tube-furnace methods for synthesizing single-layer MoS_2 have acted on the hypothesis that chemical reactions not localized at the growth surface hinder repeatability by allowing byproducts from reactions throughout the hot furnace to

condense at the substrate. These methods have employed a sulfurization approach, where Mo is pre-deposited on the substrate as either Mo [14,42], MoO_2 [43-44] or MoO_3 [45] and then exposed to a hot sulfurous ambient. Still careful studies of growth trends from groups who employ tube furnace-based hot-wall CVD remain sparse and often contradictory.

1.4.3 Other Methods: Dip Coating Thermolysis, MBE, ALD and Cold-Wall CVD

Because the literature suggests that it is possible to synthesize single-layer TMDs using the hot-wall CVD method described above, but difficult to obtain the consistency needed for more complicated processes, a number of groups have tried other methods of single-layer TMD synthesis. Dip coating thermolysis has been use to produce large scale MoS_2 films. SiO_2/Si substrates are dipped in a solution of ammonium tetrathiomolybdate, $(NH_4)_2MoS_4$, after which, an annealing procedure evaporates the residuals and allows for the reordering of Mo and S atoms on the substrate [46]. Though this procedure can produce films with large lateral dimensions and the process rather straightforward, the method seems to be limited by thickness uniformity and still needs work, and no work to further this method has been published.

Molecular beam epitaxy (MBE) and TMDs have a long history. When it was shown that van der Waals materials act as good substrates because low junction interactions don't significantly strain the lattice of the grown material, MBE of MoS_2 and other TMDs became commonplace [47]. When the current drive to synthesize single-layer TMD films started, MBE synthesis methods for TMDs were already in place. The trick was and remains in getting the film to grow as a single layer. Groups have succeeded at this for a number of TMDs, with varying degrees of success, and in some

cases have been able to use their films in the fabrication of devices [48-50]. However, due to the volatility of solid S, discussed in chapter 3, it is unlikely that this method will prove a viable method for growing single-layer MoS_2 and WS_2 in the future.

Another method being currently explored is atomic layer deposition (ALD). ALD has produced single- and few-layer films of a variety of TMDs, usually using plasma-enhanced ALD to handle the low sublimation point of the chalcogens. Films produced by this method exhibit the expected optical properties, though the authors admit that the crystallinity of the synthesized films needs improvement before this method can be implemented in large-scale production [51-54].

A small number of groups have taken the hot-wall CVD scheme and translated it to an industry relevant cold-wall set up, which isolates the chemical reactions to the growth surface. Of the methods mentioned, this, by far, has met with the most success and proven to the be most promising. Notably, this method has been used by the "2D Crystals Consortium" at Pennsylvania State, where WSe_2 films have recently been grown with great success, achieving control over the growth parameters, exploring the parameter space and synthesizing large monolayer WSe_2 features, ~ 1 μm in size [55]. WS_2 films grown by the same 2D Crystals Consortium have begun to show promise, recently exploring the effect of different S precursors on film synthesis and achieving a feature size of ~ 200 nm [56]. In our own work, published in *Crystal Growth and Design* and detailed in chapter 3, we demonstrate the ability of this method to grow single-layer MoS_2 with a high level of uniformity and repeatability in coverage. The many steps we took to improve upon that early method is the topic of much of this dissertation.

1.5 Importance of Understanding and Controlling Growth

Each of the above-mentioned methods has contributed to furthering the field of TMD synthesis. Citing the accomplishments of the hot-wall tube-furnace CVD method alone, isolated single-grain, single-layer, triangular crystals, with a base length of 100μm, have been grown [57-58]. Many of these synthesized films have been used to fabricate electronic devices.[59-60] The method has also allowed for the discovery that the optical properties of feature edges are different than at the feature center [25,61]. Hot-wall CVD grown TMD films have also been used to demonstrate TMD bandgap tunability, using doping [62], strain [63], alloying TMDs (for example: $Mo_xW_{1-x}S_2$) [64-66] and by the fabrication in-plane [67-70] and out-of-plane [67,70-71] heterostructures.

Despite the tremendous advances in the field using the methods described above, most studies continue to publish 'best-growth' results without offering any in-depth understanding of how these films grow. In order to fully advance the field into the large-scale fabrication of complex TMD devices, it is imperative to develop a growth method that produces repeatable results. From there, the effect of the various growth parameters on morphological characteristics, such as feature size, density and number of layers, must be carefully catalogued. Such work has previously been done by the Drucker group for several materials [72-74] and nanostructures [75-78]. With knowledge and control of this sort over the synthesis of TMDs, not only will the way be paved for large-scale fabrication of TMD electronic devices, but bandgap engineering and the synthesis of compound 2D materials can become common place.

To obtain this knowledge and overcome the challenges encountered by the many groups currently growing TMDs, we first created a cold-wall analogue of the hot-wall MoO_3 + S vaporization method outlined above. Our cold-wall system was carefully

designed to allow independent control over the many growth parameters involved. Using this method, we were able to demonstrate enhanced film uniformity across the sample, excellent run-to-run repeatability of film coverage, and were able to begin exploring the effect of various parameters on growth. Even with that level of control, we were still hampered by a lack of morphological run-to-run repeatability.

To enhance our control over the delivery of source materials, we switched to a true CVD method employing molybdenum hexacarbonyl (MHC) and diethyl sulfide (DES). To lower the vapor pressure of the transition metal source, we eventually switched from MHC to tungsten hexacarbonyl (WHC) to synthesize WS_2. This work yielded a number of interesting results, allowing us to demonstrate the effect of even more growth parameters on nucleation density and feature size. However, some undetermined limitation prevented our ability to grow satisfactorily large feature sizes and we switched from DES to H_2S as our S precursor. Using the combination of WHC and H_2S we were able to achieve our best films and were able to demonstrate the ripening of features by annealing in an Ar + H_2 + H_2S ambient. This work posed many challenges which required the fabrication of many custom pieces and a number of modifications to the growth chamber configuration. We did our best to overcome these challenges and anticipate that our work will be a good contribution to the field of TMD research.

1.6 Dissertation Layout

The main body of this document in divided into seven chapters. We begin the discussion of this project with an outline of the analysis techniques used throughout, namely: atomic force microscopy, scanning electron microscopy, Rutherford backscattering spectrometry, Raman spectroscopy, photoluminescence spectroscopy and

Auger electron spectroscopy. With the exception of the concluding chapter, subsequent chapters are broken into four main parts: (1) Experimental methods, where we outline the reactor configuration used and the methods used for preparing and heating the growth substrate. In this section, we also detail growth preparation, procedure and the parameters investigated. (2) Characterization methods, were the specific methods used for analyzing our samples are outlined. (3) Results and discussion, where we show and discuss the results from the series of experiments in question. And finally, (4) limitations and motivation for configuration change, where the discussion is furthered into specifying the limitations we encountered and outlining our hypotheses for moving forward. Finally, we conclude this work with a concluding summary and discussion of suggestions for future research.

Following the main body of this dissertation is an appendix. This appendix outlines our work designing, creating and testing a thermoelectric-cooled liquid bath chiller, published in 2018 in *Review of Scientific Instruments*. The design and feasibility of this chiller was explored in our pursuit of stably cooling our MHC and WHC precursors for long growth times. This is motivated more completely in chapter 4.

CHAPTER 2

ANALYTICAL METHODS USED THROUGHOUT

In this chapter, the experimental techniques used to characterize the samples grown for this dissertation are outlined. These methods include those used for characterizing morphology (atomic force microscopy and scanning electron microscopy), composition (Rutherford backscattering spectrometry and Auger electron spectroscopy) and optical properties (Raman spectroscopy and photoluminescence spectroscopy) of MoS_2 and WS_2 thin-films. Application of and analysis of the data produced by these techniques specific to a given chapter are included in that chapter.

2.1 Atomic Force Microscopy

Atomic force microscopy (AFM) is a very powerful and easy-to-use tool to obtain topographical information about a film. In this study, we primarily used a Bruker Multimode 8 AFM, maintained by the Goldwater Materials Science Facility, to obtain film thickness, feature morphology and feature density. A Dimension Multimode III was also used in early the project, but no images presented herein used the Dimension. The AFM images shown in Chapter 3 were obtained at a Bruker Fast-Scan AFM demonstration by Senli Guo from Bruker Instruments.

All images were acquired using tapping mode. Tapping mode AFM was performed using a Si tip protruding from an Al coated Si cantilever. A laser is reflected from the top of the cantilever onto a split photodiode detector. A voltage applied to a piezoelectric crystal causes vertical harmonic oscillations of the cantilever at just below the resonant frequency of the cantilever with an amplitude between 20 nm and 100 nm. The sample surface is raised toward the oscillating tip, until contact with the surface

limits the amplitude of the oscillation. The sample is then lowered to a point where the oscillation amplitude reaches the setpoint amplitude. The sample height is recorded by the computer. Taking these measurements at every point, the sample is raster scanned beneath the tip. A schematic of this operation is given in Fig. 2.1. Though the Bruker multimode is capable of generating a number of information maps from this data, all AFM images presented herein are height mode images, where contrast in the image is proportional to height. Images were analyzed using the software Image SXM [79].

Scanner operation in AFM is very cleverly engineered. The scanner tube employs four pairs of electrodes to apply a voltage to a piezoelectric (PE) material, labeled in Fig. 2.2 as X, $\bar{X}$, Y and $\bar{Y}$. Applying a positive voltage bias to a PE material causes an expansion of the material. Inversely, a negative voltage contracts the material. In this way, a positive voltage across the $\bar{X}$ segment coupled with a negative voltage across X causes the scanner to move in the direction of X. A positive voltage applied to all four segments increases the Z, height, of the scanner tube, and a negative voltage applied to all four decreases Z. This design affords very precise control over the X, Y and Z positions of the scanner tube. In the Bruker Multimode 8, used for the majority of the imaging presented herein, the tip is oscillated in place and the sample is mounted to the scanner tube. The Dimension Multimode and the Bruker Fast Scan mounts the tip to the scanner tube.

We used Aspire CT300 AFM tips, with a radius of 8nm and a cone angle of 30°. Because of the way AFM images are obtained, described above, the sharper the tip and lower the cone angle, the higher the resolution of the obtainable image. Using a blunt tip,

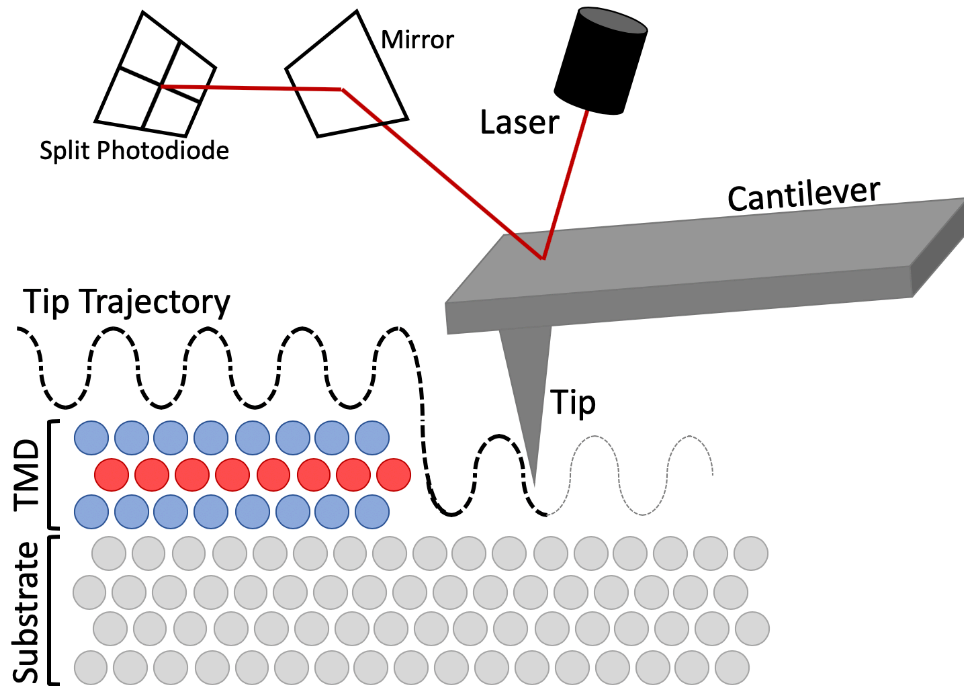

Figure 2.1: Simplified schematic of the basic AFM components and their operation of tapping mode AFM. A laser is reflected off the reflective cantilever onto a split photodiode detector. The cantilever is oscillated at just below resonance and the sample raised toward the oscillating tip. As the tip encounters the sample, the amplitude of oscillation is limited. The sample is lowered until the "setpoint" amplitude is reached. The height at this (x,y) point is recorded and the sample is raster scanned beneath the tip. At each point along the scan, the height needed to maintain the setpoint amplitude is recorded. In this way, a topographical map of the sample is obtained.

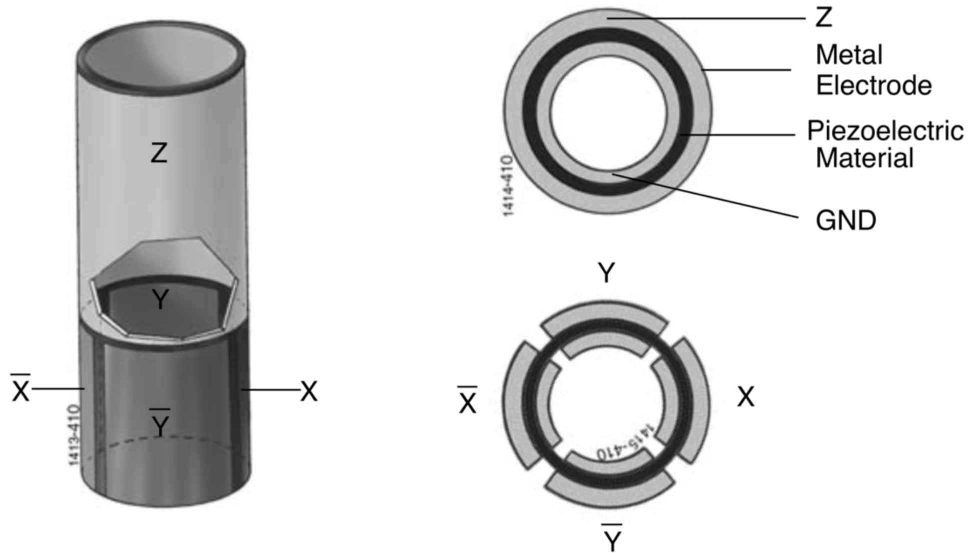

Figure 2.2: Schematic of the scanner tube used in AFM operation. The scanner tube is a piezoelectric material surrounded by a metal electrode with a metal ground at the core. This is broken into four segments. Voltage applied across the segments causes an expansion or contraction of the piezoelectric material, depending on the sign of the voltage applied. By precise manipulation of this expansion and contraction, control over the X, Y and Z directions of the sample, or cantilever, depending on the model of AFM used, is used to scan the sample and achieve a topographical image. This image is adapted from ref [80].

features are broadened and edge information is lost. Fig. 2.3 shows this effect with a schematic of two separate AFM tips, (a) a "blunt" tip and (b) a "sharp" tip. Fig. 2.3(c) shows the two scans side-by-side for comparison. This effect played a part in our analysis when we computed the percentage of our films that are single-, double-, triple-, and quadruple-layer. A detailed description of this analysis technique is given in chapter 5. In the analysis, an 'unaccounted for' percentage indicates the percentage of the film area that doesn't fall in to one of the single-, double-, etc. -layer ranges. This unaccounted for amount is most likely due to the 'bluntness' of our tip.

2.2 Scanning Electron Microscopy

Feature size, morphology and density were obtained using the field emission scanning electron microscope (FESEM), Hitachi 4700, maintained by NanoFab, at ASU. The Hitachi 4700 FESEM uses an electric field applied to a sharply etched monocrystalline W tip to extract electrons with an extremely low energy spread. These electrons are then accelerated by an accelerating voltage applied to an accelerating anode to an energy between 1 keV and 30 keV.

This beam of electrons is then focused by a series of electromagnetic lenses. The beam first passes through two condenser lenses, which act to reduce the beam diameter, and then an objective lens, which focuses the beam on the sample surface. To ensure the beam is circular the Hitachi 4700 uses a quadrupole stigmator, which applies weak supplemental magnetic fields to restore the beam to circular. Fig 2.4 shows the basic components of the Hitachi 4700.

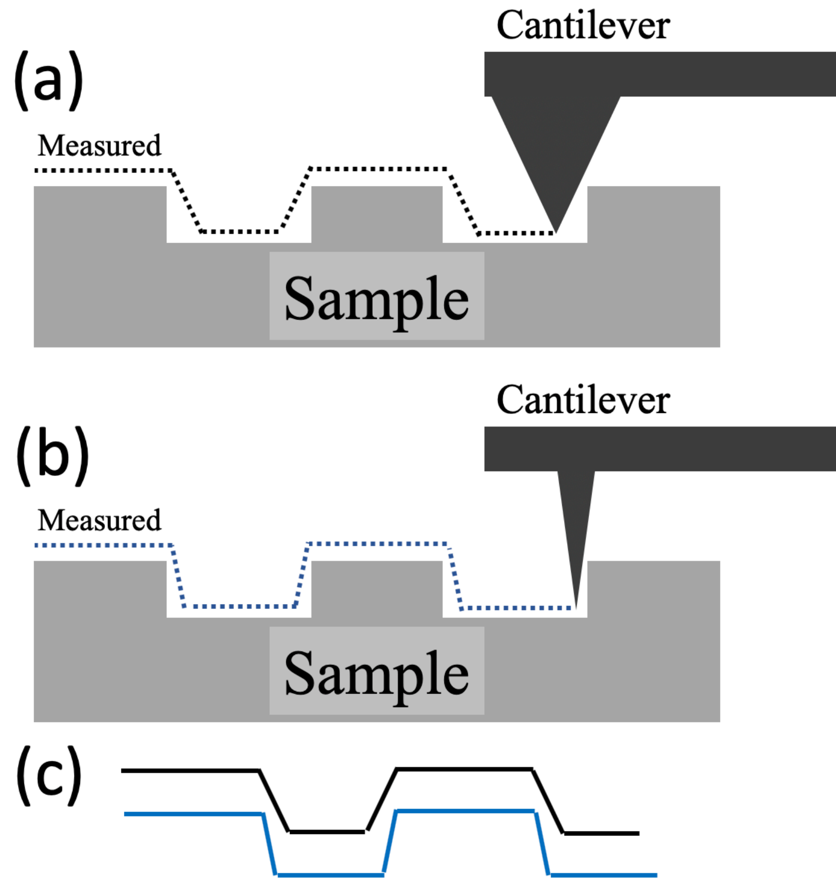

Figure 2.3: Shows the difference in image resolution between (a) "blunt" and (b) "sharp" AFM tips. Using a blunt tip produces images of features that are broadened, compared to the actual feature, and yields a feature edge height information that does not accurately reflect the edge of the feature. (c) is a comparison of the scans obtainable by the two tips in (a) and (b). The black line on top is representative of (a) and the blue line on bottom, of (b). Note that neither scan perfectly reflects the vertical edges of the sample peaks.

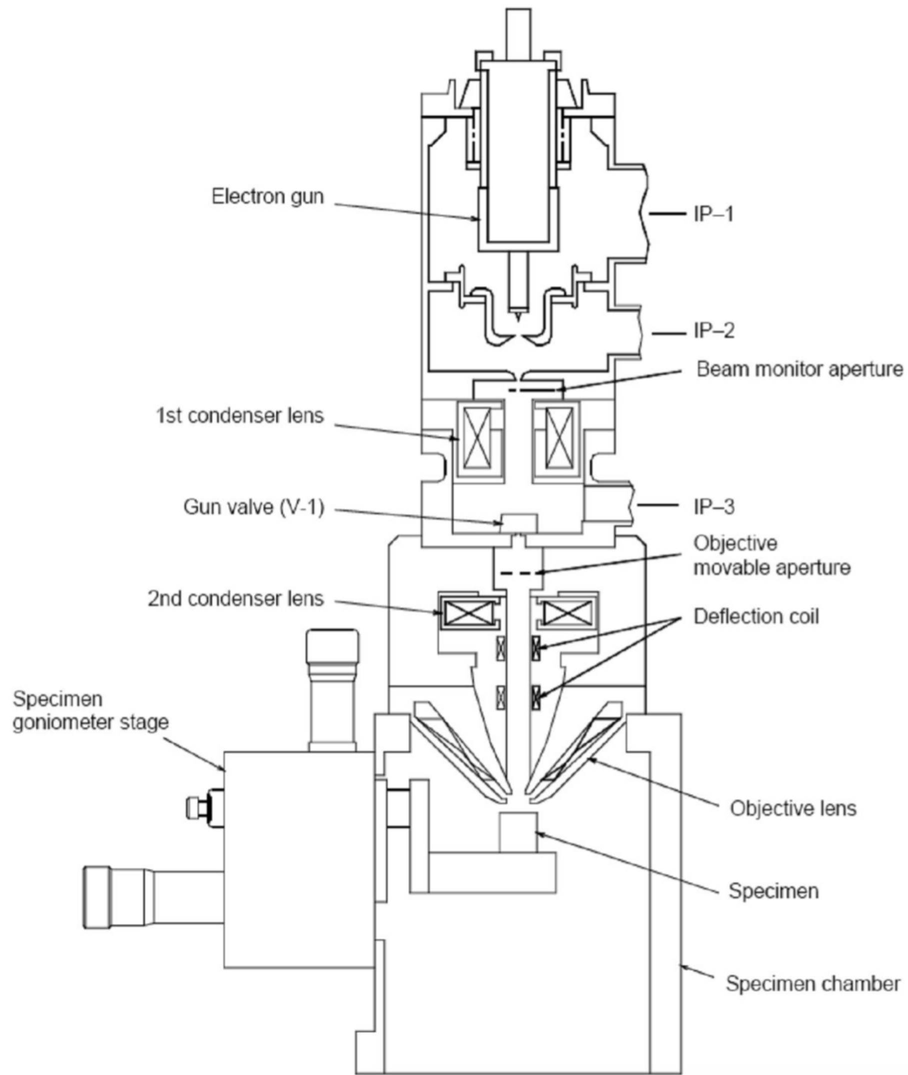

Figure 2.4: Shows the main components of the Hitachi 4700 field emission scanning electron microscope (FESEM). This is adapted from reference [81].

The focused beam is raster scanned across the surface by the deflection coils. Though some beam electrons are "elastically" scattered by the sample (in this case meaning there is little-to-no difference in the kinetic energy between incident and scattered electrons), the inelastic scattering of beam electrons is what matters to us. Beam electrons involved in inelastic scattering transmit some of their energy to the electrons and nuclei of the sample. When this happens with loosely bound outer-shell electrons, the interaction can impart enough energy to the outer-shell electron to eject it from the atom. These electrons are called secondary electrons (SEs), and have an energy < 50 eV. Emission of SEs is collected by an Everhart-Thornley detector, which maintains a positive bias relative to the sample to attract the SEs. When an energetic electron impinges the scintillating crystal of the detector, light is emitted. The emitted light is channeled to a photomultiplier and translated out of vacuum as light to a photocathode, which converts the photons back to electrons, in which form they are finally collected and compiled as an image. Fig. 2.5 shows a representative electron energy spectrum from a beam of electrons, with an energy E_0, incident on a sample. The largest peak (energies < 50 eV) is attributable to SEs. Between 50 eV and 2 keV are two minor peaks, which account for the Auger electrons, discussed below.

Digitally acquired micrographs of MoS_2 and WS_2 films were analyzed using ImageJ [82] to determine nucleation density, areal coverage and average feature size. The coverage measured using SEM could be compared to the transition metal concentration to elucidate details about the growth mechanism that were otherwise difficult to obtain, as shown in reference [83]. SEM performed on TMD/Al_2O_3 films was challenging because of the insulating nature of sapphire. Charge quickly built up at the surface, deflecting the

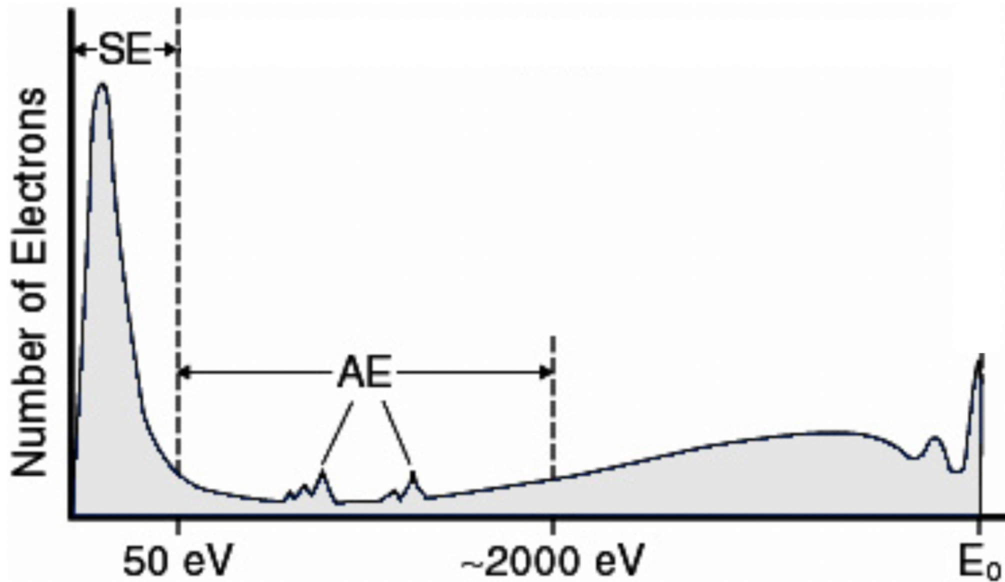

Figure 2.5: Representative electron energy spectrum for a beam of electrons, at an energy E_0, incident upon a sample. The large peak between 0 eV and 50 eV is the secondary electron peak. The two minor peaks, labeled "AE" in the figure, are the Auger electron peaks. This is adapted from ref [84].

beam and making acquisition of images suitable for analysis difficult. It was found that the best images were obtained angling the sample 20° off perpendicular to the electron beam, with an accelerating voltage of 5kv and an emission current of 10 μA. These acquisition parameters gave resolution good enough to resolve 30 nm features against the sapphire substrate.

2.3 Rutherford Backscattering Spectrometry

Film composition was determined using Rutherford backscattering spectrometry (RBS). RBS operates by accelerating a beam of α particles to an energy of 2 MeV. These ions are directed toward the sample, where the incident α particles are scattered by the atoms in the sample. As the scattering is elastic, the relationship between the incident energy E_0 and the scattered energy E_S is given by the kinematic factor, K:

$$K = \frac{E_S}{E_0} = \left[\frac{(m_2{}^2 - m_1{}^2 \sin{}^2\theta)^{1/2} + m_1 \cos\theta}{m_1 + m_2}\right] \tag{3}$$

where m_1 is the mass of the scattered particle, m_2 is the mass of the target atom and θ is the scattering angle. The mass of the scattered α particles and the scattering angle (170° for our RBS) are constant. Therefore E_S is determined by the mass of the target atoms, m_2. By binning scattered α particles according to energy, RBS gives a spectrum where peaks are related to the atomic masses in the sample by eq. (3) and the areas under the peaks correlate with the density (atoms/cm^2) of a given element.

Typical RBS spectra for $MoS_2/SiO_2/Si$ and WS_2/Al_2O_3 are given in Fig. 2.6(a-b) and 2.6(c-d), respectively. The spectra in Fig. 2.6(a) and (b), were taken from a sample where 0.3 monolayers (ML) of MoS_2 was deposited on a SiO_2/Si substrate. To determine a ML coverage value, we simply convert the measured areal density of Mo (atoms/cm^2)

using the atomic density of Mo in a single layer of MoS_2, 1.15 x 10^{15} atoms/cm^2. In Fig. 2.6(a), the O and Si energies are labeled. Backscattered α particles that penetrate deeply into a material lose energy going in and coming back out, so that "peaks" of thick materials appear in the spectra as plateaus. The small shoulder, ~ 1MeV wide and arrowed in Fig. 2.6(a), is a result of two materials with Si in the substrate. Because of the difference in atomic density of Si between SiO_2 and Si, and because α particles loose energy as they penetrate into the sample, two Si signals emerge. One signal has fewer counts at a higher energy. This signal is from the Si in the overlaying SiO_2. The other is from the underlying Si and has more counts and appears at a lower energy.

Note the proximity of the S peak to the Si signal. This proximity is a result of the similar atomic numbers, and therefore similar atomic masses of the materials, S = 16 and Si = 14. This proximity made obtaining S quantities in sub-monolayer $MoS_2/SiO_2/Si$ quite difficult. For this reason, information about quantities of S in these samples, or at least a comparison of the S quantities to the Mo quantities was obtained using Auger Electron Spectroscopy, as detailed below. Fig.2.6(b) is magnified from (a), focusing on the region from 1.22 MeV to 1.78 MeV, to show the well-defined Mo peak used to determine Mo coverage.

Fig. 2.6(c) shows 0.2 ML of WS_2 grown atop an Al_2O_3 substrate. Note the increased separation between the S peak and the signal from Al in the Al_2O_3, allowing us to use RBS to determine stoichiometry for these films. This is possible because of the increased difference in masses between S and Al, atomic numbers 16 and 13, respectively. Like (b), 2.6(d) is magnified from (c), focusing on the region from 1.1 MeV to 1.93 MeV, to better show the W and S peaks in (c). The atomic density of W in a

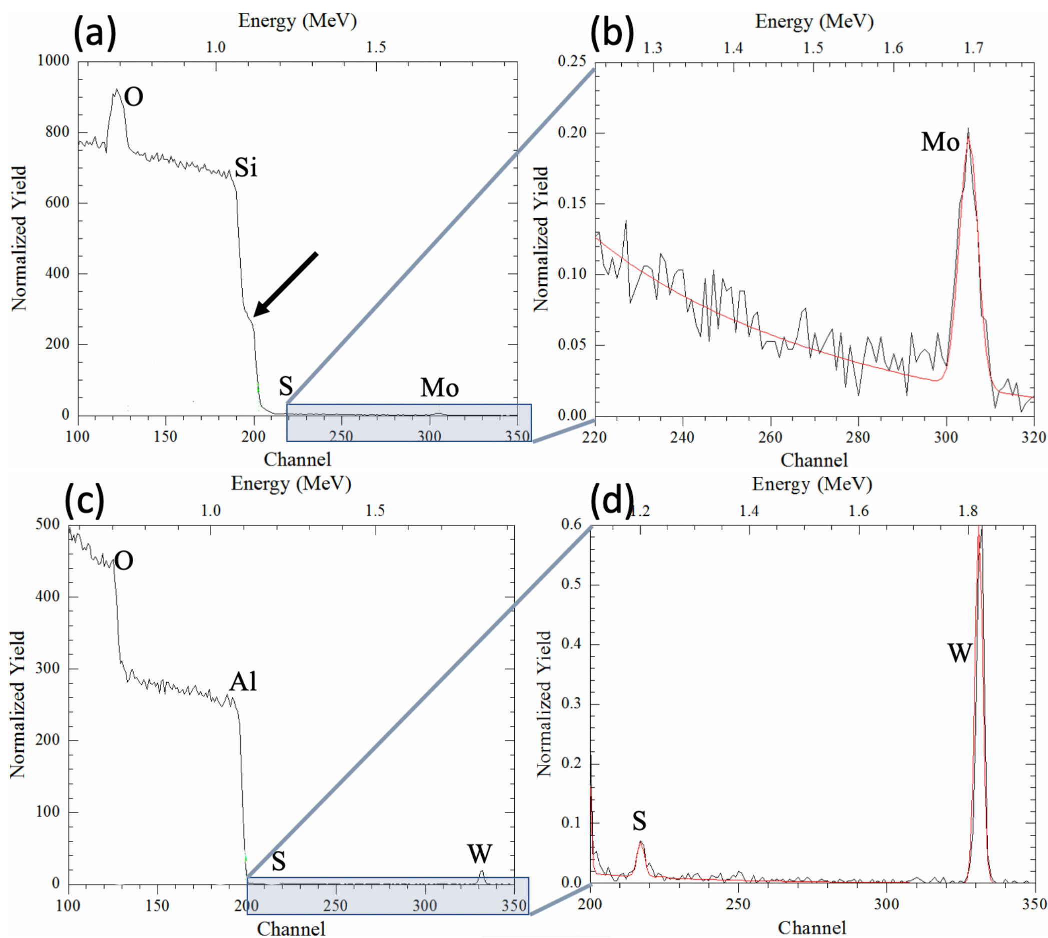

Figure 2.6: (a) RBS spectrum of 0.3 ML of MoS_2 on SiO_2/Si. Channel is given on the bottom and energy on the top. The lower shoulder of the Si peak, indicated by the arrow, obscures the S peak, making quantification of S in sub-monolayer films nearly impossible using RBS. (b) Region constrained to 1.22 MeV to 1.78 MeV to better show the Mo peak in (a). The superimposed red line is a sample fit from RUMP used to determined coverage. (c) RBS spectrum of 0.2 ML of WS_2 on Al_2O_3. Note the difference in the substrate signal between (a) and (c), energies < 1.2 MeV. (d) Region constrained to 1.1 MeV to 1.93 MeV to better show the W and S peaks in (c). Note that for TMDs grown on Al_2O_3, S was easily quantifiable down to ~ 0.1 ML. Graphs produced using RUMP RBS software.

single layer of WS_2, 1.43 x 10^{15} atoms/cm^2, was used to determine ML coverage of the WS_2 films. Spectra were acquired at the center of the sample and experimentally obtained spectra were analyzed using RUMP.

Coverage was determined using the simulation, "sim", feature of RUMP. This feature allows the user to input a set of parameters, including layer-by-layer elemental concentrations (atoms/cm^2) and produce a simulated spectrum of that parameter set. This simulated spectrum is then superimposed on the acquired data. As the signals from the substrate are very strong, by comparison to the thin-film signals, the parameters are adjusted to match the simulated substrate peaks to the actual substrate peaks. A "good" substrate match is determined by 'eyeball', and indicates that all general parameters (current, energy, etc.) are correct in the simulation. Because of the signal strength from the substrate, there is very little guess-work to this part and thus, very little error. Next, the simulation thickness of the thin-film elements are adjusted to obtain best 'eyeball' fit of the peak in question. The atomic concentration of the simulation film was recorded as the atomic concentration of the sample. It is worth noting that RUMP does have a "fit" feature, but experience showed that significantly better fits were obtainable using the method described. Error bars to this method are obtainable by conducting the same process to the same spectrum multiple times. This was done only a few times to verify the high consistency of this method, yielding an average value ± 0.01 ML, for film coverages of approximately 0.3 ML.

2.4 Raman and Photoluminescence Spectroscopy

Raman spectroscopy is an optical measurement that gives information about vibrational energies of a sample. Vibrational energies in a crystal lattice are determined

by atomic mass, bond ordering, and the molecular geometry. Because of this, vibrational energies of the different phonon modes are distinct to a given material. To obtain these vibrational energies, a collimated beam of photons (in our measurements 2.8 eV from a HeCd laser) is scattered by a sample. The majority of the photons are elastically scattered (Rayleigh scattering), but a small fraction are inelastically scattered (Raman scattering). The scattered photons are collected by a standard Si charge-coupled device (CCD) detector and binned according to their energy. For the inelastically scattered photons, the energy difference between the incident and the measured photons is the Raman shift. Shifts down in energy are referred to as Stokes shifted Raman (after the physicist, Sir George Gabriel Stokes), and shifts up in energy are referred to as anti-Stokes. Raman shifts presented in this dissertation are all Stokes shifted Raman shifts. Peaks in the obtained spectra correspond to the distinct vibrational energies of the material (most commonly presented in wavenumbers, cm^{-1}).

In this study, Raman spectroscopy was employed to measure the peak difference between the E^1_{2g} and A_{1g} Raman-active phonon modes in order to confirm single-layer TMD growth. These phonon modes are shown in Fig. 2.7(a). For both MoS_2 and WS_2 as the number of layers in the film increases, the Raman peak separation, Δ, between the E^1_{2g} and A_{1g} Raman-active phonon modes increases. The spectrum acquired for single-layer MoS_2 is given in Fig. 2.7(b). The E^1_{2g} and A_{1g} mode peaks characteristic of single-layer MoS_2 lie at 385.0 cm^{-1} and 404.9 cm^{-1}, respectively, with a Δ of 19.9 cm^{-1} [71,85]. For single-layer WS_2, $\Delta = 62.0$ cm^{-1}, with E^1_{2g} and A_{1g} peaks at 356 cm^{-1} and 418 cm^{-1}, respectively [71,86-87]. It is worth noting the difference in the shift between the E^1_{2g} and A_{1g} Raman-active phonon modes in Fig. 2.7(b). As might be expected, the out-of-plane

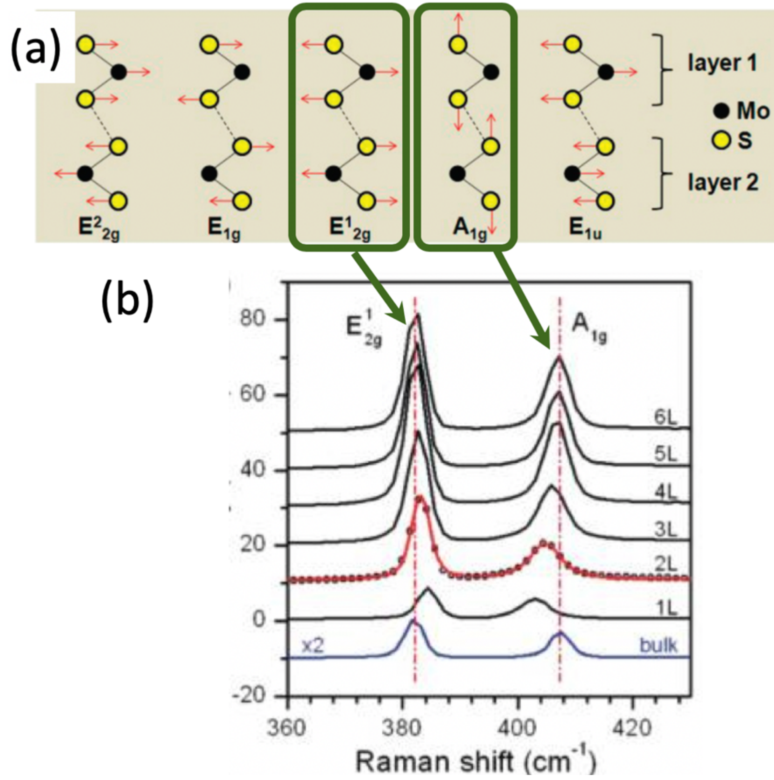

Figure 2.7: (a) Shows the Raman-active phonon modes of MoS_2 (E^2_{2g}, E_{1g}, E^1_{2g}, and A_{1g}) and the IR-active mode, E_{1u}. The two modes investigated, E^1_{2g} and A_{1g}, are boxed and arrows direct to the corresponding peaks in the Raman shift spectra (b) for thicknesses of MoS_2 from exfoliated single-layer, 1L, to bulk. Spectra from the 1L film and the bulk material are plotted side-by-side to highlight the shift in the two Raman modes and the corresponding change in the separation between them, Δ. Figure adapted from ref [85].

phonon mode, A_{1g}, is more affected by the addition of layers than the in-plane mode, E^1_{2g}.

The bandgap of the TMD nanocrystals was measured using photoluminescence spectroscopy (PL). PL, or fluorescence, occurs when incident light is absorbed by the sample. In the case of semiconductors, the absorbed energy excites electrons in the atoms from the valence band to the conduction band. When these relax, photons are emitted with an energy equal to the energetic difference between the conduction band minimum and the valence band maximum, in other words, with the bandgap energy, E_g. Single-layer MoS_2 is typically reported to exhibit an E_g of ~1.85eV and WS_2 a bandgap of ~1.95 [5-7].

For both the Raman and PL measurements, films were excited by 150 μW of collimated 442 nm light from a HeCd laser. Higher intensity incident beams, 300 μW and higher, were found to irreversibly damage the sampled area resulting in a time dependent decrease in intensity of both the Raman and PL signals. Both Raman and PL spectra were obtained at room temperature using a minimum acquisition time of 4 min for Raman spectra and 10 min for PL.

2.5 Auger Electron Spectroscopy

As discussed above, quantities of S were difficult to measure on the SiO_2/Si substrate using RBS, which precluded the use of RBS for stoichiometry measurements on SiO_2/Si. A further limitation of the RBS was the inability to easily manipulate the sample to acquire spectra across the surface of the sample, a valuable means of determining uniformity across the growth surface. Therefore, elemental composition was further quantified using Auger electron spectroscopy (AES).

AES operates by impacting a sample with high energy, 2keV, electrons. These electrons are energetic enough to knock off inner shell electrons, which leave a vacancy in the inner atomic shell. An outer shell electron relaxes to fill the vacancy, emitting a high energy, x-ray, photon equal to the energy difference between the shell states. Sometimes, these high energy x-rays are absorbed by outer shell electrons, exceeding their work function energies, causing them to be emitted as Auger electrons. The energy of these electrons is related to the energy of the x-ray photon emitted when higher-orbital electrons in the atom relaxed to the lower energy states. As the energies of these states are elementally specific, the Auger electrons can be used to determine elemental composition of the target sample. The peaks between 50 eV and 2 keV in Fig. 2.5 are representative of the Auger electrons as they appear in an electron energy spectrum.

For this dissertation, AES was conducted in a separate UHV system with a base pressure in the 10^{-10} Torr range. This system houses a Perkin Elmer PHI 10-155A single-pass cylindrical mirror analyzer (CMA) equipped with a coaxial electron gun. The electron gun produces a ~50 μm diameter electron beam that is incident on the sample at energies between 0.1 and 5 keV. For the spectra discussed herein, we employed a primary electron energy of 2 keV. The CMA analyzes electrons emitted from the near-surface region of the sample to produce Auger electron spectra with an energy resolution of about 1eV. An X-Y-Z manipulator (Z is parallel to the coaxial primary electron beam direction) enables mapping elemental composition along the sample with precision at the ~ 0.01 monolayer level. Typical acquisition times for spectra with high signal-to-noise ratios that encompassed the S_{LMM} (151 eV) and Mo_{MNN} (186 eV) Auger transitions were 3 minutes.

Auger electron spectra were obtained for MoS_2 by smearing bulk material on a substrate identical to those used for growth. Spectra were then differentiated, dN/dE, to obtain a standard of the peak-to-peak height ratio of the S_{LMM} and Mo_{MNN}, $R = 11.1 \pm 0.4$ for MoS_2 films. This gave us a convenient standard measurement for determining stoichiometry of our sub-monolayer TMDs films. Since the inelastic mean free paths for Mo and S Auger electrons are nearly identical [88], these Auger electrons should attenuate similarly, and this ratio should be valid for MoS_2 layers of any thickness. Low sensitivity to W in AES, combined with the ability to measure S quantities against the Al_2O_3 substrate, meant that AES contributed significantly less to our study of WS_2 films.

Where Auger was used to quantify Mo quantities on the substrate, an Auger spectrum was acquired at the sample center, where the Mo concentration was quantified by RBS. The peak-to-peak height of the Mo Auger signal was then calibrated to the absolute Mo coverage as determined by RBS. Using this calibration, we were able to measure the Mo coverage at any point on the substrate. In addition, since S does not stick to the SiO_2 substrate at the growth temperature unless it reacts with Mo to form MoS_2, we can use the peak-to-peak height of the S signal with the S_{LMM} and Mo_{MNN} peak-to-peak ratio to determine the coverage of stoichiometric MoS_2. By this determination, the coverage of stoichiometric MoS_2 is simply the S_{LMM} peak height multiplied by stoichiometric peak height ratio, R, corrected by the Mo areal density in a single MoS_2 layer.

CHAPTER 3

SYNTHESIS OF MoS_2 USING MoO_3 AND S

As discussed in the introduction, many groups have used MoO_3 and S in hot-wall tube furnace configurations to grow single-layer MoS_2 crystals. Though these methods have met with a good deal of success, they are limited by repeatability and film uniformity. This chapter describes our attempt at using these source materials in a cold-wall CVD system capable of independent control over the growth parameters. Much of the material in this section was taken from our Crystal Growth and Design paper, "Uniform and Repeatable Cold-Wall Chemical Vapor Deposition Synthesis of Single Layer MoS_2" [83].

3.1 Experimental Methods

3.1.1 Chamber Configuration

Fig. 3.1(a) schematically depicts the cold wall CVD reactor implemented for this investigation. As shown in the image of fig. 3.1(b), the reactor was assembled from ultra-high vacuum (UHV) components. A stainless-steel chamber sealed with a combination of metal-sealed conflat and Viton O-ring-sealed Kwik flanges. The 4.5" diameter conflat flanges in the sample chamber were sealed with carefully selected Viton O-rings rather than the copper gaskets commonly used because we found that under growth conditions elemental S reacts with Cu to form a flakey, blue/black deposit, presumably a copper sulfide. This sulfurization of the Cu components also led us to replace Cu electrodes in the chamber with Kapton-coated Cu wires, which afforded some protection from the sulfurous environment and increased the longevity of the components. The system was pumped with a Varian V70D, 60 L/s turbomolecular pump (TMP) backed by a rotary

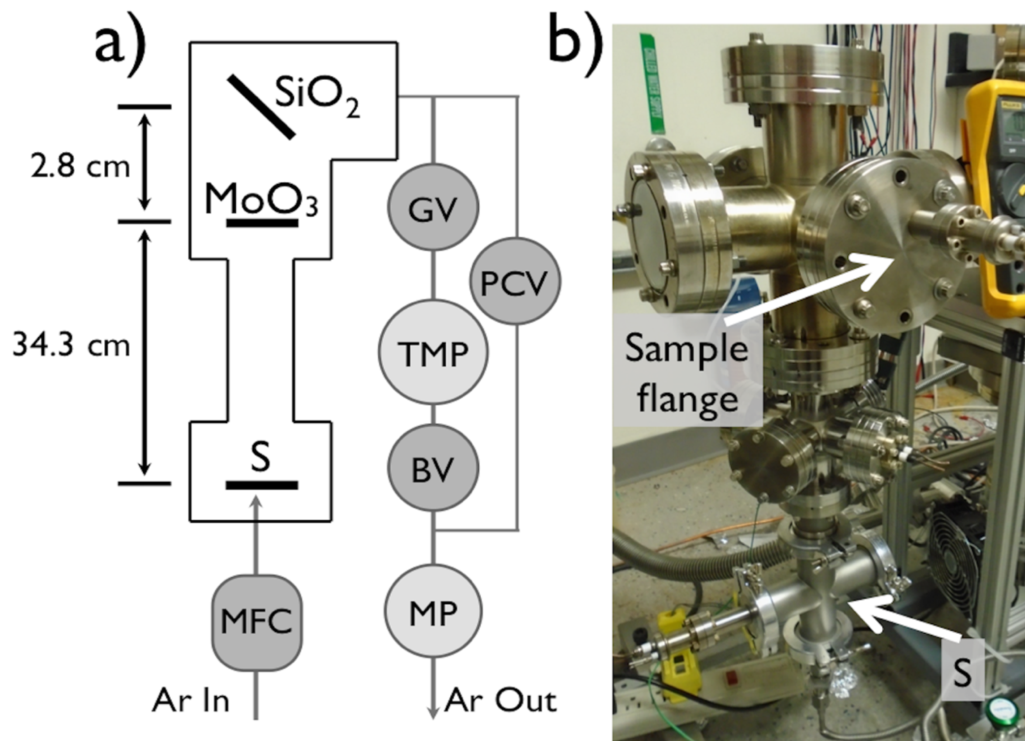

Figure 3.1: (a) Schematic of our cold-wall CVD reactor showing Ar flow path and the location of S and MoO_3 sources relative to the resistively heated substrate (SiO_2). Ar flow was regulated by the mass flow controller (MFC) and the chamber pressure was manually regulated by a downstream pressure control valve (PCV). After pumping to the 10^{-6} Torr range, the turbopump (TMP) was isolated from the chamber and mechanical pump (MP) by closing the gate valve (GV) and backing valve (BV). During deposition, the growth chamber was pumped by the mechanical pump through the PCV line. (b) Image of the CVD reactor. The substrate was mounted to the arrowed 4.5" diameter conflat flange. The MoO_3 source was mounted to the flange at the base of the 4.5" cross. The S source was mounted to the quick flange labeled 'S' in the cross near the bottom of the image. Ar was fed into the base of the quick flange cross so that S vapor is transported past the heated MoO_3 source to the substrate [83].

vane mechanical pump. While the system could easily reach base pressures in the low 10^{-7} Torr range, we typically pumped for about ½ hr after sample insertion to reach pressures in the 10^{-6} Torr range.

It was found early on that flowing Ar and the byproducts of growth directly into the TMP resulted in both a severe limitation on the flows of Ar we could use and unmaintainable wear on the TMP. To circumvent this problem, the TMP was isolated and vented from the gas flow during growth. This was accomplished by closing the gate valve (GV) and the backing valve (BV) seen in Fig 3.1(a). The pressure control valve (PCV) was then opened allowing gases to flow directly into the mechanical pump. An added benefit to this configuration is that the PCV allowed control over the pressure in the chamber. Turning the valve toward the closed position slightly closed the aperture, reducing gas conduction through the valve and raising the upstream pressure. We found that heating the PCV to > 170°C during growth minimized evaporant condensation on the valve, allowing for a stable pressure to be maintained throughout the growth. Pressure was monitored using a 1,000 Torr full-scale capacitance manometer. It was found that leaving the capacitance manometer exposed during growths resulted in a change in the manometer's calibration. For this reason, the capacitance manometer was isolated during growth.

The system was designed to enable independent control over all growth parameters: substrate temperature, S and MoO_3 source temperatures, and Ar carrier gas flow rate into the chamber and pressure. Substrates were resistively heated using direct current and their temperature monitored using an infrared (IR) pyrometer operated in 2-

color mode. We estimate that sample temperatures are accurate to within ± 10°C. The MoS_2 films were grown by thermal deposition of 99.9995% MoO_3 and 99.999% S (Alfa Aesar) from alumina-coated W baskets in a flowing Ar (99.999%) ambient. The MoO_3 and S sources were mounted 2.8 cm and 34.3 cm from the substrate, respectively. The Ar carrier gas flow was controlled using a 500 sccm (1 cubic centimeter per minute at standard temperature and pressure) full-scale mass flow controller (MFC).

Fig. 3.2 is an image of the special flange designed to hold the MoO_3 alumina source basket. This flange was designed to house and heat four separate source baskets and was mounted to the bottom of the 6-way 4.5" cross visible in Fig. 3.1(b). Initial experimentation was conducted with the S and the MoO_3 baskets mounted on this flange, 2.8 cm from the substrate, but radiative heat from the hot sample and MoO_3 alumina basket made it difficult to control the temperature of the S basket. We attempted to mitigate this effect by employing various lengths of posts (visible in Fig 3.2), to try and separate the sources and move the S away from the sample, and by adding radiation shields (not shown) between the source baskets. Where these changes improved the controllability of the S basket temperature, it was eventually determined necessary to move the S 34.3 cm upstream of the sample to the location in Fig 3.1(b).

Both the MoO_3 and S source temperatures were feedback controlled by separate Eurotherm proportional-integral-derivative (PID) controllers. The source temperatures were sensed by thermocouples bonded to the underside of alumina-coated W baskets with vacuum-compatible epoxy. A K-type thermocouple was used for the S basket and a S-type was used for the MoO_3. We found it necessary to use an S-type for the MoO_3 basket

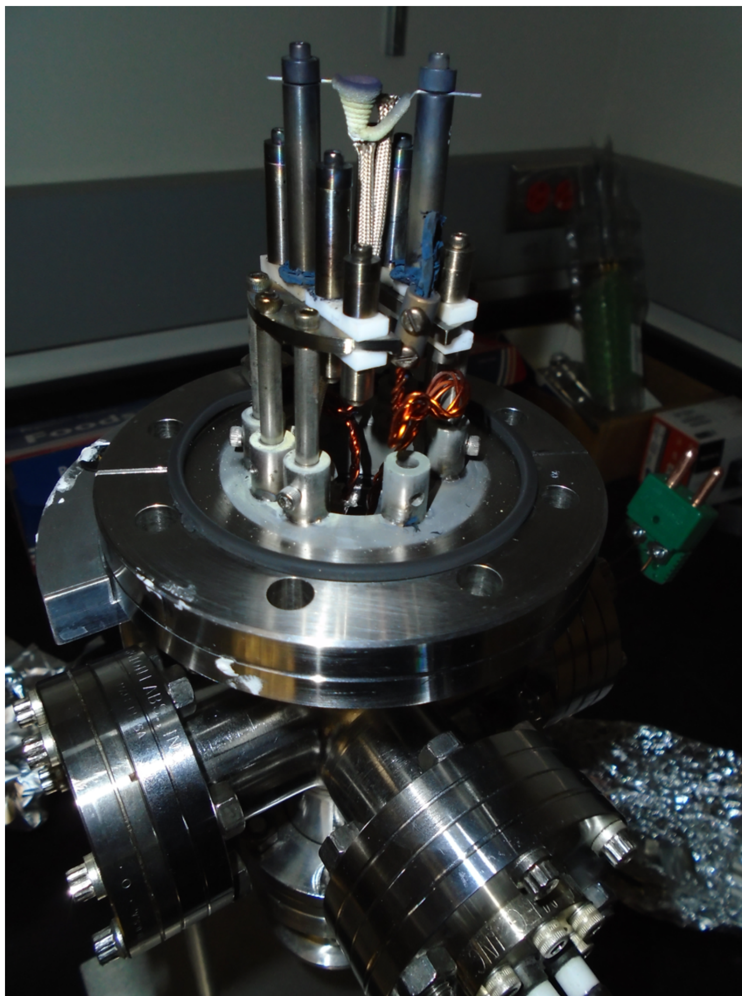

Figure 3.2: Flange specially designed to hold the alumina coated source baskets close to the sample. This flange was mounted to the bottom of the 6-way 4.5" cross seen in Fig. 3.1. Visible in the image are the alumina-coated basket used to hold the MoO_3 powder, the Kapton-coated Cu wires used for electrical conduction and the Viton-O-rings used in place of the typically employed Cu gaskets.

because sulfurization of the K-type thermocouple at the higher basket temperatures led to breakage and unreliable temperature readings after a couple of growths.

3.1.2 Sample Preparation

MoS_2 films were grown on 4 mm x 20 mm substrates cleaved from 3" diameter Si wafers with a 100 nm-thick furnace-grown dry oxide layer, grown by ASU's Center for Solid State Electronics Research staff under cleanroom conditions. Prior to each growth, the SiO_2/Si substrates were chemically cleaned using a standard cleanroom protocol by being first loaded into a specially designed polytetrafluoroethylene (PTFE) holder. The sample/holder was then submerged in a >70°C piranha etch solution (3:2, H_2SO_4:H_2O_2) for 20 min, then swirled in a 5% hydrofluoric acid (HF) in water solution for 30 sec. Following the chemical etchants, the sample was rinsed for 10 min in flowing 18 MΩ-cm water. The sample and PTFE holder were then transferred to a 3" deep Pyrex container where the sample could be carefully removed from the PTFE holder, while staying submerged in 18 MΩ/cm H_2O. This was done to minimize the amount of time H_20 had to air dry on the sample. Immediately after removing the sample from the Pyrex container, it was dried with N_2. The samples were then clamped between Ta electrodes and loaded into the growth chamber so that the growth surface made a 45° angle with the direction of Ar flow, as shown schematically in Fig. 3.1(a). Once loaded, and before growth, the sample was also cleaned by sequential degassing. This was accomplished by resistively heating the sample from room temperature to 775 °C in 100° increments for 10 min at each increment.

3.1.3 Growth Parameters and Procedure

While using this chamber configuration, we systematically varied growth parameters in order to assess their effects on film morphology and uniformity. As detailed below, this capability also enabled us to identify growth parameters that produced the highest run-to-run repeatability of MoS_2 coverage at the precision of a few hundredths of a monolayer (ML). Additionally, in favorable cases, the MoS_2 coverage was uniform (to within 0.01 ML) over several square mm regions of the substrate. Sample temperature was varied in the range 650-825 °C. The MoO_3 source temperature was varied in the range 550-600 °C. The sulfur source temperature was first increased to 80 °C, then to a maximum temperature which we varied in the range 110-250 °C over a ramp-up time which varied between 2 and 4 min. Ar pressure and flow were varied in the range 10-300 Torr and 25-250 sccm, respectively.

We found it essential to perform the following procedure between growths to ensure consistent run-to-run repeatability. Prior to each growth, any material remaining the in the MoO_3 basket was removed mechanically. A sacrificial Si strip, identical to a growth substrate, was inserted into the sample holder. The strip was resistively heated to 830 °C while the MoO_3 basket was heated to 740 °C for > 1 hour. This procedure was performed under high vacuum conditions. Likewise, the S basket was heated to 325 °C for 30 min under a flow of 50 sccm Ar in the mTorr pressure range. This procedure eliminated any spurious Mo or S deposition from evaporants that had condensed on the sample holder and baskets. Fresh source material was then loaded into the source baskets before each growth: 20 ± 2 mg of MoO_3 and > 200 mg of S.

Growth runs were initiated after pumping the chamber for ≥ 30 min to reach a pressure in the 10^{-6} Torr range. From this state, the backing valve and gate valve were

closed to isolate the TMP from both the growth chamber and mechanical pump. The TMP was then switched off and vented to atmospheric pressure with N_2. Ar flow was then initiated, simultaneously opening the PCV to allow the reactor to be pumped by the mechanical pump. Ar was first flowed at 25 sccm until growth chamber pressure increased to approximately 20 Torr. Under these conditions, the sequential degas cleaning described above was executed and we began heating the PCV. Sample temperature was monitored using an infrared (IR) pyrometer operated in 2-color mode. After the sequential degas, the sample was cooled to room temperature (RT).

Once the sample had cooled and the PCV had reached 170°C, typically about 30 min, the Ar flow rate was increased to its desired value and the PCV gradually closed until the desired growth pressure was reached. The pressure was monitored for ≥ 10 min to verify its stability over a time interval similar to that required for growth. The capacitance manometer was then isolated from the growth chamber. The sample and source temperatures were simultaneously increased using profiles similar to those displayed for a typical growth run in Fig. 3.3. After material deposition, the sample was cooled to RT in flowing Ar. After sufficient cool-down, approximately 30 min, the sample was removed from the chamber for analysis.

3.1.4 Characterization Methods Used

Samples for this study were primarily analyzed using scanning electron microscopy (SEM), Rutherford backscattering spectrometry (RBS) and Auger electron spectroscopy. SEM images were used to determine film morphology and analyzed to obtain the nucleation density and average feature size of the film. This was done using the "density slice" and "analyze particles" features of the software ImageJ [82], which

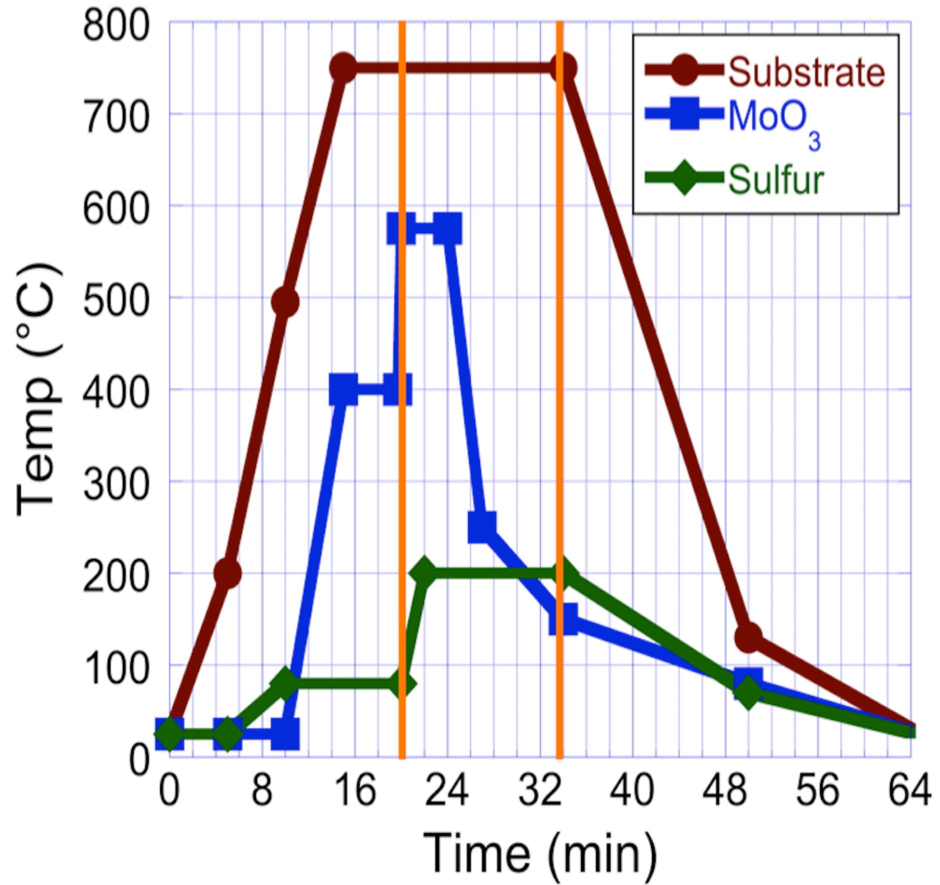

Figure 3.3: Typical substrate and source temperatures vs. time. During times t < 0, Ar flow is established and the chamber pressure is stabilized. The vertical orange lines delineate the time interval for which there was material flux from the source baskets. After growth (t > 34min), the sample is cooled to room temperature in flowing Ar [83].

were used to isolate the features from the background and determine the area of each feature. A comparison of the sum of areas of the features to the area of the image gave a % covered by features. Since 1 ML of single-layer film corresponds to 100% coverage of the SEM image, this % corresponded to the ML coverage of features. RBS was done to quantify the amount of Mo present on the substrate and, when quantities of S were great enough to be resolved against the SiO_2 signal, to check film stoichiometry. Because of the difficulty in obtaining a quantification of S in our films and the inability to translate the sample in the RBS chamber, AES was done to determine stoichiometry and composition as a function of position along the sample.

Atomic force microscopy (AFM) was used to verify that the height of the MoS_2 features matched reports of single-layer MoS_2 from the literature and was used to quantify the layers of multi-layered films. Layers were further quantified using the spacing between the in- and out-of-plane, E^1_{2g} and A_{1g}, vibrational modes obtained from Raman spectroscopy. Photoluminescence spectroscopy (PL) was done to verify the bandgap of our MoS_2.

3.2 Results and Discussion

Fig. 3.4(a) shows a SEM image of typical MoS_2/SiO_2 nanocrystals grown using the chamber configuration and technique presented here. The nanocrystals are evident as dark features on a lighter SiO_2 substrate. The sample shown in Fig. 3.4(a) was grown at an Ar pressure of 50 Torr at a flow rate of 150 sccm following the substrate and source temperature vs. time profiles shown in Fig. 3.3. To confirm that these nanocrystals were single-layer MoS_2, we acquired the Raman spectrum shown in Fig. 3.4(b). The in- and out-of-plane, E^1_{2g} and A_{1g}, vibrations characteristic of MoS_2 are evident at 385 and 404.9

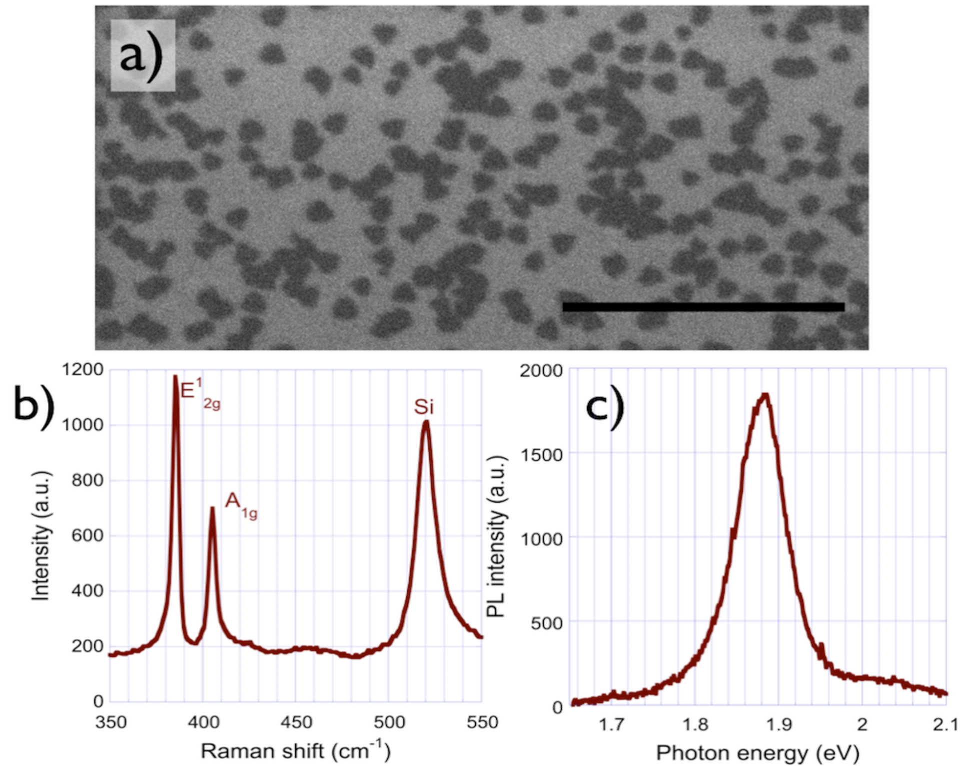

Figure 3.4: (a) SEM image of a sample grown using the temperature vs. time profile shown in fig. 2 using P = 50 Torr Ar at a flow rate of 150 sccm. The scale marker is 500 nm. (b) Raman spectrum of the sample shown in (a). The energy difference, Δ, between the E^1_{2g} (385.0 cm^{-1}) and A_{1g} (404.9 cm^{-1}) Raman peaks of MoS_2 is 19.9 cm^{-1} indicating that the nanocrystals are single-layer MoS_2. The Si substrate Raman peak is evident at 520 cm^{-1}. (c) photoluminescence spectrum of the same area showing a peak energy of 1.88 eV [83].

cm^{-1}, respectively. Previous work has shown that the difference, Δ, between the maxima of these peaks increases with the number of MoS_2 layers [14,23,36,44,85,89]. Δ values for monolayer MoS_2 have been reported to range from 17 to 20.6 cm^{-1} (see chapter 2 section 4). The Δ value of 19.9 cm^{-1} evident in the spectrum presented in Fig. 3.4(b) thus indicates that the nanocrystals in Fig. 3.4(a) are single-layer MoS_2. Unless otherwise stated, all 2D samples presented in this chapter, which exhibit these dark contrasted discrete features, showed similar Δ values indicative of single layer MoS_2.

Fig. 3.4(c) shows a photoluminescence spectrum acquired at the same area from which the Raman spectrum, shown in fig. 3.4(b), was acquired. The peak energy in this photoluminescence (PL) spectrum is at 1.88 eV. Experimental values have been reported in the range of 1.81 to 1.9 eV [5,6,36,44,89-94]. Interestingly, the PL peak energy has been observed to increase at the edges of and boundaries between ~ 15 μm diameter crystallites grown by CVD (with a maximum of 1.87eV) [33]. For our relatively small features, a 1 μm diameter excitation beam averages PL from many islands, their edges and the junction between those that have impinged during growth. The edge contribution to the PL for our smaller islands is greater than for the larger features of ref. 33, thus it is likely responsible for our measured PL value being on the higher energy side of the reported values.

Unless otherwise stated, all 2D samples discussed here exhibited similar Raman and PL behavior. For samples with significantly different average feature sizes, we have found that the Raman intensity normalized by the total MoS_2 area seems to depend on the average feature size. We have also found that after a month under ambient conditions,

both Raman and PL intensity have significantly decreased, in agreement with previous reports [59].

It was also straightforward to test the single-layer nature of grown features using atomic force microscopy (AFM). A line-scan height profile of the feature shown in the AFM image of Fig. 3.5(a) shows the feature to be ~ 0.7 nm in height, the expected height for single-layer MoS_2. As will be discussed below, certain growth conditions yielded multi-layer features. A line-scan height profile of the feature in Fig. 3.5(d) of the AFM image in Fig. 3.5(c) show a feature height of ~ 1.4 nm, double that seen in Fig. 3.5(b). In this study, feature height was always measured to be a multiple of the single-layer height.

The capability to independently vary growth parameters enabled us to individually assess their effects on film morphology and uniformity and identify optimum growth conditions. It is commonly believed that S reacts with heated MoO_3 forming suboxides either at the MoO_3 source, in the gas phase or on the substrate. The Mo suboxides that reach the surface are then believed to further react with S to form MoS_2. In an attempt to identify the sequence of events leading to MoS_2 formation on heated SiO_2, we adjusted the timing of S deposition relative to that of the MoO_3 heating cycle. Even with our capability for independent control over deposition parameters, a systematic investigation was inconclusive. We found that MoS_2 formed on the heated SiO_2 surface if the MoO_3 was pre-deposited and then 'sulfurized' at an elevated temperature, seemingly identically to the concurrent deposition of S and MoO_3. Depositing S for 15 min prior to the MoO_3 deposition also formed 2D MoS_2 nanocrystals. While we have not systematically investigated this behavior, we tentatively believe that it is most likely a result of remnant S desorption from the cold-wall system.

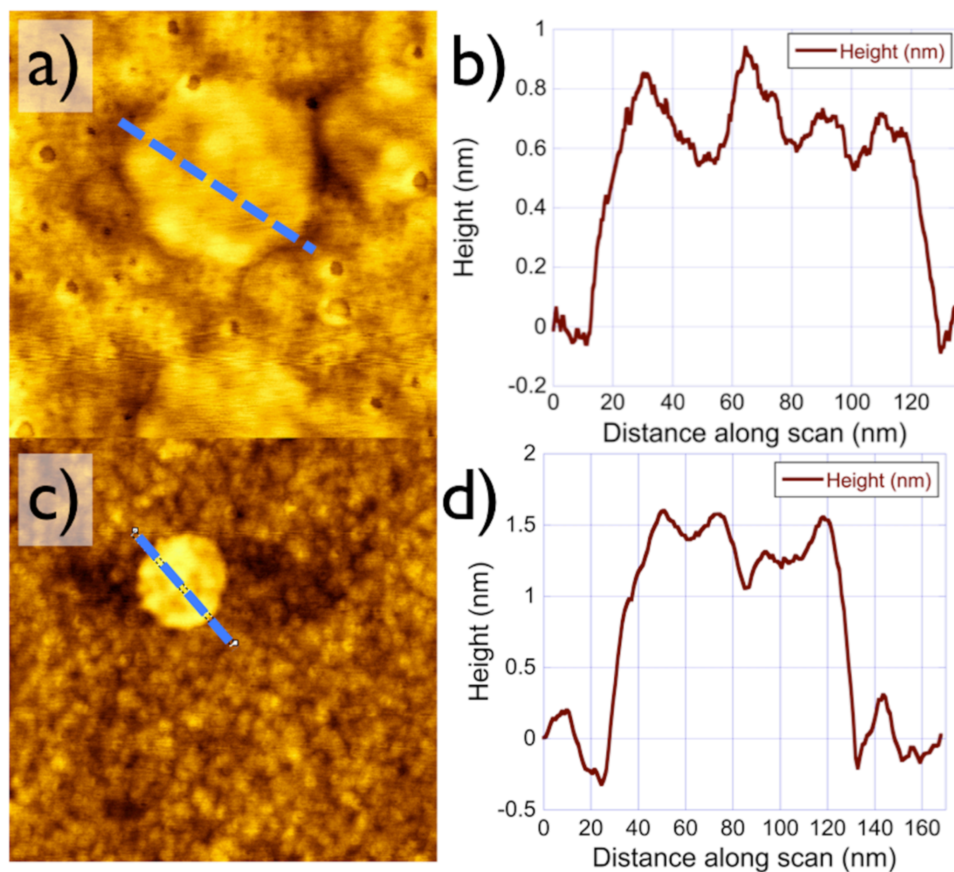

Figure 3.5: (a) 250 nm x 250 nm AFM height image of typical MoS_2 nanocrystals produced by our synthesis method. (b) corresponding line-scan along the line indicated in (a) shows a nanocrystal height of ~ 0.7 nm, the expected height for single layer MoS_2. (c) 500 nm x 500 nm AFM height image of sample grown at an Ar pressure of 10 Torr. (d) shows the line-scan height profile along the line indicated in (c) indicating a 2 ML high nanocrystal as discussed in the text [83].

Our observation that single-layer MoS_2 can be grown by sulfurization of pre-deposited MoO_3 is similar to behavior previously observed by other investigators. MoS_2 has been grown by tube furnace sulfurization of drop-cast MoO_3 nanoribbons [26] or thermally deposited MoO_3 films [27-28]. We found that concurrent deposition of S and MoO_3, following the time vs. temperature profiles shown in Fig. 3.3, yielded the most uniform films and provided the best control over MoS_2 film coverage. As a consequence, all results reported here employed this deposition sequence.

Subsequent to identifying the optimum timing for S and MoO_3 deposition, we correlated variations of other deposition parameters with sample morphology. Systematic variation of the Ar pressure during growth enabled us to determine that pressures greater than 100 Torr produced the most uniform MoS_2 films. We assess MoS_2 uniformity by measuring the average nanocrystal size, areal density and coverage from SEM images acquired every 2 mm along the substrate. For pressures in the 100 to 300 Torr range, we observed no significant variation in these parameters as the Ar pressure was varied for different growth runs. Typical values for nanocrystal density were in the mid 10^9 cm^{-2} range with an average size in the few 10s of nm range. The single-layer MoS_2 islands typically covered about 20% of the substrate.

Interestingly, a reduced Ar growth pressure produced a marked effect on film morphology. When we reduced the Ar pressure to below 30 Torr, the average nanocrystal size increased to 160 nm, the density decreased by 2 orders of magnitude to 2 x 10^{-7} cm^{-2} and the nanocrystals covered only 5% of the substrate area (see Fig. 3.6). For these lower pressure growths, we observed a much larger discrepancy between the total area of MoS_2 nanocrystals observed in SEM and the Mo coverage measured by RBS at the sample

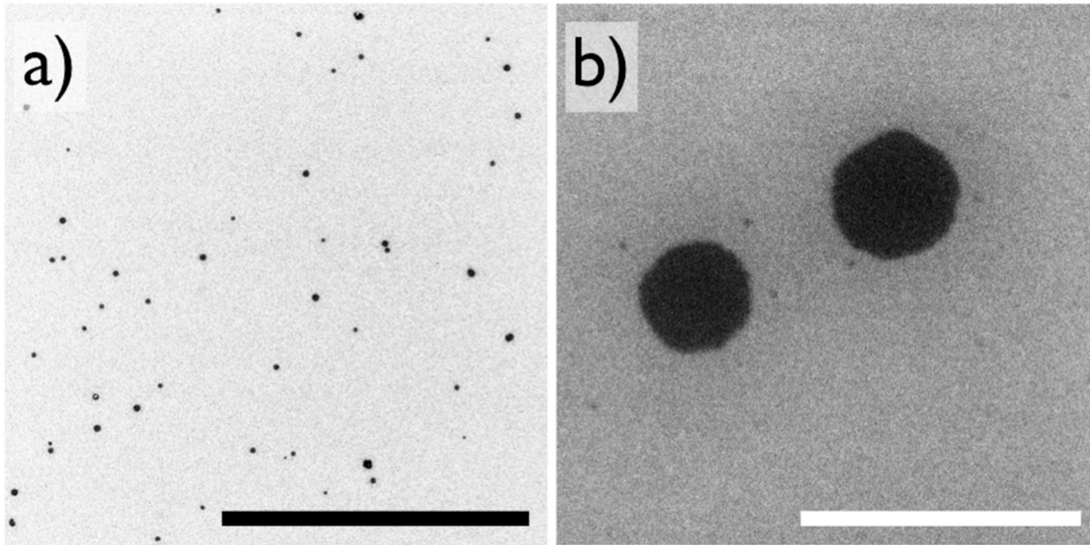

Figure 3.6: SEM images showing the relatively large features grown with a low nucleation density across the substrate at Ar pressures ≤ 30 Torr. Scale bars are 10 μm in (a) and 500 nm for (b) [83].

center, which was 0.28 ML (corresponding to a coverage of 28%). AFM indicates that these islands are not single-layer, but double-layer MoS_2, as shown Fig 3.5(c) and (d). A Δ value of 25.4 cm^{-1} obtained by Raman, confirms that these nanocrystals are thicker than a single layer. Note that the increased height of the features to 2 ML still only accounts for roughly a third the Mo coverage measured by RBS.

Over the pressure range investigated, we speculate that Ar pressure affects MoS_2 growth primarily by suppressing S evaporation. Between 30 and 300 Torr, the mean free path of Ar decreases by an order of magnitude from about 5 to about ½ µm, which is much smaller than any relevant growth chamber dimension. So, all growths in this pressure range occur in the continuous gas flow regime. However, in the same pressure range, evaporation rates decrease by about an order of magnitude [95-96]. As a consequence, the S delivery rate to the substrate may be more stable during deposition at higher pressures. In addition, the S residence time on the substrate likely increases with pressure, providing greater opportunity for reaction with deposited Mo suboxides to form MoS_2.

We also note that our cold-wall CVD approach will significantly suppress gas-phase reaction between S and MoO_3 and its sub-oxides in comparison to the majority of previously reported work that employed hot-wall reactors. As a consequence, in our work most of the reaction between S and MoO_3 occurs either on the substrate or at the MoO_3 source, which is 'downwind' from the S source and upstream from the sample, as shown in Fig. 3.1. There is likely some gas phase reaction in the hotter portions of the inhomogeneous temperature region surrounding both the MoO_3 source and substrate and the cooler surroundings. However, reaction rates are exponentially dependent on

temperature, so they will be most rapid near the substrate and MoO_3 source. As a consequence, we speculate that thermal gradients in the Ar carrier gas may not significantly contribute to the observed film morphologies.

We subsequently varied the MoO_3 source temperature to determine its optimum value. The results obtained are summarized in Fig. 3.7. Fig. 3.7(a) shows that, as would be expected, increasing the MoO_3 source temperature increased the quantity of Mo deposited onto the substrate. Figs. 3.7(b)-(d) show that as the source temperature, and consequently the flux, increased the morphology evolved from small triangular 2D clusters to larger 2D features with multifaceted, often irregular, edges. Further increase of the MoO_3 flux leads to a bimodal distribution comprised of 2D islands, similar to those shown in fig. 3.7(c), and 3D features. These 3D features appear with lighter contrast in Fig. 3.7(d). With the larger amount of material on the sample, it was possible to use RBS to quantify the S coverage. These measurements revealed that in spite of the increased quantity of Mo on the substrate, the material shown in fig. 3.7(d) is stoichiometric MoS_2. These 3D clusters are readily apparent in the cross-section SEM image of this sample, which is provided in Fig. 3.8(b). It is noteworthy that an order of magnitude increase in Mo flux did not drastically change the nucleation density, as would be expected by standard growth models.

To assess run-to-run consistency of this growth method, we grew a series of four samples using the temperature vs. time profiles shown in Fig. 3.3 at an Ar pressure of 100 Torr and flow rate of 150 sccm. Fig. 3.9 displays SEM images acquired from the center of each of these samples. Analyzing these SEM images and those acquired over larger nearby areas enabled us to determine the fraction of the substrate area covered by MoS_2

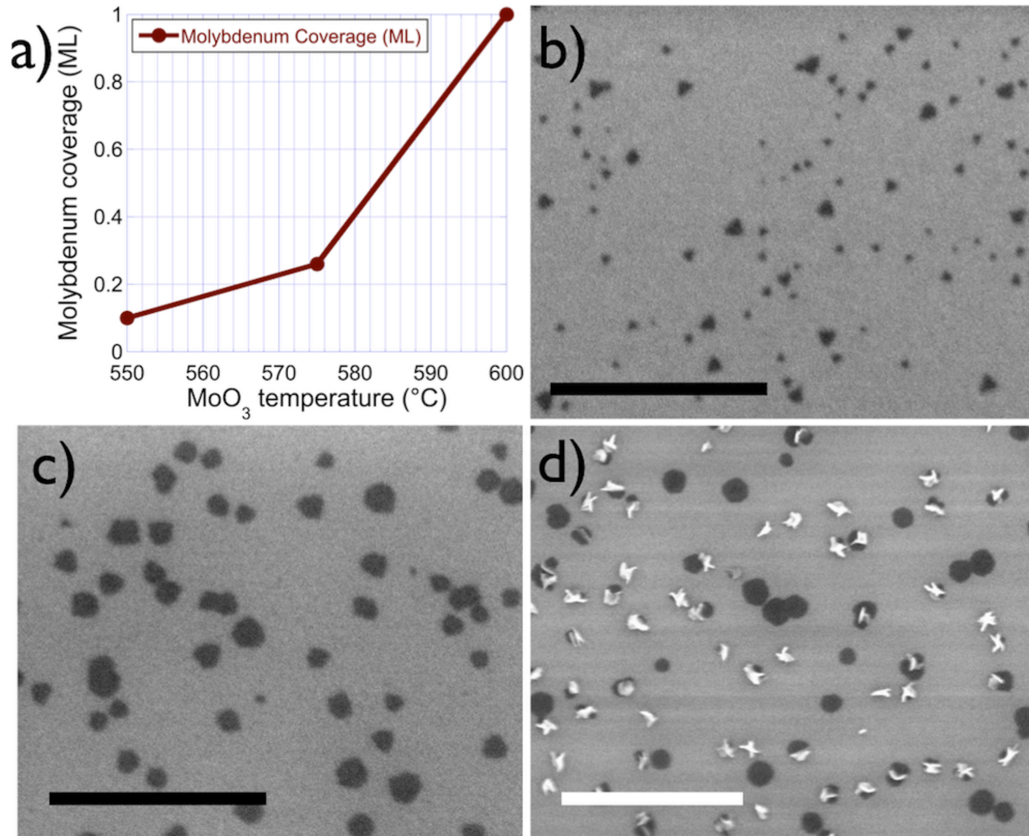

Figure 3.7: (a) plots the variation in Mo coverage at the center of the sample, measured using RBS vs. MoO_3 source temperature for the samples shown in (b)-(d). 1 ML represents the areal coverage of Mo in a single layer of MoS_2. (b)-(d) are SEM images of samples grown at an Ar pressure of 100 Torr and flow rate of 150 sccm using 750°C substrate and 200°C S temperatures. The MoO_3 temperature for each growth was 550 (b), 575 (c), and 600°C (d). In (b) and (c) the black scale bars represent 500 nm. In (d), the white scale bar is 1 μm [83].

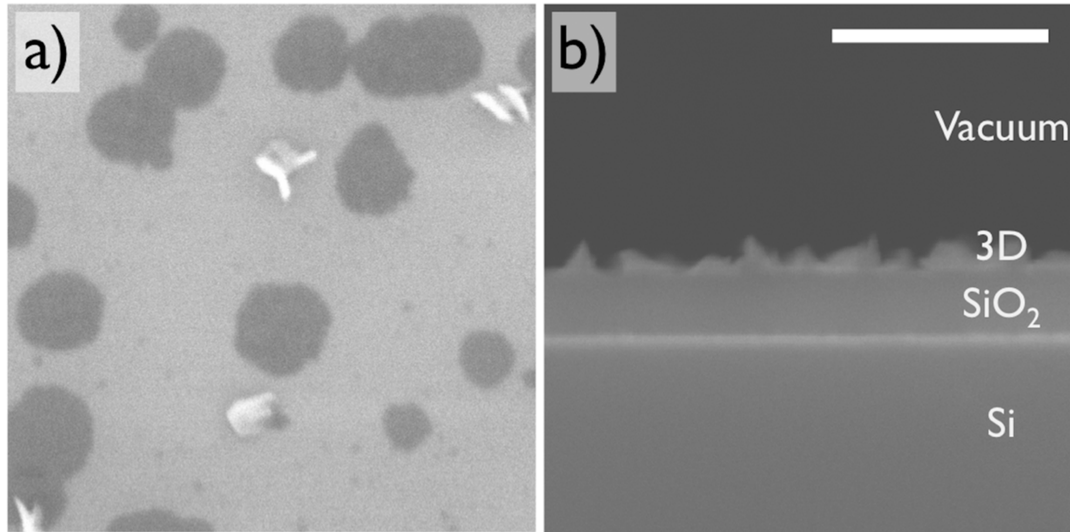

Figure 3.8 : SEM images of sample exhibiting both 2D and 3D features. (a) plan view and (b) cross-section SEM image. In (b), the SiO_2/Si substrate is labeled. 3D refers to the three-dimensional nature of the white features evident in (a), which have an average height of ~30 nm above the SiO_2 surface. The white scale bar is 300 nm for both images [83].

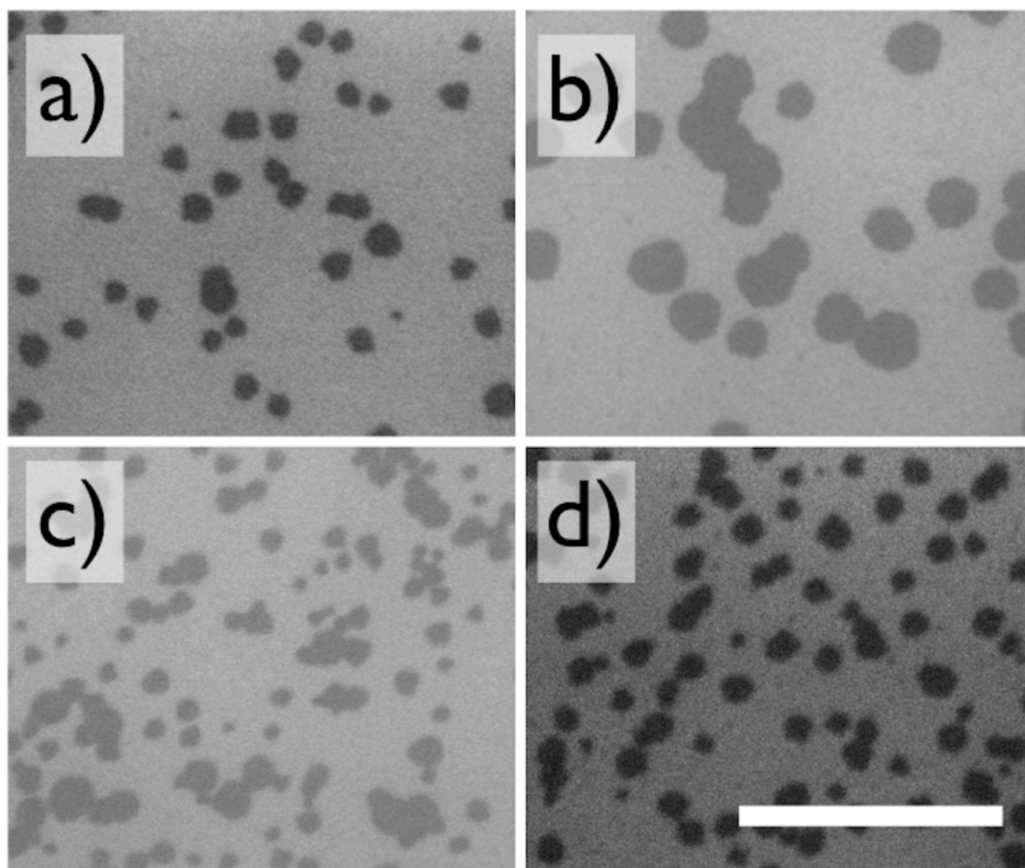

Figure 3.9: SEM images of 4 samples grown using an Ar pressure of 100 Torr and flow rate of 150 sccm with the temperature vs. time profile shown in Fig. 3.3. The average fraction of substrate area covered by the dark MoS_2 nanocrystals is 0.18 and is consistent to within ±0.03 ML for these samples. RBS detects a larger amount of Mo than can be accounted for by the area of the MoS_2 nanocrystals. While run-to-run coverage is very consistent, the nanocrystal size and nucleation density vary significantly between growths. The scale bar represents 500 nm for all images. Statistical analysis of these samples is shown in Table 3.1 [83].

nanocrystals as well as the nanocrystal nucleation density and average size. For each of these samples, an area 1.5 µm x 1.5 µm was imaged containing a minimum of 200 nanocrystals. We also determined the areal coverage of Mo at the center of the sample using RBS, which averaged over a 1 mm diameter beam. RBS consistently detects more Mo than can be accounted for by the MoS_2 nanocrystals evident in the SEM images. The results of these SEM and RBS measurements are summarized in Table 3.1.

Fig.	SEM	RBS	Size (nm)	Density (cm^{-2})
3.9(a)	0.14	0.26	26.0 ± 6.0	5.91×10^{9}
3.9(b)	0.19	0.33	44.6 ± 8.9	2.88×10^{9}
3.9(c)	0.19	0.30	17.4 ± 8.4	1.63×10^{10}
3.9(d)	0.19	0.30	22.5 ± 6.1	1.13×10^{10}
Average	0.18 ± 0.03	0.30 ± 0.03	27.6 ± 11.9	$9.1 \pm 5.1 \times 10^{9}$

Table 3.1: Summary of coverages measured by SEM and RBS at the center of the substrate, average MoS_2 nanocrystal size and nucleation density for the samples shown in Fig. 3.9. The SEM coverage values are the fraction of substrate area covered by MoS_2 nanocrystals. The RBS coverage values represent the fraction of substrate area that would be covered by single-layer MoS_2 nanocrystals containing the amount of detected Mo. The nanocrystal sizes are the radii of circles whose areas equal those of the features in the SEM images. At least 200 nanocrystals were involved in the statistical analysis of each sample [83].

As indicated in Table 3.1, this growth method yields run-to-run consistency in MoS_2 nanocrystal coverage with a precision near a few percent; i.e., to within a few 100^{ths} of a ML. While the amount of deposited Mo detected by RBS is consistently greater than can be accounted for by the area covered by the MoS_2 nanocrystals in the SEM images, it is also consistent from run-to-run at a similar precision. Despite the consistency in coverage, the nanocrystal size and nucleation density vary significantly from run-to-run.

We also note the difference in average size, nucleation density and shape between MoS_2 nanocrystals grown using our cold-wall method and those appearing in the literature. The most commonly reported MoS_2 crystallites grown using hot-wall CVD are triangular and can reach lateral dimensions up to 100 μm [33]. In contrast, the larger of the MoS_2 nanocrystals reported here are hexagonal, circular or irregularly shaped with lateral dimensions of several 10s of nm. We attribute these differences primarily to growth kinetics and not to some feature peculiar to cold- vs. hot-wall CVD. For example, in ref. 24 a MoS_2 film grown using hot-wall CVD employing growth conditions similar to those used here are circular (see fig. 1(c) of that manuscript). Interestingly, as shown in fig. 3.7(b), nanocrystals grown at our lowest Mo deposition rate are triangular and occupy the smaller end of the size range for those grown using this cold-wall approach. Tripling the Mo deposition rate yields larger, hexagonal and circular nanocrystals as shown in fig. 3.7(c). This observation suggests that the relationship between the MoS_2 attachment and edge diffusion rates enable nanocrystals grown at lower deposition rates to attain the commonly observed triangular shape. Qualitatively, we also expect that higher growth rates would lead to the higher nucleation densities and smaller average sizes reported

here. We speculatively attribute the observed variation to subtle differences in the S flux vs. time during growth. We therefore speculate that a more stable method of delivering S during growth, e.g. gaseous precursors (H_2S [97], diethyl sulfide [39], dimethyl sulfide [98], or di-tert-butyl sulfide [99]), would be beneficial.

The discrepancy between the coverages measured using SEM and RBS was investigated further using AES. The Auger electron spectrum acquired at the center of the sample shown in Fig. 3.9(a) exhibited a S_{LMM} to Mo_{MNN} peak height ratio of 6.7, which is smaller than the value of 11.1 for stoichiometric MoS_2. Thus, AES shows that there is more Mo at the center of the substrate than is required to form stoichiometric MoS_2.

In addition to the run-to-run consistency in MoS_2 coverage demonstrated by Fig. 3.9, this deposition method also yields uniformity of MoS_2 coverage over several square mm areas of the substrate. As discussed in Chapter 2, Analysis Methods Used Throughout, the RBS measurement calibrates the Mo_{MNN} peak height so that it measures the absolute Mo coverage. Also, all S detected by AES is incorporated into MoS_2 nanocrystals so the S_{LMM} peak height is a measure of the stoichiometric MoS_2 coverage. When combined with our capability for translating the sample in the UHV AES system we are able to quantify both the Mo and MoS_2 coverage at any point on the substrate surface and compare its value to that measured by SEM. First, we note that the ratio of the S_{LMM} to Mo_{MNN} Auger peaks are nearly constant at ~7 over the central ~cm long region of the sample shown in Fig. 3.9(a). This result is shown in Fig 3.10 and although it confirms that there is excess Mo, it also indicates deposit uniformity.

Uniformity of the MoS_2 film is summarized in Fig. 3.11. Fig. 3.11(a) displays a series of SEM images acquired at the indicated positions relative to the center of the

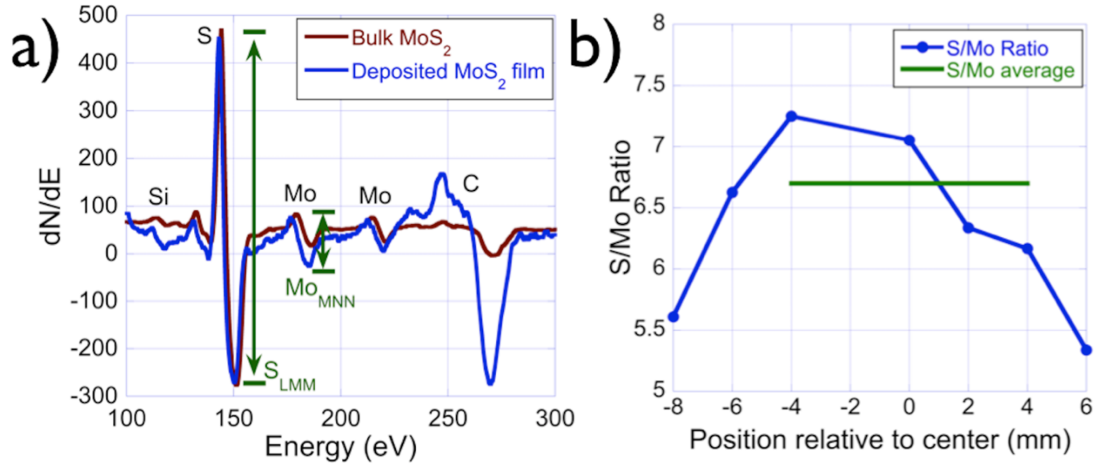

Figure 3.10: (a) The blue curve plots the differentiated dN/dE AES spectrum measured at the center of a sample grown following the temperature vs. time profile shown in Fig. 3.3. The sample was grown at 100 Torr with an Ar flow rate of 150 sccm. SEM images of this sample are shown in Fig. 3.11(a). The red curve in (a) is the dN/dE Auger electron spectrum measured from a bulk standard. The peak-to-peak heights of the S_{LMM} and Mo_{MNN} Auger transitions are identified by the green arrows. Oxygen peaks lie outside the range of the spectrum shown. (b) S_{LMM}/Mo_{MNN} peak height ratio vs. position relative to sample center for the same sample from which the blue curve displayed in (a) was obtained. The green line is the average of the ratios obtained over the points acquired at positions within 4 mm of the sample center. Within this central region, the S/Mo ratio measured using AES varies by about ± 0.5 from its average of 6.7. The S/Mo ratio measured from the bulk standard, is 11.1, which is characteristic of the ratio for stoichiometric MoS_2 [83].

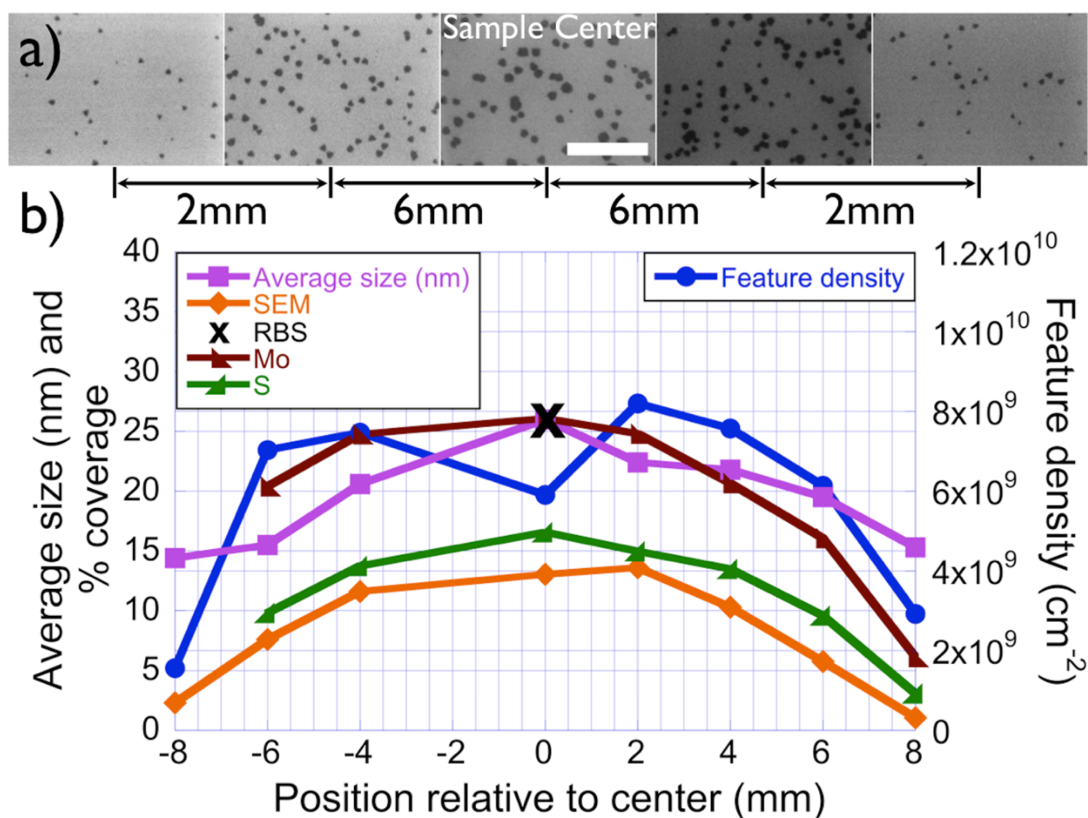

Figure 3.11: (a) SEM images acquired at the indicated positions relative to the center of a sample grown using an Ar pressure of 100 Torr and flow rate of 150 sccm with 750°C substrate, 575°C MoO_3 and 200°C S temperatures. Scale bar represents 500 nm. (b) plots feature density, average size and the fractional coverage of MoS_2 nanocrystals. The fractional coverage of MoS_2 nanocrystals was determined from SEM micrographs similar to those shown in (a), the Mo coverage measured using RBS at the center of the sample (RBS), the Mo coverage measured by AES (Mo) and the S coverage measured by AES (S) [83].

substrate. Fig. 3.11(b) plots the average size of the MoS_2 nanocrystals, their nucleation density and the fraction of substrate area they cover as determined from SEM images similar to those shown in Fig. 3.11(a). These values are compared to the fraction of substrate area covered by MoS_2 nanocrystals that would contain the amount of Mo measured using AES and to the fraction of substrate area covered by MoS_2 nanocrystals that would contain the amount of S measured by AES. Regardless of the measure of MoS_2 coverage, within the central ~cm long region of the 4mm-wide substrate, the MoS_2 coverage varies by only about 6%. Note that the fraction of substrate area covered by MoS_2 nanocrystals determined by SEM is nearly identical to the fractional coverage of MoS_2 derived from the S_{LMM} AES signal. We interpret this result as confirmation that all S deposited on the substrate is incorporated into stoichiometric MoS_2.

These variations in nanocrystal size, nucleation density and total coverage are believed to be a result of the variation in substrate temperature along the substrate, which is plotted in Fig 3.12, or the changing distance from the MoO_3 source to points along the substrate. The decrease in MoS_2 coverage as distance from the substrate center increases is likely due to the variation in distance from the MoO_3 source, which is closest to the substrate center. The concentration of Mo in the Ar carrier gas may not become uniform during the time required for transport between the source and substrate at the 150 sccm flow rate for which the data of Fig. 3.11 was acquired. By standard growth kinetics argument, a decrease in material flux to a given area of the substrate would be expected to yield a lower density of larger features. As this is not what is observed, it is likely that the decrease in nanocrystal size away from sample center is related to variation of the substrate temperature. A lower surface temperature is expected to reduce the surface

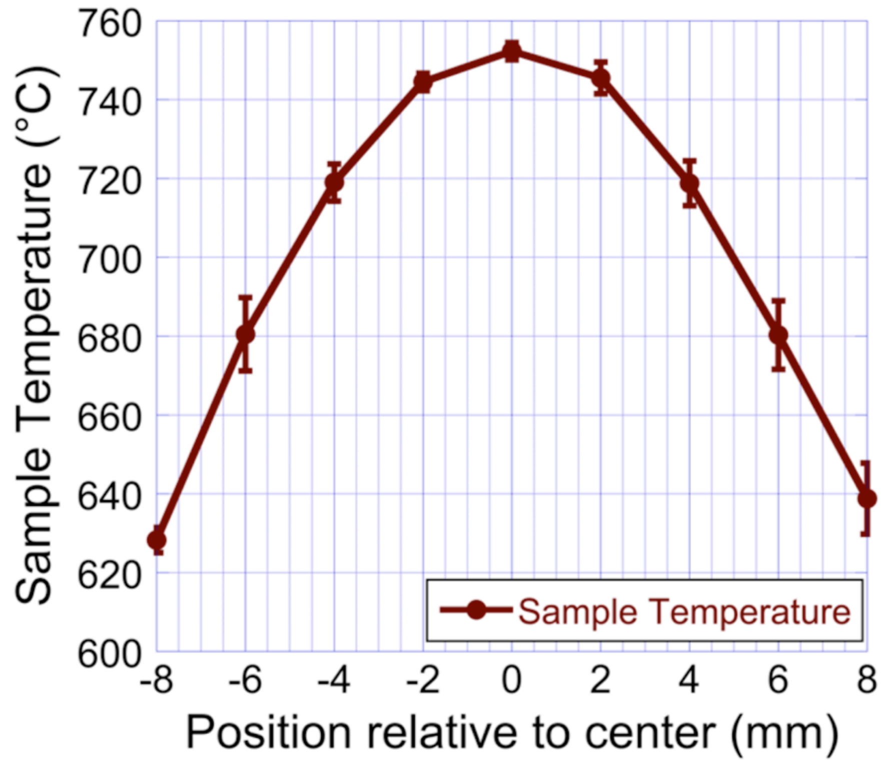

Figure 3.12: Variation of temperature along substrate. The IR pyrometer samples a ~ 3 mm diameter circular area. To improve the spatial resolution of the temperature measurement, a stainless-steel sheet with a 1 mm wide slit was inserted between the pyrometer and the substrate. The slit and pyrometer were translated relative to the sample in 2 mm increments [83].

diffusion rate of Mo adatoms, increasing the density of features with a lower average nanocrystal size. Fig 3.12 shows that moving from sample center to the coldest part of the sample, there is a 120 °C decrease in temperature. The combination of reduced flux and reduced surface diffusion could easily produce an 'average size' vs. 'position relative to center' curve similar to the one presented in 3.11(b).

3.3 Limitations and Motivation for Configuration Change

With this growth configuration and technique, we have demonstrated a novel method for the synthesis of single layer MoS_2 nanocrystals by co-depositing MoO_3 and S onto resistively heated SiO_2/Si substrates in a flowing Ar ambient. Though many groups have successfully grown MoS_2 using these source materials in tube furnace-based hot-wall CVD systems, the experimental configuration we designed and implemented allowed us independent control of the deposition parameters while minimizing gas-phase reactions. By individually optimizing deposition parameters, we identified growth conditions that yielded consistent run-to-run MoS_2 coverage and uniformity in film morphology over several square mm regions of the substrate. Using AES and SEM, we determined that while there is an excess of Mo in our films, all S detected on the substrate is incorporated into stoichiometric MoS_2.

While this was an significant first step toward understanding the growth mechanisms and the morphological consequences of varying growth parameters, it was apparent that more needed to be done to achieve the level of control we sought. While we clearly can deposit consistent amounts of Mo from run-to-run, we cannot consistently obtain similar feature size or areal density. This result suggests that the Mo surface diffusion rate varied between growths. Significant changes in growth kinetics could be

the result of a number of factors. However, the high volatility of S made us consider it the factor most likely to be causing run-to-run discrepancies in growth kinetics. An increase in the partial pressure of S during growth is suspected to slow the surface diffusion of Mo adatoms, by providing more opportunities for the Mo adatoms to form the heavier MoS_x. For this reason, a more stable and consistent method of delivering S to the growth surface was developed.

CHAPTER 4

SYNTHESIS OF MoS_2 USING MoO_3, MHC AND DES

In this chapter, we describe our use of molybdenum trioxide (MoO_3) and molybdenum hexacarbonyl, $Mo(CO)_6$, (MHC) as Mo sources and diethyl sulfide, $C_4H_{10}S$, (DES) as a S source to grow MoS_2 films. First, we explored the use of MoO_3 and DES. As this was found to irreversibly contaminate the alumina-coated W basket used to heat the MoO_3, we switched to the higher vapor pressure MHC as our source of Mo. Simultaneous with this switch, we began growing on sapphire (Al_2O_3), in place of the SiO_2/Si substrates used for the work in chapter 3. This change was made because of Al_2O_3's ability to withstand high growth temperatures and the ease with which clean, atomically flat surfaces are produced.

We begin this chapter describing the chamber modifications performed to add DES to the gas inlet line. This discussion includes an in depth description of our home-designed 'bubbler' system, and motivates our switch to MHC. The significant changes and custom parts needed to accommodate the switch to MHC are then outlined. We first detail the need to cool the precursors as well as the method used to accomplish this. Because of the large number of parts that needed simultaneous manipulation, it was necessary to automate the growth system, which is then outlined. Following this description, the methods used for cleaning and heating the Al_2O_3 substrates are described. Because many of the custom parts created in this stage were used throughout the remainder of the project and are referenced in chapters 5 and 6, this chapter focuses mostly on the experimental details of transitioning from the solid source (MoO_3 + S)

evaporation discussed in chapter 3 to the vapor delivery systems used to transport MHC + DES vapor to the substrate.

The results and discussion shows the MoS_2 films typical to those grown under this configuration with this combination of precursors. As will be discussed, the use of solid/liquid "slurry" cold-baths made repeatability challenging and obtaining information about growth trends difficult. Consequently, a discussion of how variation of growth parameters affect growth trends is reserved for chapter 5, where we have achieved run-to-run repeatability. We conclude this chapter with a brief summary and the motivation for further changes to our selection of precursors.

4.1 Experimental Methods

4.1.1 Chamber Configuration

It was necessary to modify the chamber for DES to be employed as a source of S. At room temperature (RT), DES is a clear liquid with a vapor pressure of 50 Torr [100]. These properties not only required modification to the growth chamber, but the development of a 'bubbler' system to deliver precursor vapors to the substrate. As this system was specially designed for our 2D materials projects, and because it was used throughout the remainder of the project, it warrants careful description. It is later employed for the delivery of molybdenum hexacarbonyl and tungsten hexacarbonyl in this dissertation, and was employed by Emmanuel Borcean for the delivery of ammonia borane in his work on 2D hexagonal-boron nitride.

4.1.1.1 'Bubbler' System for Delivery of Source Vapors

The delivery system we designed and employed is much like the bubbler systems commonly used in metal organic chemical vapor deposition (MOCVD). The bubblers

typically used in MOCVD are closed stainless steel (SS) containers that house a liquid precursor. Two tubes are used flow a carrier gas through the bubbler, usually ultra-high purity (UHP) Ar. One of these, the gas inlet tube, extends below the liquid level inside the bubbler and the other remains above it. In this way, the carrier gas is "bubbled" through the liquid precursor. The other tube, the gas outlet, is above the liquid level. The gas bubbled through the precursor is assumed to be saturated with the vapor of the precursor before being transported to the growth chamber.

For the delivery of DES into our chamber, we employed a similar method. A closed end Pyrex tube with a ceramic-to-metal sealed Kwik-Flange (KF) port was acquired from MDC [101]. To minimize the time spent reloading the DES bubbler, we eventually had the on-campus glass shop increase the diameter of the Pyrex tube from 1.5" to 4.0". To seal the flange, we designed a custom KF flange, which was fabricated by the on-campus machine shop. Like the bubbler system described above, the flange has two ¼" diameter SS tubes which pass through the flange and into the Pyrex tube. Rather than actually bubble through a liquid precursor, our system relies on the vapor pressure of our source materials to saturate the Ar as it is flowed through the tube. Because of the similarities between this method and the MOCVD bubbler method, we refer to the Pyrex tube as a 'bubbler' throughout.

Fig. 4.1 is a schematic of the bubbler system with the SS tubing involved. On the air-side of the flange, the ¼" SS tubes terminate in metal-sealed VCR fittings. Stainless steel VCR gaskets were used in place of the more commonly used Cu gaskets because of the deterioration of Cu in a sulfurous environment, as described in chapter 3. These VCR ends connect to a configuration of valves that allow for two 'states' of the delivery

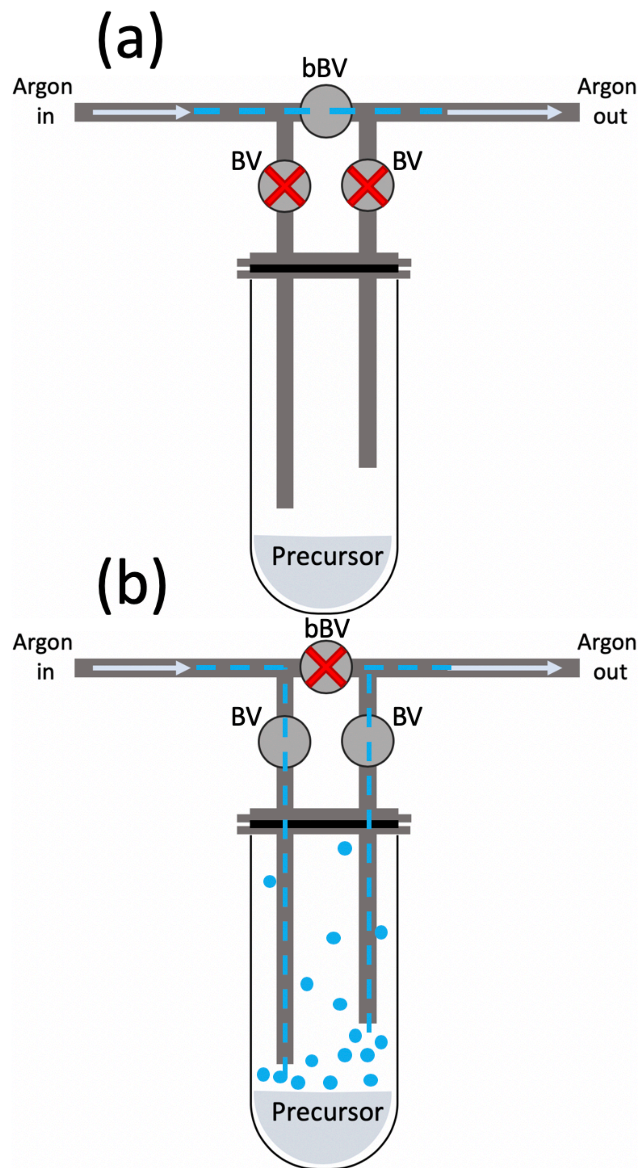

Figure 4.1: A schematic of the bubbler system used to deliver precursor vapor to the substrate. Two states of this system were used: (a) Ar is flowed through the bubbler bypass valve (bBV) to allow for pressure equilibration in the main chamber at growth flows, (b) The bBV is closed and the two bubbler valves (BV) are open. This flows the Ar through the bubbler, saturating the Ar with the precursor vapor for delivery to the substrate.

system: (1) Ar is flowed in into the chamber via the bubbler bypass valve (bBV) and (2) Ar is flowed through the first bubbler valve (BV), into the bubbler, out the second BV and into the chamber. State (1), shown in Fig. 4.1(a), is used to equilibrate the pressure in the chamber, using the downstream pressure control valve (PCV) discussed in chapter 3. State (2), shown in Fig. 4.1(b) is used for delivery of the precursor material to the chamber, i.e. growth. This configuration was tested without precursor material, flowing Ar, and it was found that switching between these states (1) and (2) caused no change in chamber pressure.

4.1.1.2 Implementation of the 'Bubbler' System for DES

The bubbler outlined above was added to the growth chamber using three manually controlled shutoff valves. 98.0 % DES (Sigma-Aldrich) was loaded into the Pyrex 'bubbler'. Because of the high flammability and skin and eye irritation properties of DES vapor, this was done in a fume hood. The bubbler was then mounted to the chamber. A schematic of this addition is given in Fig. 4.2(a). Fig. 4.2(b) is an image of the realization of this scheme. A dashed line is superimposed on the image to aid the eye in following the gas pathways. The pumping configuration on the downstream end of the gas flow is detailed in chapter 3.

Experiments conducted using this reactor configuration were few because the DES was found to irreversibly contaminate the alumina-coated W basket that contained the MoO_3, which was located downstream. To achieve run-to-run repeatability, the contaminated baskets needed to be replaced after each growth, with a newly bonded S-type thermocouple. The time and cost needed to maintain this precluded further pursuit of this method. The few results from these experiments were inconclusive and none are

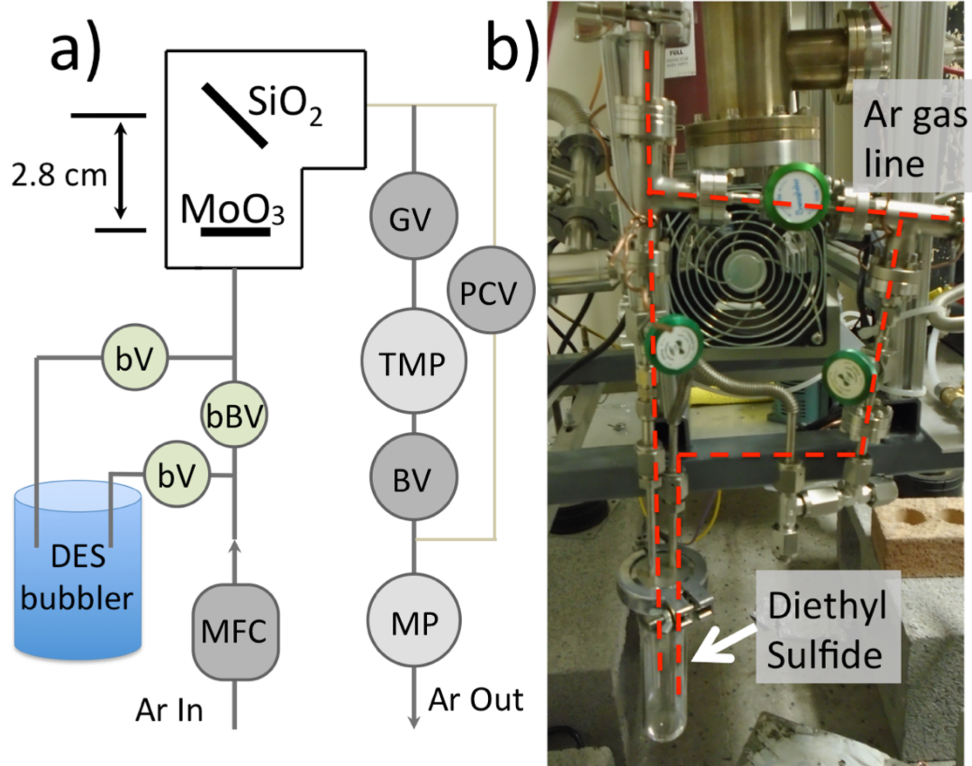

Figure 4.2: (a) A schematic of the growth chamber used for the MoO_3 and diethyl sulfide (DES) sourced growths. This is similar in many respects to the schematic in Fig 3.1, but with the replacement of the S source basket with a DES bubbler, shown in Fig 4.1. Prior to growth, the Ar pressure is stabilized flowing Ar through the bubbler bypass valve (bBV). During growth, bBV is closed and the two bubbler valves (bVs) are opened to force the Ar flow through the bubbler. (b) Image of the Ar/DES gas line. A dashed red line is given for aid in distinguishing the gas lines from the background hardware.

presented herein. However, it verified the feasibility of DES as a S source, and proved the viability of our bubbler system as a means to transport precursor vapor to the substrate. We therefore modified the chamber to include a second bubbler that would house a high vapor-pressure Mo precursor that could be protected from exposure to the DES.

4.1.1.3 Addition of MHC

Molybdenum hexacarbonyl (MHC), $Mo(CO)_6$, was selected as a new source of Mo. Its low vapor pressure, relative to that of DES (0.118 Torr at room temperature [102-103] compared to 50 Torr at room temperature for DES [100]), concurrent experiments within the group using the similar hexacarbonyl, $W(CO)_6$, as a precursor and already published literature demonstrating MHC as a viable source of Mo for the synthesis of MoS_2 [39], made it a viable candidate. The bubbler system described in section 4.1.1.1 was employed to transport MHC vapor. 98% MHC (Strem Chemicals) was carefully loaded in a separate bubbler mounted to a separate bubbler system with an independent mass flow controller (MFC), allowing control over the flow through the MHC bubbler. At room temperature, MHC is a solid, white powder. It is acutely toxic and fatal, and was therefore handled with suitable care. The vapor pressure curves for both DES and MHC are given in Fig. 4.3.

An additional Ar line was added to allow a flow of Ar directly into the chamber concurrent with Ar flowing through the DES and MHC bubblers. This line was controlled by a separate MFC. Thus, Ar was allowed to flow into the chamber via three separate lines, each with its own MFCs: one leading directly to the chamber, one to the DES bubbler system and one to the MHC bubbler system. In this way, we were able to control the Ar flow through the DES bubbler, through the MHC bubbler, and dilute the mixture

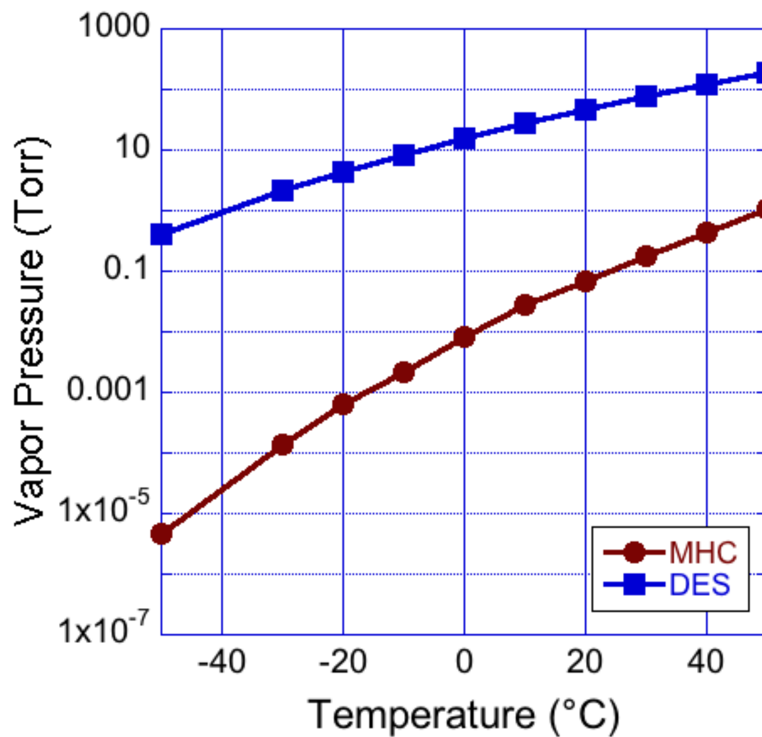

Figure 4.3: Plots vapor pressure as a function of temperature for the two precursor materials used in this study, molybdenum hexacarbonyl (MHC) and diethyl sulfide (DES). The vertical axis is a logarithmic scale [100,102-103].

with a controlled flow of Ar. Common MOCVD practice is provide a flow of H_2 as a necessary means of removing spurious C from the growth surface and its surroundings. To accomplish this, an additional gas inlet line was added allowing UHP (99.999%) H_2 to be flowed into the reaction chamber simultaneous with the three Ar flows. The flow of H_2 was regulated by an additional MFC. A schematic of this reactor configuration is given in Fig. 4.4. The bubblers were mounted approximately 1 meter off the ground to allow the various cooling systems employed, discussed below, to be easily added and removed. Various full-scale ranges of MFCs were used in the exploration of flow dependence. It is noteworthy that we decided to place the MFCs upstream from the sources to keep from contaminating the MFCs by the unintentional deposition of source material.

4.1.1.4 Preparation and Cooling of Precursors

After loading the precursors, a freeze-pump-thaw method of degassing the materials was conducted. Though we used this method as a means to purify all our precursors and purge the bubblers of contamination, it is most effective with liquids and the freeze-pump-thaw process for the DES is outlined here as an example. This process was done without the flow of any gasses. First, the bubbler, with the precursor, was submerged in liquid nitrogen (LN_2), -196 °C, until the entirety of the DES was frozen in the bottom of the Pyrex tube. Using the turbo molecular pump (TMP), the frozen DES was pumped for approximately 1 hr. Because of sulfur's propensity for contamination, we did not have an ion gauge to monitor the pressure. Instead, the current load on the TMP, which is related to pressure, was used to monitor the 'pressure'. When the current load on the TMP reached the value it achieves at vacuum, under no additional gas load, the BVs were closed to isolate the bubbler from the chamber. At this point the DES was thawed to

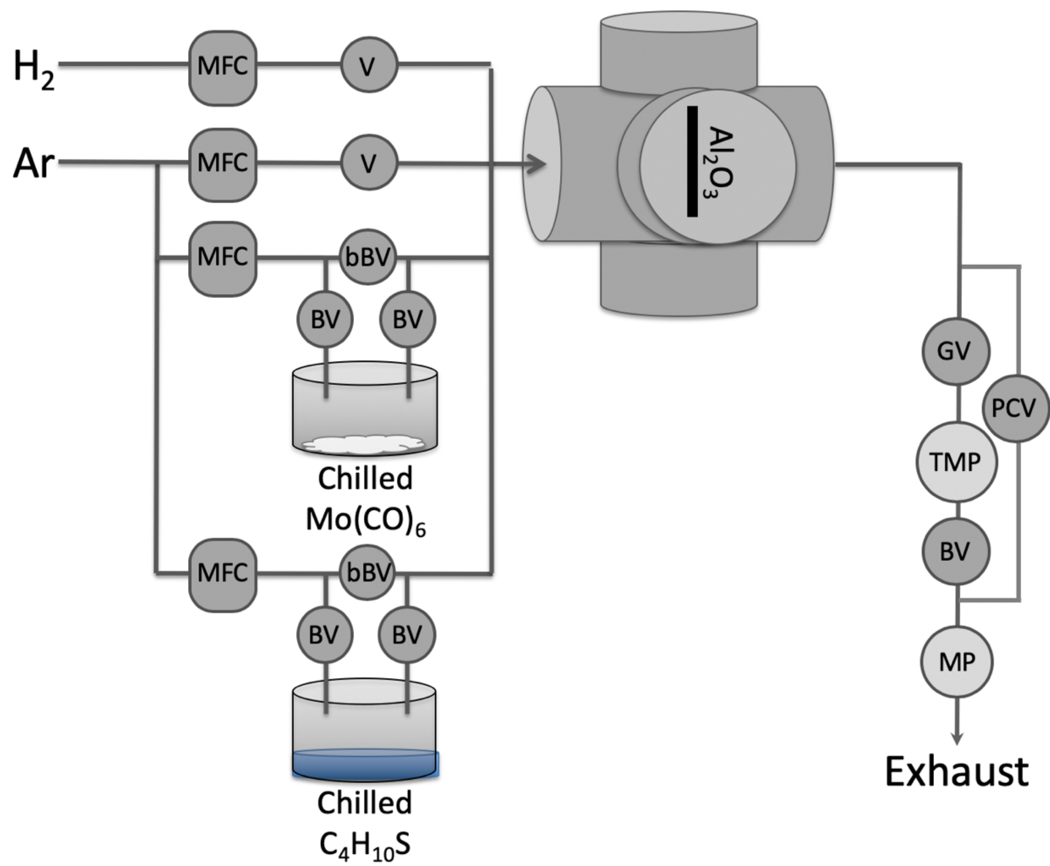

Figure 4.4: A schematic of the growth chamber used for the MHC, $Mo(CO)_6$, and DES, $C_4H_{10}S$, sourced growths. This is similar in many respects to the schematic in Fig. 4.2, but with the addition of a second vapor deliver system for the MHC. This configuration also includes the addition of independently controlled ultra-high purity H_2 and Ar gas lines. With this configuration, we were able to equilibrate the pressure in the chamber under the four gas flows without exposing the sample to any source material.

room temperature (RT). The difference in evaporation points between the liquid DES and gasses trapped in the liquid causes a bubbling of the source material as the trapped gases phase separate from the thawing liquid. Once the DES was completely thawed to RT, it was once again frozen in LN_2 and the cycle repeated. When no bubbling occurs in the 'thaw' step and the maximum current load on the TMP is unchanged when it is exposed to the frozen DES, the material is degassed and ready for use. This usually took 3 full freeze-pump-thaw cycles to achieve.

As stated above, the RT vapor pressures of MHC and DES are 0.118 Torr and 50 Torr, respectively. These vapor pressures are too high for the slow, controlled growth process we sought. For instance, it was found that growing with the MHC at room temperature, under growth conditions, Mo was deposited on the substrate at a rate of 0.5 monolayers / min. Therefore, to suppress the vapor pressures of the precursors, the bubblers were submerged in cold baths during growth. This was accomplished using independent dry-ice cooled solution baths, maintained as liquid/solid "slurries" at the freezing point temperatures of the solutions. Table 4.1 lists the solutions used in this study and will be specified where they apply. The cooling solution most commonly employed for the MHC was a 6:5 mixture of calcium chloride hexahydrate ($CaCl_2 \cdot 6(H_2O)$) and water, yielding temperatures between -40 °C and -43 °C. The DES was most commonly cooled using a 1:3 sodium chloride (NaCl) in water mixture, to a temperature of -21 °C. Solutions were held in beakers heavily insulated with 5 cm - 8 cm of polyurethane foam rubber and continuously stirred throughout the growth. To maintain the freezing point of the bath, dry-ice was continuously added to the mixture in small chunks, < 1 cm^3 in volume. This repetitive and highly tedious task over long growth

times led to our development of a thermoelectric-cooled liquid bath chiller, discussed in detail in appendix A, and motivated the eventual switch to tungsten hexacarbonyl as a transition metal source (see chapter 5).

Temperature (° C)	Solution used	Ratio
-14	MeOH : H_2O	1 : 6
-21	NaCl : H_2O	1 : 3
-24	MeOH : H_2O	3 : 11
-34	$CaCl_2 \cdot 6(H_2O)$: H_2O	1 : 1
-40	$CaCl_2 \cdot 6(H_2O)$: H_2O	6 : 5
-47	MeOH : H_2O	1 : 1
-50	$CaCl_2 \cdot 6(H_2O)$: H_2O	7 : 5

Table 4.1: Shows the cold-bath "slurry" solutions used to cool the precursors. All mixtures were cooled by the addition of dry-ice throughout the growth.

4.1.1.5 Automation of the Growth Process

Looking at Fig. 4.4, there are eight valves and four MFCs that require simultaneous manipulation. Each MFC requires a +15 V and -15 V power supply, a 0 V – 5 V control voltage, and each transmits a 0 V - 5 V 'sense' voltage, an internal measurement of the actual flow passing through the MFC. Because of the large number of valves and MFC operations that required simultaneous reading and manipulation, it was necessary to automate the growth process. A National Instruments USB interface, NI USB-6001 [104], was used to handle the multitasking. The NI USB-6001 allows control

over eight digital I/O outputs, two 0 V - 10 V analog outputs and eight 0 V -10 V analog inputs.

The digital I/O outputs were used to control all eight valves upstream of the growth chamber. These valves were all SS pneumatic valves, opened by application of 90 psi of N_2. To utilize the digital I/O outputs from the NI USB interface, eight solenoid valves were used to regulate the pressure to the eight pneumatic valves. As these solenoid valves required 120 V AC to activate, and the digital I/O output of the NI USB interface was ~ 4 mA DC, we designed and implemented a rack-mounted box housing an array of solid state relays. In this way the eight 4 mA DC outputs were able to independently activate eight separate solid state relays, each of which independently opened one of the eight solenoid valves, in turn opening a pneumatic valve. This box is seen in Fig. 4.5 as the black box in the bottom of the image.

Four of the analog inputs on the NI USB interface were used to directly read the 'sense' voltage from each MFC. The analog outputs were used to control the MFCs. To control four MFCs with two analog outputs required a little engineering. Two voltage dividers, each with a 2 kΩ potentiometer, were used to provide a control voltage to the four MFCs. This allowed one MFC to be controlled at the full analog output (0 V - 10 V) and the other to be operated at a fraction of the full analog output (controllable with the potentiometer).

Initial experimentation with this method was done with breadboards and alligator clips. To protect the circuitry from the user (and vice versa), we designed and created an instrument box to house the MFC power supplies, the reading circuitry and control the voltage dividers. Fig 4.5 is a photograph of the front panel of this box. It was designed in

anticipation of adding additional source lines to the chamber, and was thus designed to allow for four separate voltage divider circuits to control a possible total of eight MFCs. The top switch activates a given MFC. The top row of red banana jack plugs allow the sense to be measured at any time using a volt meter, relative to ground, the black banana jack plug in the bottom right of the front panel. The knobs below the red plugs are the potentiometers, whose resistance can be measured between growths by the red plugs directly below. Two salvaged computer fans were secured inside the box and a series of holes drilled to allow adequate air flow to the power supplies.

To simultaneously control all the functions of the NI USB interface, a custom LabVIEW program was written. Various iterations of this program were used to accommodate the many changes made to the chamber configuration and the growth process. The various iterations of this control program are presented in the chapters where they are employed. It is worth noting that commercially available options were not available to accommodate the very specific needs of this stage of the project and required the careful in-house customization described above.

4.1.2 Sample Preparation and Heating

With the switch to MHC + DES growth of MoS_2, sapphire, Al_2O_3, was chosen to replace SiO_2/Si as the growth substrate. Sapphire was selected because of its atomically flat surface after annealing and its robustness at high temperatures. MoS_2 films grown under this configuration were grown atop 4 mm x 20 mm strips cleaved from single-side polished c-plane sapphire wafers off 0.2° toward the m-plane, obtained from Precision Micro Optics. Sample cleaning was performed by sonication for 10 min in acetone,

Figure 4.5: Photograph of the two instrument boxes designed and created for the automation of the growth process. The top box is the MFC control box, which directs all input and output communication between the NI USB600-1 interface and the MFCs. It also houses the power supplies and voltage dividers required by the MFCs. The row of switches at the top are in place to activate/deactivate each MFC. The red banana plugs below the switches allow the sense to be measured at any time. The four knobs below these control the division of the voltage and the final row of red plugs allow the resistance of the potentiometer to be measured. The black box underneath houses the array of solid state relays for control of the solenoid valves, and consequently control of the pneumatic valves.

followed by 10 min sonication in isopropyl alcohol. After sonication, the samples were loaded in an open-air quartz-tube furnace held at 1,000 °C for 1 hr. The 1 hr anneal not only desorbs contamination not removed by solvent sonication, but also causes a change in the surface morphology of the sapphire [105-110]. The "out-of-box" surface, Fig. 4.6(a), is restructured by the annealing process, forming atomically flat terraces 3 Å high with a terrace width of ~ 70 nm, which matches the 0.2° cut specification of the wafers. The surface after annealing is shown in the atomic force microscope (AFM) height mode image in Fig. 4.6(b). Terrace edges are visible as peaks and troughs in the line-scan height profile, Fig. 4.6(c).

Interestingly, this cleaning method occasionally yielded an unintended large-scale patterning of the sapphire substrate. This patterning exhibits semi-triangular regions with a long, straight edge (along the steps of the Al_2O_3), and one lenticular rounded edge. This patterning is visible in SEM, Fig. 4.7(a), as dark contrasted semi-triangular regions. Fig. 4.7(b) is a height mode AFM image of the flat elongated edge of one of these 'triangles' and (d) is a line-scan height profile along the white line in (b). As shown by AFM, the flat elongated edges of the triangles are 3 - 4 step heights tall. Fig 4.7(c) is a height mode AFM image of the interior of the triangle. The triangular region is filled with irregularly edged terraces, which restore to the regular terrace edges immediately outside the feature. Terrace roughness inside the triangular region is identical to the terrace roughness outside the region.

Many experiments were done to determine the cause of and eliminate this effect. Different quartz tube geometries were used, different gasses were flowed through the furnace during the anneal, different anneal times were used, as were different annealing

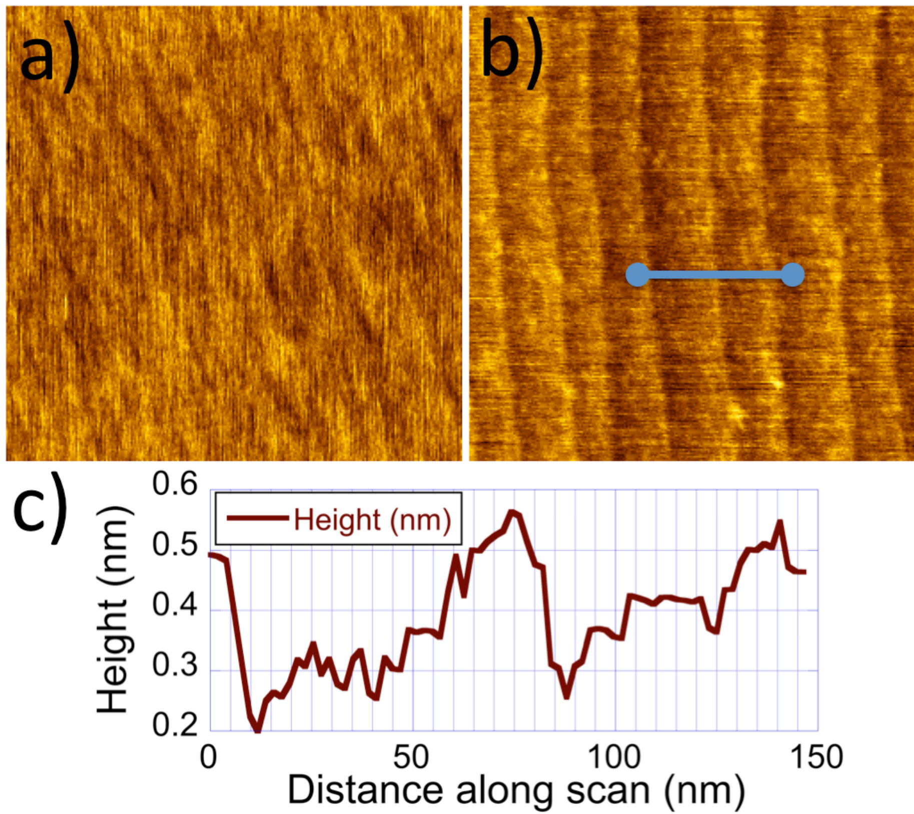

Figure 4.6: 500 nm x 500 nm height mode AFM images of a) "out-of-box" polished Al_2O_3 and b) the same Al_2O_3 sample after 1 hr annealing in air. The height profile over the blue line indicated in (b) is given in (c). Note the typical step height of 3 Å high, with a terrace width of ~ 70 nm, matching the 0.2° cut specification of the wafer.

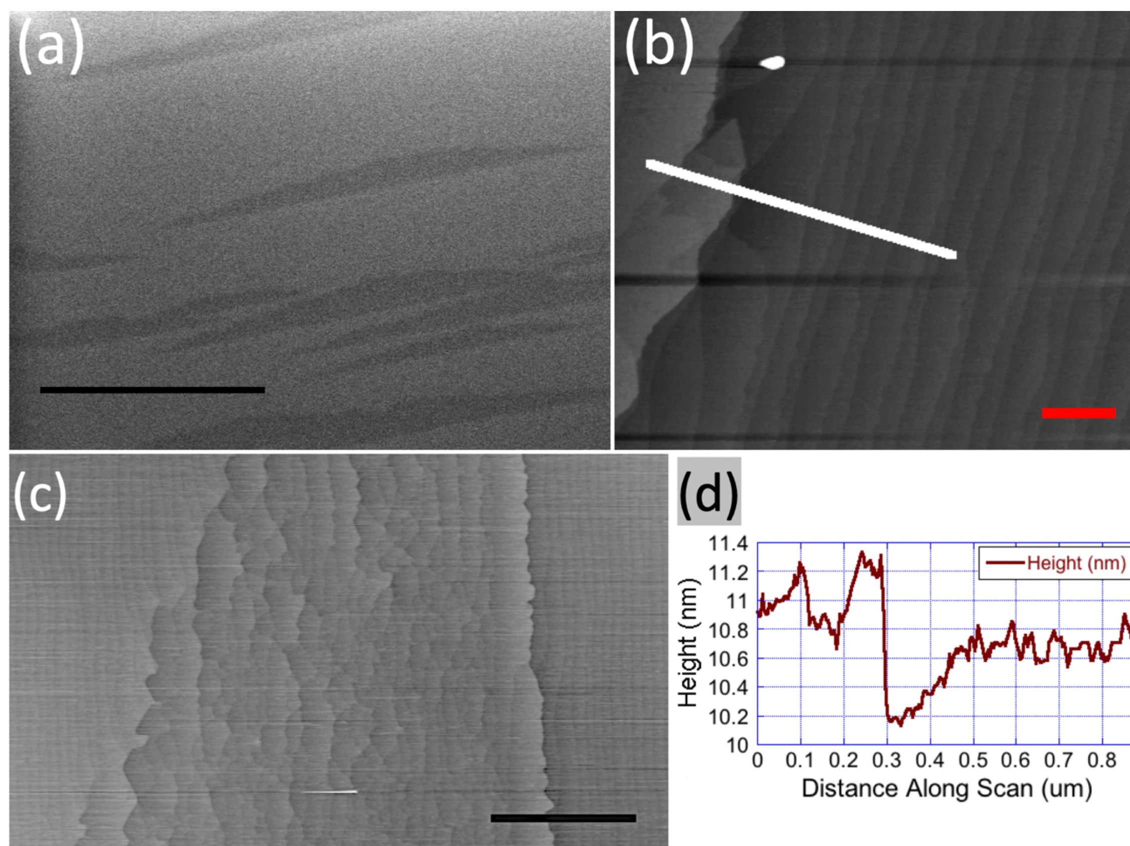

Figure 4.7: (a) SEM image of semi-triangular patterning occasionally seen after annealing Al_2O_3 at 1000 °C, in air, for 1 hr. The light grey areas are the "clean" sapphire expected from the cleaning process (see Fig. 4.6(b)). The black scalebar in (a) is 50 µm. (b) height mode AFM image of the long, flat edge of one of the dark triangular regions in (a). The red scalebar in (b) is 200 nm. The white line indicates the line-scan from which data is given in (d). (c) Height mode AFM image of the interior area of the triangular features. Scalebar in (c) is 1 µm. (d) shows a plot of height along the scan. It shows a 3-4 step heights drop at 0.3 µm before returning to the expected surface terracing outside the 'triangle'.

temperatures. The effect persisted. Only one instance of this phenomenon was found in the literature [111]. Contacting the authors of the paper, we learned that they too were unable to eliminate the effect. Though we were unable to pinpoint the cause of this patterning, we were able to mitigate it by purchasing the highest affordably available grade of sapphire wafers (> 99.996%). Use of the higher grade sapphire resulted in fewer annealed samples exhibiting the 'triangles' and lowered the density of the triangles from ~ 2.9×10^5 cm^{-2} to 8.0×10^4 cm^{-2}, yielding average distances between triangles orders of magnitude larger than the typical distance between our MoS_2 nanocrystals (~40 μm compared to ~100 nm), see Fig. 4.8(c). SEM images in Fig. 4.8(a) and (b) show the difference between a "bad" post-anneal substrate using the lower grade Al_2O_3, (a) and a "bad" post-anneal substrate using the higher grade, (b). A "good" post-anneal substrate was free of the semi-triangular defects. Fig. 4.8(c) is given to show that the triangles do not affect the surrounding MoS_2 feature size and density.

Since sapphire is an insulator, substrates could not be resistively heated by passing a DC current through them, as was described in section 3.1 to heat SiO_2/Si. Heating the sapphire required some ingenuity, which was explored throughout the remainder of the project. To heat the sapphire, single-side polished Si wafers were cleaved into 4 mm x 20 mm strips. These strips were placed against the sapphire strips, and both were clamped to the Ta electrodes on the sample holder as shown in Fig. 4.9(a). Since the bandgap of sapphire (9.1 eV) is much larger than the infrared (IR) energies used by our IR pyrometer (IR energy range = 1.24 eV - 1.7 eV), sapphire is transparent to the pyrometer.

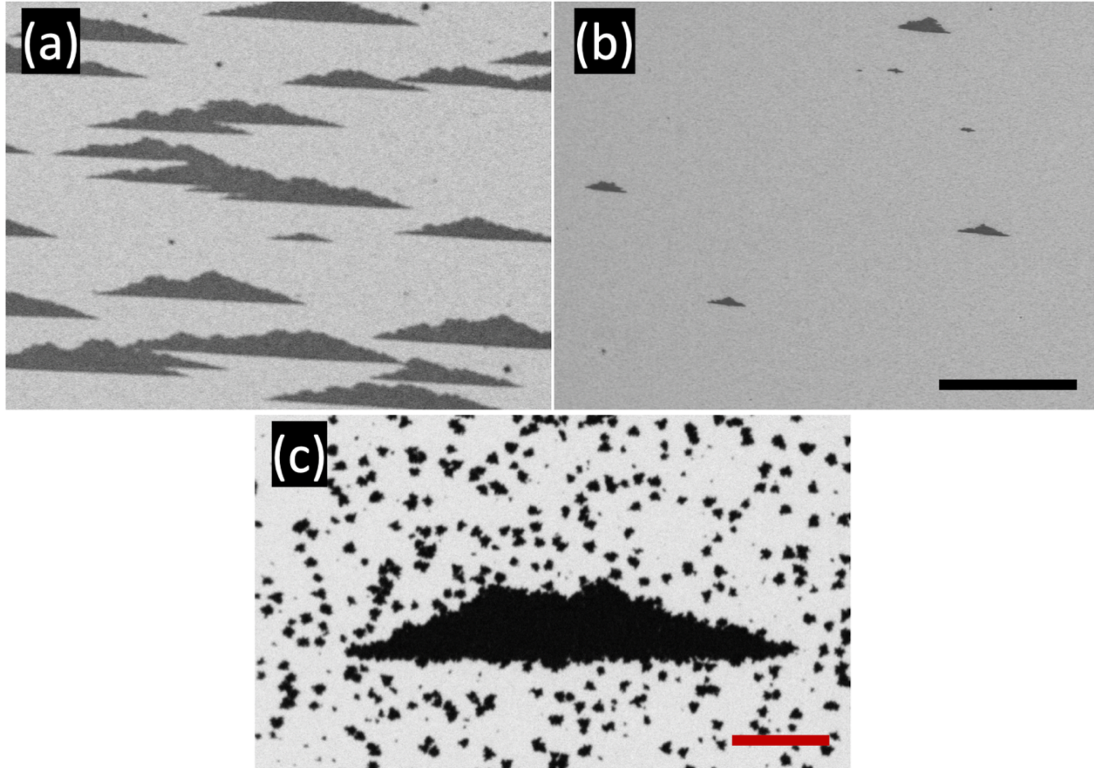

Figure 4.8: SEM images of MoS_2 grown on Al_2O_3 substrates with different densities of semi-triangular regions. The darker MoS_2 features selectively decorate the semi-triangular defects. (a) Represents 'bad' patterning, meaning a high density of large semi-triangular regions. (b) Representative of a 'good' substrate, meaning a low density of smaller semi-triangular regions. This image is from after changing to the high purity Al_2O_3 wafers. The black scalebar in (b) is 25 μm and applies to (a) and (b). (c) Shows the effect the semi-triangular region has on the MoS_2 growth. Feature size and density up to directly adjacent to the semi-triangular region is the same as in defect-free regions. The red scalebar in (c) is 2.0 μm.

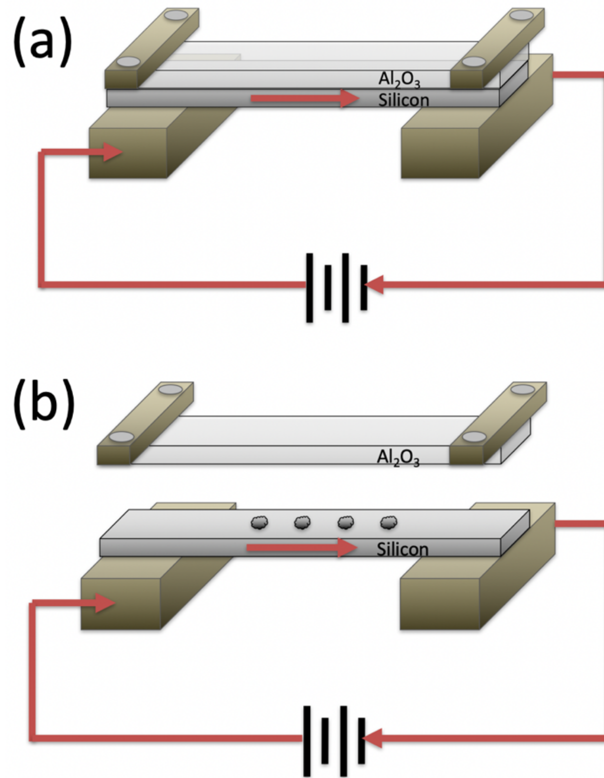

Figure 4.9: (a) Schematic of the method used for Al_2O_3 heating. A DC current is passed through a Si strip causing the Si temperature to rise, via resistive heating. By a combination of thermal and radiative heating, the hot Si strip against the Al_2O_3, heats the Al_2O_3. (b) Shows the 'Sn bonding' method used to increase the thermal conductivity between the Si and Al_2O_3, which significantly improved temperature agreement between the two.

Calibration of the sapphire temperature vs. Si temperature was performed using the IR pyrometer, measuring the Si temperature, and two K-type thermocouples (TC), one spring-loaded against the sapphire and the other spring-loaded against the Si. In this way, we were able to obtain $T_{Silicon,pyrometer}$, $T_{Silicon,TC}$, and $T_{Sapphire,TC}$. By the relationship between these values, $T_{Silicon,TC}$ - $T_{Sapphire,TC}$ as a function of $T_{Silicon,pyrometer}$, we were able to calibrate the temperature of the sapphire surface against the pyrometer reading. Results from this calibration are given in Fig. 4.10. The calibration was performed under pressure and flow conditions typical to a growth.

A marked improvement in the agreement between the sapphire and Si temperatures was achieved using 'indium bonding' between the layers. This method is commonly used in molecular beam epitaxy of III-V semiconductors to bond GaAs to Mo heater blocks. To apply this to our needs, four small (sub-millimeter diameter) dots of Sn were cut from a thin-rolled 99.999% Sn shot and placed along the length of the unpolished side of the Si strip. Then, the cleaned sapphire strip was mounted on top. The stack was then clamped to the Ta electrodes on the sample holder, as shown in Fig. 4.9(b). Indium was initially used but was found to migrate to the growth surface under growth conditions. Switching to Sn eliminated this effect. Consequently, we will refer to this thermal bonding with Sn as 'Sn bonding'.

4.1.3 Growth Preparation, Parameters and Procedure

Early in the experimentation, a sacrificial Si strip was used to thermally clean the sample holder and surroundings of spurious material, as described in section 3.3,. However, we found that, for these sources, this between-growth thermal cleaning was unnecessary for obtaining run-to-run repeatability, and was abandoned. The Sn bonded

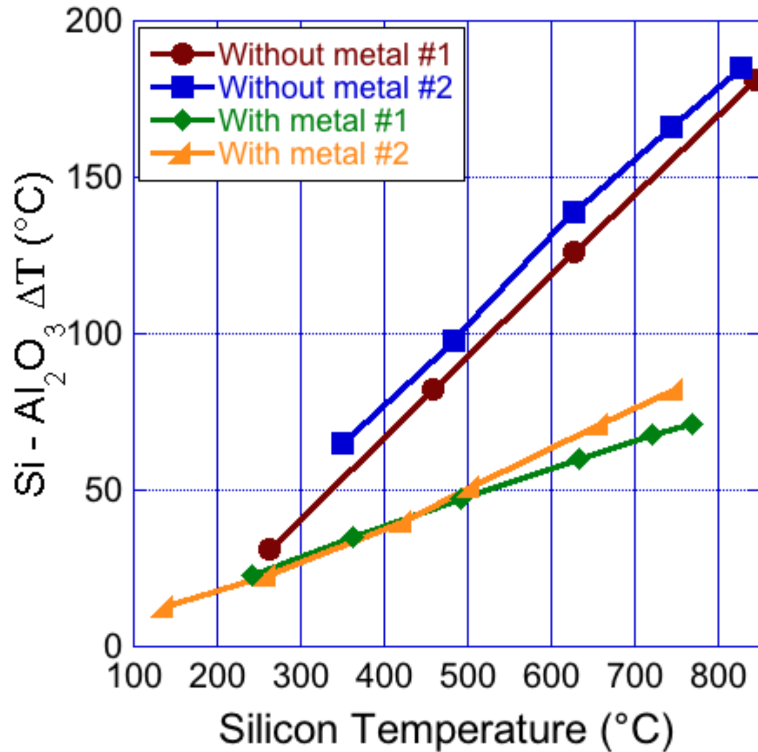

Figure 4.10: Plots the difference in temperature between the Si heating strip and the Al_2O_3 growth surface as measured by the thermocouples, $T_{Silicon,TC}$ - $T_{Sapphire,TC}$, as a function of the Silicon temperature measured by the pyrometer, $T_{Silicon,pyrometer}$. The "with metal" curves were obtained with the Al_2O_3 Sn bonded to the Si as described above (see Fig. 4.9(b)). "Without metal" was done without Sn bonding. The numbers, #1 and #2, in the legend indicate measurements using separate setups (i.e., new substrates and thermocouples) to check the repeatability of these measurements. The data shows a dramatic improvement the agreement between the Al_2O_3 and Si when Sn bonding is used, from a ΔT of ~ 150 °C without Sn bonding, to 60 °C with Sn bonding, at a Silicon temperature of 600 °C.

Al_2O_3 sample was loaded into the chamber, which was pumped for 30 min to achieve a pressure in the 10^{-6} Torr range. During this time, the dry-iced-cooled solution baths were prepared. The TMP was then isolated from the main chamber and vented with N_2, before flowing UHP Ar (99.999%) and H_2 (99.999%) through the chamber and into the mechanical pump. The LabVIEW control program was used to initiate the flow. To accomplish this task, the button labeled "flow" on the LabVIEW graphical interface was triggered. This instructed the NIUSB interface to supply a control voltage to all four MFCs and send the appropriate I/O signals to open the valves labeled "V" and "bBV" in Fig. 4.4. At this point, the program also began reading and displaying, real-time, the MFC sense values. These values were concurrently written into an Excel file.

Pressure was again controlled using the PCV, which was heated to > 170°C, as described in section 3.1. Once the pressure was observed to be stable over timeframes relevant to the growth, the capacitance manometer was isolated from the growth chamber. At this point, the source bubblers were submerged in their respective temperature baths. To prevent the possibility of small pressure differences between the bubbler and the chamber, the downstream bubbler valve was open for 5 sec to allow a pressure equilibration between the two. This task was also performed by the LabVIEW control program. The buttons labeled "MHC eq" and "DES eq" on the LabVIEW graphical interface triggered the opening of the downstream BV valves in Fig. 4.4. This was done first for the MHC bubbler, then, after allowing 10 min for the source vapors to be flushed by the flowing Ar + H_2, it was done for the DES. After waiting another 10 min for the DES to be flushed, the sample temperature was manually increased to the desired growth temperature.

After pressure equilibration, growth was initiated in the LabVIEW program by triggering the "growth" button to 'active'. This action simultaneously closed the two bBVs and opened the four BVs, forcing Ar through the MHC and DES bubblers, and exposing the hot growth surface to the flow of source gasses. This state was maintained for the duration of the growth. After the desired exposure time, the "growth" button was again triggered to return to the "flow" state, simultaneously opening the bBVs and closing the BVs. After this change in valve states, samples were annealed under Ar and H_2 for 5 min - 30 min to prevent source material still in transit from reaching a "cold" substrate, which would alter adatom diffusion and final growth morphology. It can be expected that precursors arriving at a cooler substrate would have a shorter diffusion distance than those arriving at the "hot" substrate, yielding a bimodal distribution of features grown on the hot and cold substrates. This effect was observed in our group by Emmanuel Borcean growing hexagonal boron nitride atop liquid and solid Cu substrates. After this annealing time, the sample was cooled to room temperature. Flow and pressure were maintained under these valve conditions for 20 min to allow rapid cooling of the sample and to purge the chamber of excess source vapors. The flow was then terminated in the LabVIEW control program before venting the growth chamber and removing the sample for analysis.

MoS_2 growths were investigated with source bubbler temperatures in the range of -50 °C to 25 °C and -36 °C to 25 °C were explored for the MHC and DES respectively. Substrate temperatures from 450 °C to 790 °C were explored. Growth times from 10 min to 300 min were performed, and the pressured varied from 33 Torr to 300 Torr. The main Ar flow was varied from 138.6 sccm to 680 sccm.

4.2 Results and Discussion

Though many MoS_2 films were synthesized using MHC and DES, the necessary repeatability was unattainable (discussed below). Because of this, it was difficult to establish growth trends. Fig 4.11 shows SEM and AFM of MoS_2 films characteristic of those produced using MHC and DES. In the SEM images, (a) and (c), MoS_2 features appear as dark spots contrasted against the much lighter substrate. In the height-mode AFM images, (b) and (d), the MoS_2 features appear as the light grey to white features contrasted against the much darker substrate. Note that the Al_2O_3 steps are visible in the background of the AFM images as dark lines running from the top to the bottom of the image. SEM images are given at a relatively low magnification to give a sense of feature density, where AFM is given at a higher magnification to show feature morphology. From (b) and (d), we see that the MoS_2 crystals are semi-triangular, with irregular, sometimes jagged, edges. Feature height was only observed in multiples of the height measured for single-layer MoS_2 (see Fig. 3.5), i.e. N x 0.7 nm, where N is an integer indicating the number of S-Mo-S layers.

The two samples shown in Fig. 4.11 were grown for 2 hr with a 15 min anneal, as described above. All parameters were kept the same, with the exception of the substrate temperature, which was varied from 650 °C, (a) and (c), to 720 °C, (b) and (d). As evidenced by Fig. 4.11, increasing the substrate temperature decreases the nucleation density from 3.6×10^9 cm^{-2} to 6.25×10^7 cm^{-2}, and increases the average feature size, the square root of the area of the substrate covered by the feature, from 40 nm to 70 nm. This correlation between feature size and nucleation density and substrate temperature was repeated and verified to be independent of the source materials used (see chapters 5 and

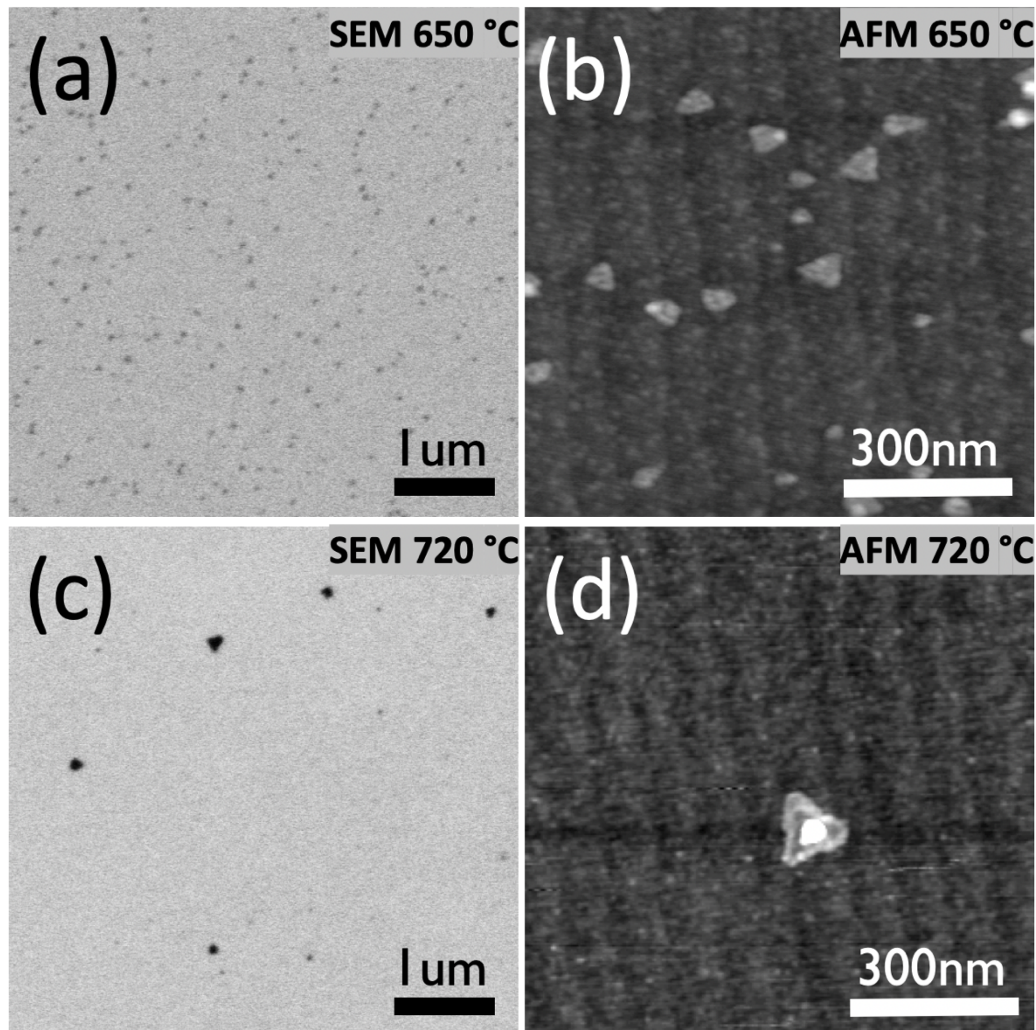

Figure 4.11: (a) and (c) SEM images, (b) and (d) height mode AFM images of MoS_2 films grown on Al_2O_3 typical of those grown using molybdenum hexacarbonyl (MHC) and diethyl sulfide (DES). (a) and (b) are of a sample grown at a substrate temperature of 650 °C, while (c) and (d) are of a sample grown at 720 °C. This shows a dramatic reduction in density of features from 650 °C to 720 °C. Where the features in (b) are 0.7 nm tall, the height of single-layer MoS_2, the white at the center of the feature in (d) is 7 nm tall. The Al_2O_3 steps are visible in (b) and (d) as dark vertical lines running from the top to the bottom of the image.

6) and implies the importance of surface diffusion in the nucleation and growth process involved in TMD growth.

Also of note in Fig. 4.11 is the increase in feature height as the substrate temperature is increased. Features grown at 650 °C, Fig. 4.11(b), are single layer, with a height of 0.7 nm. The feature in Fig. 4.11(d) is typical of the others in Fig. 4.11(c). The light grey base of the feature is single-layer and the white on top is 7 nm tall, corresponding to ten S-Mo-S layers. This indicates that though nucleation density decreases at higher substrate temperatures, the excess material goes into vertical growth of 3D features. RBS analysis of these samples showed a presence of ~0.06 ML of Mo on the substrate, with a corresponding S signal too low to quantify against the background, as discussed in chapter 2.

The AES analysis of our MoS_2 films grown using MoO_3 and S, section 3.2, supports an assumption we make throughout: that because of the low sublimation point of S, S atoms cannot stick to a hot substrate without a Mo atom present for it to bond to. Models of nucleation and growth state that an atom that sticks to a surface will diffuse across the surface in a random walk some distance determined by the energy available to it (i.e. surface temperature), and the availability of low energy sites (i.e. a S atom or another Mo atom) [112-116]. This implies that the surface diffusion effect on nucleation and growth shown in Fig. 4.11 must be dominated by the surface diffusion of Mo atoms. The effect of S in this process is debated in the literature [39,117-120].

If TMD growth follows the model of nucleation and growth referenced above, it stands to reason that other effects predicted by these models could be observed. One such

effect is that of material flux. As stated above, the distance an atom can diffuse across the surface is also determined by the availability of low energy sites where the atom can stick, or at least have its surface diffusion lessened by bonding with another atom. We have already investigated this to some extent (see Fig. 3.7). In Fig. 3.7, S flux and substrate temperature were constant between growths and only the MoO_3 flux was increased, verified by the RBS data in Fig. 3.7(a). However, that series of experiments did not conclusively show what we might expect: that decreasing the flux of Mo to the surface decreases the nucleation density. This implies that S does play a part in limiting the average diffusion distance of Mo adatoms across the surface. To investigate the possibility of decreasing nucleation density under this model, we began attempting to keep the ratio of Mo flux to S flux constant, while diluting the mixture with added flow from the main Ar line.

Though diluting the gas mixture with Ar did show a reduction in nucleation density, run-to-run differences and variation in the slurry temperature during a given growth yielded inconsistent fluxes of precursor material to the substrate. Because the effect of diluting the gas at the substrate is discussed in chapter 5, using a more reliable cooling method, results from this investigation are not shown here. We opted at this point to switch to cooling the bubblers with cold-bath chillers, giving temperatures consistent to ± 0.1 °C. The cold-bath chillers at our disposal combined with the relatively high vapor pressure of MHC, 0.118 Torr at RT [102-103], precluded our use of MHC for this investigation, and we switched to the lower vapor pressure tungsten hexacarbonyl (WHC), $W(CO)_6$, 0.024 Torr at RT [103,121].

4.3 Limitations and Motivation for Configuration Change

In this chapter, our development of a way to effectively heat and clean Al_2O_3 was described, along with the automation of our growth process for the synthesis of single-layer TMDs. Using this Al_2O_3 heating scheme, our automated growth system and the source materials MHC and DES, single-layer MoS_2 crystals were successfully grown. We further used this method to demonstrate the importance of substrate temperature in the nucleation of MoS_2 crystals, showing that increasing the substrate temperature significantly decreases the density of features, but initiates 3D feature growth.

Variations in the liquid/solid slurry cold-bath temperature limited our ability to investigate further. To combat this, we designed, fabricated and tested our own thermoelectric-cooled cold-bath chiller, which is discussed in appendix A. With the cold-bath chillers at our disposal, including the thermo-electric cooled one we designed, we were unable to achieve the low, -45 °C, source temperature required by the MHC and proceeded by switching to the lower vapor pressure tungsten hexacarbonyl (WHC).

CHAPTER 5

SYNTHESIS OF WS_2 USING WHC AND DES

In this chapter, our use of tungsten hexacarbonyl, $W(CO)_6$, (WHC) and diethyl sulfide (DES) to grow WS_2 thin-films is described. The chamber configuration for this stage of the project was very similar to that used in the growth of MoS_2 thin films with molybdenum hexacarbonyl (MHC) and DES. The few modifications made to the chamber configuration to accomplish this are first outlined. The method used for cleaning and heating the Al_2O_3 strips was unchanged (section 4.1.2). Following the discussion of chamber modifications, is a detailing of the specific analysis methods used in this portion of the project. In the Results and Discussion section, the effect of varying substrate temperature, main Ar flow and Ar flow through the DES bubbler is shown. Some of the literature suggests that adding NaCl to the growth system has a dramatic effect on nucleation density and feature size. Results from our investigation of this are given. Then, the significant improvement in repeatability that this growth configuration and method had over the co-deposition of MoO_3 and S, discussed in chapter 3, is shown. This chapter is concluded with a summary and the motivation for further changes made to the growth method in chapter 6.

5.1 Experimental Methods

As stated above, the chamber configuration and method for cleaning and heating the Al_2O_3 substrates did not change in this stage of the growth. The liquid/solid "slurry" cold-baths were replaced with Lauda RM6 S/C liquid cold bath chillers. Because of the -21 °C minimum temperature under load of the Lauda chillers, it was necessary to switch to a lower vapor pressure transition metal precursor. The MHC bubbler was simply

replaced by a separate WHC bubbler to grow WS_2. The method for cleaning and heating of the Al_2O_3 was identical to that used in chapter 4.

5.1.1 Switch from MHC to WHC

To move away from the run-to-run inconsistencies and same growth temperature fluctuations of the liquid\solid "slurry" cold baths, discussed in chapter 4, it was necessary to switch to a transition metal precursor whose vapor pressure was lower than MHC's. Fig. 5.1 plots the vapor pressures of MHC, WHC and DES. Note that the vapor pressure of WHC is nearly an order of magnitude lower than MHC at a given temperature. First, the MHC was removed from the MHC bubbler and replaced on the chamber. Then hot Ar was flowed through the line to purge the line of any MHC deposits. This was done by wrapping heating tape around the Ar inlet line and heating it to ~ 50 °C, while flowing Ar at ~ 20 sccm through the line. The MHC bubbler was then replaced with a separate WHC bubbler (see section 4.1.1.1 for a discussion of this). 99.99% WHC (Sigma-Aldrich) was carefully loaded in a separate Pyrex tube, bubbler, like the one in Fig. 4.1(a) and added to the chamber. Like MHC, WHC is a solid white powder at room temperature. WHC powders were degassed using the freeze-pump-thaw cycle described in section 4.1.1.4.

5.1.2 Use of the Cold-Bath Chillers

The WHC and DES bubblers were suspended approximately 1 meter off the ground to allow the cold-bath chillers to be added and removed for replacement and addition of precursor material. Lauda RM6 S/C cold-bath chillers were used to cool the precursors. Though the manual lists a minimum temperature of -30 °C , it was found that under the heat load of our growth system, only -21 °C was attainable. The Lauda chillers

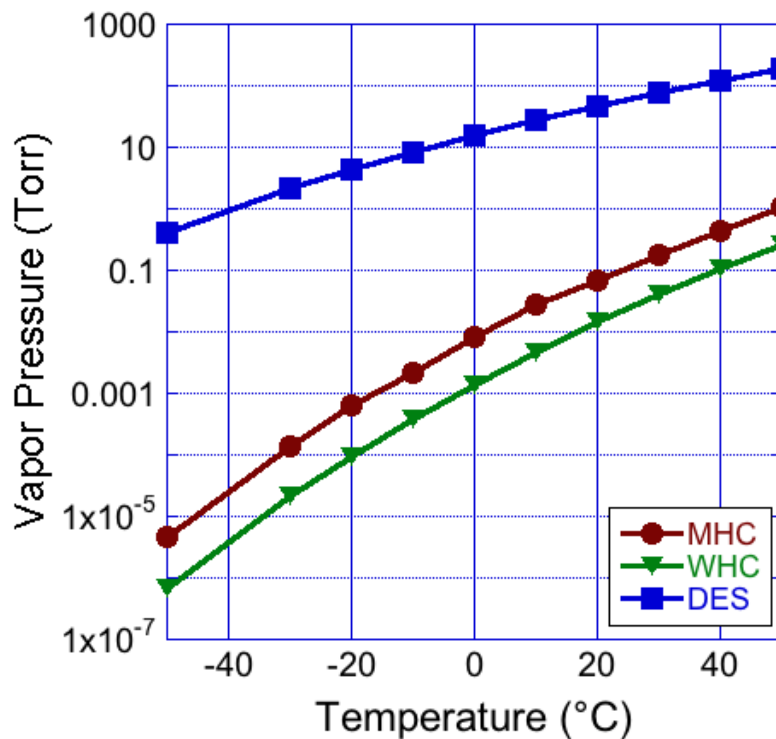

Figure 5.1: Plots vapor pressure as a function of temperature for the two precursor materials used in this study, tungsten hexacarbonyl (WHC) and diethyl sulfide (DES). The vertical axis is a logarithmic scale. The vapor pressure curve of MHC is also plotted for comparison [100,102-103,121].

were filled with a 1 : 1 mixture of ethylene glycol : water and placed so that the bubblers were submerged in the liquid. The chillers were continuously maintained at the growth temperatures, even when growth was not in process.

5.1.3 Addition of NaCl to the Gas Inlet

A commonly reported phenomenon is the dramatic increase in feature size, and corresponding decrease in feature density, when salt is added to the growth system [39,40,122]. NaCl has been shown to make the largest change in feature morphology [39]. To investigate this phenomenon, a 1" diameter x 4" section was added to the gas inlet line, such that all gas and precursor vapor were forced through the NaCl tube on their way to the sample. To prevent NaCl crystals from flowing downstream, potentially into the 75k rpm turbo molecular pump (TMP), the section was sealed off with a stainless steel (SS) mesh custom fit to our chamber. The addition was designed and fabricated to allow easy switching and replacement of salt between growths. Two kinds of NaCl were found to have a grain size large enough to prevent NaCl from being carried downstream: Morton Kosher Salt and "grade 22" NaCl (99.5 % Dominion Salt). Both were tested in this investigation. Results from this investigation are discussed in detail below.

5.1.4 Growth Preparation, Parameters and Procedure

As described in chapter 3, the prepared Al_2O_3 substrate and Si heater strip were loaded into the chamber and pumped for 30 min to achieve a pressure in the 10^{-6} Torr range. The TMP was then isolated from the main chamber and vented with N_2, before flowing ultra-high purity (UHP) Ar and H_2 through the chamber and into the mechanical pump. Once the pressure was observed to be stable over timeframes relevant to the growth, the downstream bubbler valve (BV) was open for 5 sec to allow an equilibration

between the two. This was done first for the WHC bubbler, then, after allowing 10 min for the source gases to be flushed by the flowing Ar + H_2, it was done for the DES. After waiting another 10 min for the DES to be flushed, the sample was heated to the growth temperature.

After pressure equilibration, growth was initiated by the LabVIEW program. The sample was exposed to the flow of Ar + H_2 + WHC vapor + DES vapor for the duration of the growth. After the desired growth time was reached, Ar flow through the bubblers ceased and was directed through the bubbler bypass valve (bBVs) (Fig. 4.1(a)). After this change in valve states, samples were annealed under Ar + H_2 for 15 min to account for precursor vapor still in transit from the vapor delivery system. After this annealing time, the sample was cooled to room temperature. Flow and pressure were maintained for 20 min to rapidly cool the sample and to purge the chamber of excess source vapors. The sample was then removed for analysis.

Chiller temperatures were varied from 3 °C to -8.4 °C for the DES and from -16.2 °C to -21 °C for the WHC. It was found that WS_2 films grown with the WHC chiller at -21.0 °C and the DES chiller at -2.0 °C yielded stoichiometric films (one W atom for every two S atoms, as measured by RBS), and gave the expected morphology (features with triangular footprints). Therefore, all growth presented in this chapter were done at these temperatures. Growth times from 30 min to 20 hr were performed. The pressure was varied from 10 Torr to 500 Torr, but little change was observed between "best results" at low pressure and "best results" at high pressure. Because of this, the growths presented herein were conducted at 100 Torr and 300 Torr, and is specified where relevant to the discussion.

In the investigation of the effect of growth parameters on nucleation density and feature size and morphology, the main Ar flow was varied from 2770 sccm to 4725 sccm. The effect of varying the substrate temperature was investigated varying the temperature from 545 °C to 585 °C. Flows through the WHC and DES bubblers were varied from 4.2 sccm to 20 sccm and 27.0 sccm to 60.1 sccm, respectively. No significant change was observed when varying the flow through the WHC bubbler indicating that the sublimation rate of the WHC was not high enough to saturate the Ar carrier gas. A 15 min post-growth anneal under Ar + H_2 was exclusively used for these growths, as this was calculated and observed to be enough time for any 'in transit' precursor vapor to be flushed from the chamber.

5.1.5 Characterization Methods Used

In this chapter, height mode atomic force microscopy (AFM) images were taken at the centers of the samples and were used to characterize the growths. Rutherford backscattering spectrometry (RBS) was used to verify stoichiometry. Raman spectroscopy and photoluminescence spectroscopy were attempted, but a signal was very difficult to resolve against the noise. It is suspected that this is because of the low coverage (0.1 monolayer) films investigated. Obtaining higher coverage films was precluded by the rate of Ar consumption at the flows investigated and is discussed below.

Analysis of AFM images was conducted by first obtaining the percentage of the growth surface covered by WS_2 features using Image SXM [79], as described in the chapter 3. Then we conducted an additional method of analysis on these images. First, an average height was taken of the background (BG). Image SXM allows the user to set a range of heights and compute the area of the image that exhibits that range of heights.

Knowing the height of a single layer of WS_2, a range of heights from BG + (*n*-layer height - 0.2 nm) to the BG + (*n*-layer height + 0.2 nm) was selected, where *n* is an integer up to 4. This was done for *n* = 1, 2, 3, and 4. The area of the film exhibiting a height within each range was recorded and compared to the total areal coverage. In this way we were able to determine what percent of the imaged TMD film was single-, double-, triple-, quad-, and many-layer (Fig. 5.2(c) is an example of the data obtained from this analysis). Due to the finite radius of the AFM tip, as discussed in chapter 2, there are inevitably heights measured in each image that fall between the height ranges outlined above. These are presented as "unaccounted for" percentages in the data and are presented primarily to comfort the reader with the assurance that 100% of the area was considered in the analysis. Feature size is calculated by taking the square root of the area covered by the feature. This gives a measure of length to represent feature size.

5.2 Results and Discussion

Fig. 5.2 shows features typical of those produced using WHC and DES. The reader will note that the features are typically more convincingly triangular than those obtained with MHC and DES, Fig. 4.11. We speculate that this is primarily due to the difference in purity of the transition metal source material used, 98% MHC vs. 99.99% WHC. Impurities are likely to hamper the synthesis of high-quality features that accurately reflect their crystalline structure. Fig. 5.2 also shows the effect of increasing the main Ar flow, while keeping all other parameters constant, in effect, diluting the gas mixture that reaches the sample, without changing the WHC:S ratio. The WS_2 film shown in Fig. 5.2(a) was grown at a main Ar flow of 2770 sccm, and (b) grown at the increased main Ar flow of 4725 sccm.

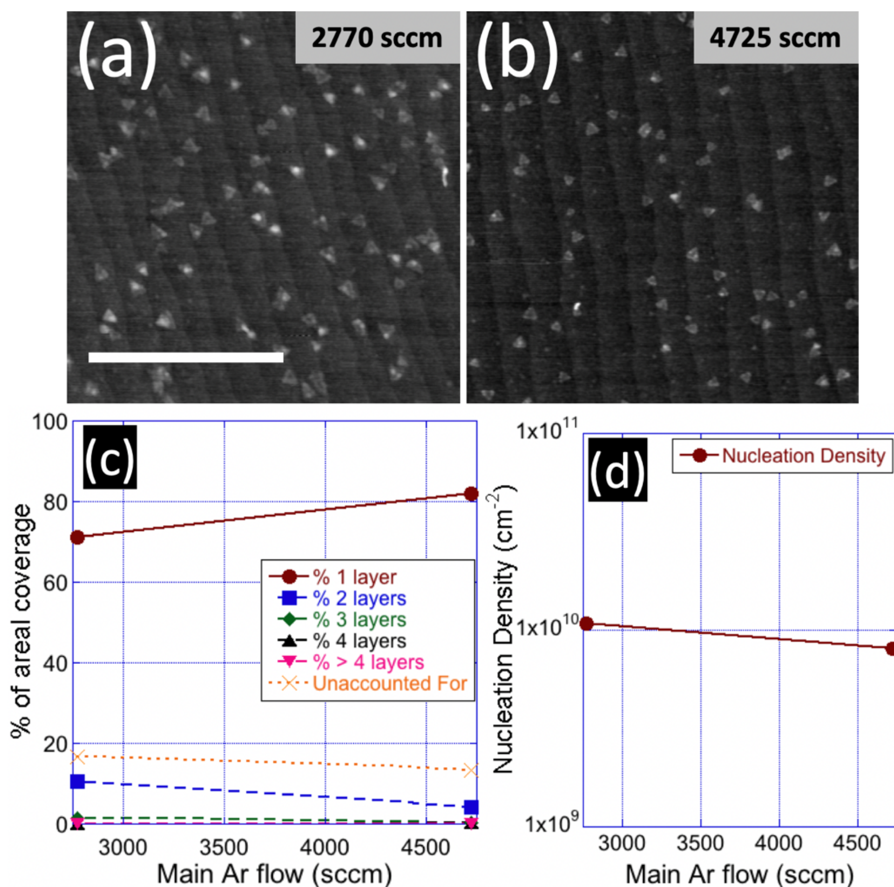

Figure 5.2: Height mode AFM images of WS_2 films grown on Al_2O_3 typical of those grown using tungsten hexacarbonyl (WHC) and diethyl sulfide (DES). Sample (a) was grown under a main Ar flow of 2770 sccm, while (b) was grown under a main Ar flow of 4725 sccm. All other parameters kept constant. The white scale marker is 500 nm and applies to both (a) and (b). (c) plots the percent of areal coverage attributable to 1 layer, 2 layer, etc. heights as a function of main Ar flow. Though feature coverage in both is at least 70% single-layer, this plot demonstrates a slight improvement in single-layer coverage by diluting the delivered gas mixture with Ar, up to 82% at 4725 sccm. Areal coverage, as determined by AFM, differs between the samples, 5.25% coverage for (a) and 2.92% for (b). (d) Nucleation density plotted as a function of main Ar flow. The nucleation density axis is logarithmic.

Immediately evident from a comparison of Fig. 5.2(a) and (b) is a decrease in areal coverage as the main Ar flow increases, the 5.25% coverage in (a) decreases to 2.92% in (b). Less obvious is the decrease in nucleation density, 1.08×10^{10} cm^{-2} in (a) vs. 8.0×10^{9} cm^{-2} in (b). This verifies the hypothesis that diluting the gas mixture that reaches the sample with Ar, decreases the nucleation density. This is plotted in Fig. 5.2(d). The subtly lower density at approximately half the coverage means that the average feature size at the increased flow decreases from 28.2 nm, at 2770 sccm, to 22.8 nm, at 4725 sccm. It is expected that longer growth times would increase the feature size without increasing the nucleation density. Thus lowering the nucleation density is advantageous to large crystal growth.

Fig. 5.2(c) shows the percentage of the covered area attributable to single- (red), double- (blue), triple- (green), quadruple- (black), or many-layer (pink) WS_2 as a function of main Ar flow. The orange line displays 'unaccounted for' data, described above. The data indicates that the film grown under a greater main Ar flow is more single-layer than the other by 12%, with decreasing percentages of the film that are > 1 layer thick. We speculate that this improvement in single-layer percentage is due to the atoms having more time to find the lower-energy feature edges at the lower deposition rate than they do at the higher deposition rate. The benefit of diluting the gas mixture is then twofold: (1) it lowers the feature density allowing for larger crystal growth and (2) increases the single-layer nature of the features.

Fig. 5.3(d) is a similar analysis of WS_2 films grown on substrates of different temperatures. Following the % 1 layer (red) curve, we see that increasing the substrate temperature from 545 °C to 585 °C, dramatically decreases the % coverage of single

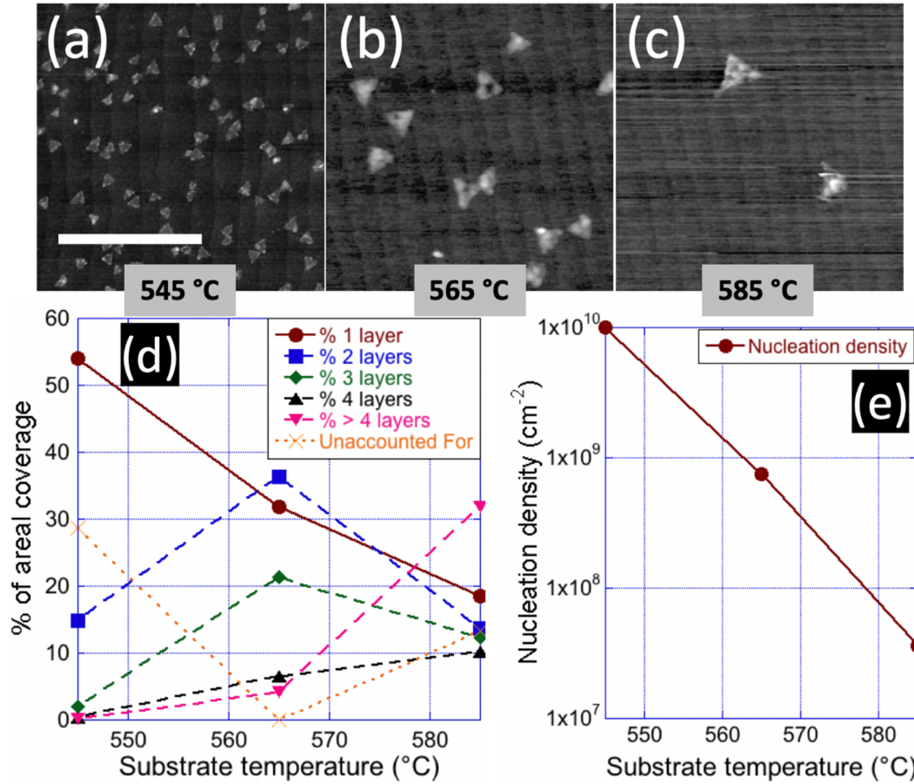

Figure 5.3: (a)-(c) height mode AFM images of WS_2 films grown on Al_2O_3 substrates at temperatures of (a) 545 °C, (b) 565 °C and (c) 585 °C. The white scale marker is 500 nm and applies to (a), (b) and (c). All samples were grown under a main Ar flow of 2770 sccm for 4 hr with all other parameters kept constant. (d) plot of the % of areal coverage attributable to 1 ML, 2 ML, etc. as a function of substrate temperature. Shows that as the substrate temperature is increased from 545 °C to 585 °C, the percentage of single-layer coverage decreases from 54% to 18% and the percentage of multi-layer growth increases. (e) Nucleation density as a function of substrate temperature. The nucleation density axis is logarithmic. A decrease in nucleation density from 1.0 x 10^{10} cm^{-2}, at 545 °C, to 3.6 x 10^{7} cm^{-2}, at 585 °C, agrees with our previous observation that increasing the substrate temperature decreases the nucleation density, though at the cost of producing multi-layer crystals.

layer from 54% to 19%. The curves for 2 layers (blue) and 3 layers (green) increase significantly going from 545 °C to 565 °C before dropping at 585 °C. The reason for this decrease at 585 °C is evident in the 4 layers (black) and > 4 layers (pink) curves. The 4 layers curve continues almost linearly with temperature, while the > 4 layers experiences a gradual increase from 0% at 545 °C, to 5% at 565 °C, followed by a large jump to 32% at 565 °C.

Fig. 5.3(a)-(c) show height mode AFM images of samples grown at a substrate temperature of 545 °C, 565 °C and 585 °C, with all other parameters held constant. The trend shown by this data agrees with what is shown in Fig. 4.11, that increasing the substrate temperature has the effect of significantly decreasing the nucleation density of the film, from 1×10^{10} cm^{-2} at 545 °C to 3.6×10^{7} cm^{-2} at 585 °C, as shown in Fig. 5.3(e). Though decreasing the feature density is a good thing, from the perspective of obtaining larger area crystals, Fig. 5.3(d) shows that increasing the substrate temperature also increases the number of vertically stacked WS_2 layers in the film. As discussed in the introduction, the exciting properties of transition metal dichalcogenides (TMDs) exist in single-layer films, so increasing the substrate temperature further to produce larger area features with WHC and DES is ultimately detrimental to the aim of the research. The reason for this switch to vertical growth at higher substrate temperatures is somewhat perplexing. Weak van der Waals interactions between WS_2 layers should mean that W atoms are more likely to find a low energy site to bond to at the edge of the feature than on existing WS_2 layers. By the growth model discussed in chapter 4, increasing the substrate temperature should actually improve the percentage of single-layer coverage by providing W adatoms more energy with which to overcome the van der Waals

interactions, but this is not what is observed. It is possible that this vertical growth is attributable to defects in the existing WS_2 layers. Another possible explanation is that catalytic decomposition of one of the precursors on top of existing WS_2 triangles increases with substrate temperature. This would lead to an increased density of precursor constituent moieties on the WS_2 feature, inducing nucleation atop the feature. Such selective decomposition of precursors on semiconducting and metallic surfaces over insulating ones is relied upon in selective CVD methods.

Another possibility is that there is insufficient S to populate the edge states during growth, preventing Mo adatoms from bonding at the edges. To investigate this possibility, Ar flow through the DES bubbler was increased. Doing this, a similar trend to that shown in Fig. 5.3(d) was observed (see Fig 5.4(d)). Increasing the flow through the DES bubbler carries more DES in the gas mixture delivered to the substrate, decreasing the DES/WHC ratio at the growth surface. The plot in Fig. 5.4(d) shows that as the Ar flow through the DES bubbler was increased from 27.0 sccm to 41.6 sccm, the % of single-layer coverage decreased from 71% to 46%. A further decrease to 31% was observed when the flow was increased to 60.1 sccm. Percent coverage of multi-layer growth correspondingly increases. Figs. 5.4(a)-(c) show height mode AFM images of the WS_2 films synthesized using these flows. Analysis of these AFM images reveal that as the flow through the DES bubbler increases, the nucleation density decreases from 1.08×10^{10} cm^{-2} at 27.0 sccm to 3.40×10^{9} cm^{-2} at 41.6 sccm, down to 7.44×10^{8} cm^{-2} at 60.1 sccm. This trend in nucleation density is also plotted in Fig 5.4(e).

Like what was observed when increasing the substrate temperature, the average feature size increases with the flow through the DES bubbler, from an average feature

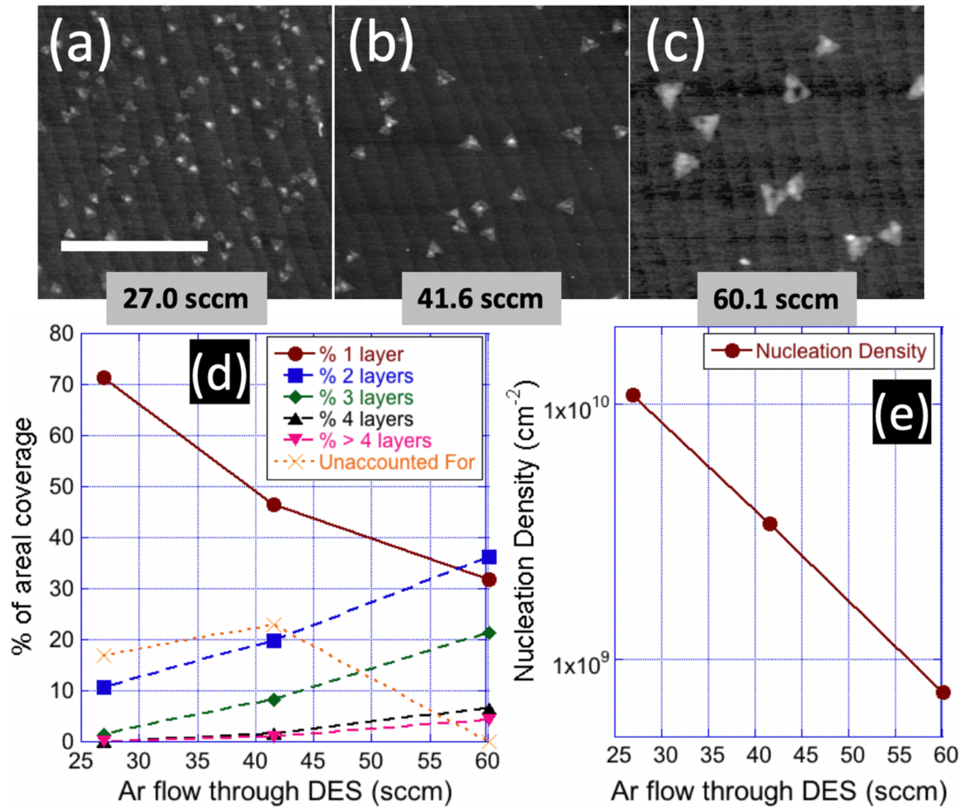

Figure 5.4: (a)-(c) height mode AFM images of WS_2 films grown with Ar flows through the DES bubbler of (a) 27.0 sccm, (b) 41.6 sccm and (c) 60.1 sccm. The white scale marker is 500 nm and applies to (a), (b) and (c). All samples were grown under a main Ar flow of 2770 sccm for 4 hr with all other parameters kept constant. (d) plot of the % of areal coverage attributable to 1 layer, 2 layer, etc. as a function of Ar flow through the DES bubbler. Shows that as the Ar flow through the DES bubbler is increased from 27.0 sccm to 60.1 sccm, the % of single-layer coverage decreases from 71% to 31%, and the percentage of multi-layer growth increases. (e) Plot of nucleation density as a function of flow through the DES bubbler. The nucleation density axis is logarithmic. A decrease in nucleation density from 1.08 x 10^{10} cm^{-2} at 27.0 sccm to 7.44 x 10^{8} cm^{-2} at 60.1 sccm is shown.

size of 28.2 nm at 27.0 sccm to 66.8 nm at 60.1 sccm, albeit at the cost of decreasing the percentage of single-layer growth. This observation indicates that the 3D growth seen at higher growth temperatures is not a result of too little DES. It also lends credence to the speculation that 3D growth is either a result of defects introduced to the features, or the catalytic decomposition of precursors on top of the existing WS_2 features. Under the "defect hypothesis", an increased flux of DES, $C_4H_{10}S$, could produce increased interstitial defects of C atoms in the features, providing low energy sites on the WS_2 surface for additional layer nucleation. Under the "catalytic decomposition hypothesis", an increase in DES flux would provide more of the catalytically decomposed precursor, DES, to the top of the WS_2 feature, increasing the likelihood that some moiety of the precursor materials is formed, nucleating an additional layer of growth.

This result that increasing the flow through the DES bubbler decreases nucleation density is interesting as it disagrees with ref. 36, who observe the opposite with an increase in DES in their MoS_2 films. Their films are grown with MHC and DES in a hot-wall tube furnace. Their results, given in the supplementary information of that publication, show that increasing the DES delivered to or decomposed at the growth surface increases the nucleation density and decreases the feature size, without any reported indication of inducing multilayer growth. They argue that this is due to the decreased surface diffusion of Mo adatoms, as MoS_x should have a lower surface diffusion than Mo. It's difficult to argue with this logic and we speculate that our observation of a reduction in nucleation density is a result of increased ripening of the WS_2 nanocrystals under the increased flux of S. X. Zhang et al. and T. H. Choudhury et al. have shown that ripening does occur under a chalcogen flux, an observation confirmed

by our work, which is discussed in chapter 6 [55-56]. The fact that the hot-wall grown films reported by K. Kang et al. [39] showed no multilayer growth in their experiments provides further evidence for the catalytic decomposition hypothesis. In a hot-wall reactor, chemical reactions are not isolated to the sample surface and precursor decomposition can easily occur in the gas-phase prior to substrate impingement. In our cold-wall configuration, precursor decomposition is isolated to the sample surface where both thermolysis on the sapphire substrate and catalytic decomposition atop existing WS_2 islands are in competition.

Summarizing the results up to this point, we found it easy to grow single-layer WS_2 films, decrease the feature density and even increase the size of the features. However, due to an unidentified parameter, larger samples grown at lower nucleation densities resulted in multi-layer growth. The only instance when this did not occur was when increasing the main Ar flow. Using the highest flow presented herein, 4725 sccm, it was necessary to grow for 20 hr in order to get measurable coverages. This equates to 4.7 L of Ar per minute flowed through the chamber for 20 hr. After 20 hr at 4.7 L/min, the Ar cylinder was exhausted, precluding investigation of longer growth times. Continuing to increasing the flow of Ar was not a choice, because it would increase the growth time required to achieve appreciable coverage, while increasing the rate at which we ran out of Ar. Thus, we could not pursue this effect further.

As mentioned above, a number of publications in the literature suggest that adding salt to the gas line dramatically improves feature size, with NaCl yielding the best results. The argument made by these papers is that adding NaCl to the gas line acts as a desiccant, and that dehydrating the environment improves the growth kinetics

[39,40,122]. We investigated this phenomenon by adding NaCl to our gas line as outlined in section 5.1.3. We tried different purities of NaCl, changing the NaCl between growths and varying the mesh size of the NaCl. After many growths, we were forced to conclude that the NaCl offered no significant improvement to the growth for our setup and growth method. Fig. 5.5 shows identically grown samples, (a) grown with no NaCl in the gas line and (b) grown with NaCl. As evident by Fig. 5.5, average feature size is essentially unchanged from 44.5 nm without NaCl to 44.3 nm with NaCl. Similarly, nucleation density is largely unchanged, decreasing slightly from 3.8 x 10^9 cm^{-2} without NaCl to 3.05 x 10^9 cm^{-2} with NaCl. The average size and nucleation density for the with NaCl growths are taken from the statistical analysis of 3 identically grown samples (see Fig. 5.6 and Table 5.1). We speculate that the reason this addition did not affect our growths, as it has for others, is either because evacuating the chamber to 10^{-6} Torr prior to growth does a better job of evacuating the chamber than other methods, or because the high flows used (~2800 sccm total flow) too quickly saturated the NaCl desiccant. One must suspect, however, that any H_2O in the process, or any polarized impurities, for that matter, come from the chamber walls or from either the DES or MHC. It is therefore unlikely then that the high flows are a cause of rapidly saturating the NaCl.

Using these WS_2 growths, with NaCl in the gas line, we checked the repeatability of our growths. Fig. 5.6 shows height mode AFM images of three identically grown samples. In our experiments with MoS_2 growths using MoO_3 and S as the source materials, we demonstrated excellent repeatability in coverage, to within 0.03 ML, but a lack of repeatability in feature size and nucleation density. Fig. 5.6 and Table 5.1 show

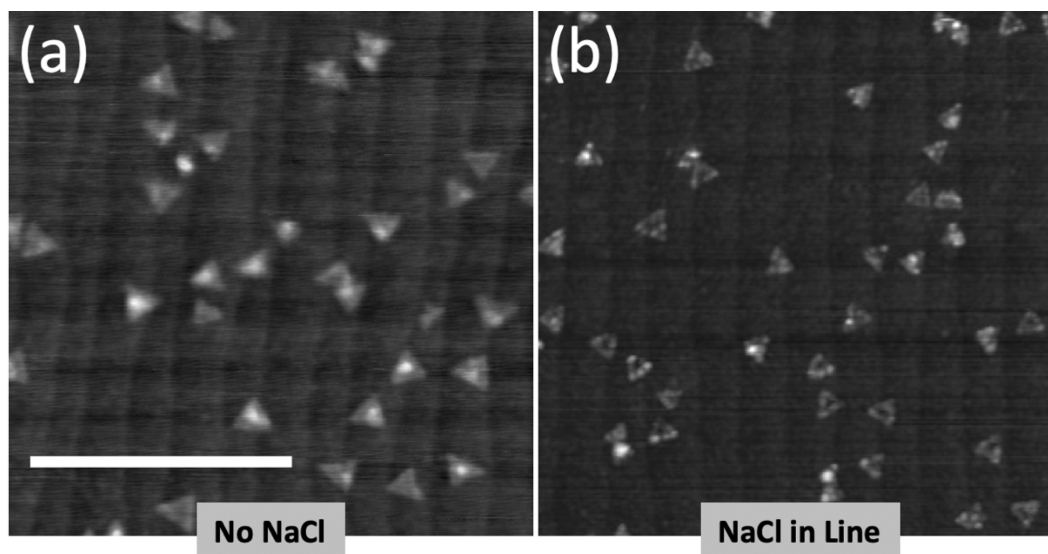

Figure 5.5: Height mode AFM images of WS_2 films grown (a) with and (b) without NaCl in the gas inlet line. The white scale marker is 500 nm and applies to both images. All growth parameters were the same between the two growths. This shows that where feature morphology between the samples is not identical, no dramatic improvement in feature size was observed with our growth configuration, as has been reported for other groups.

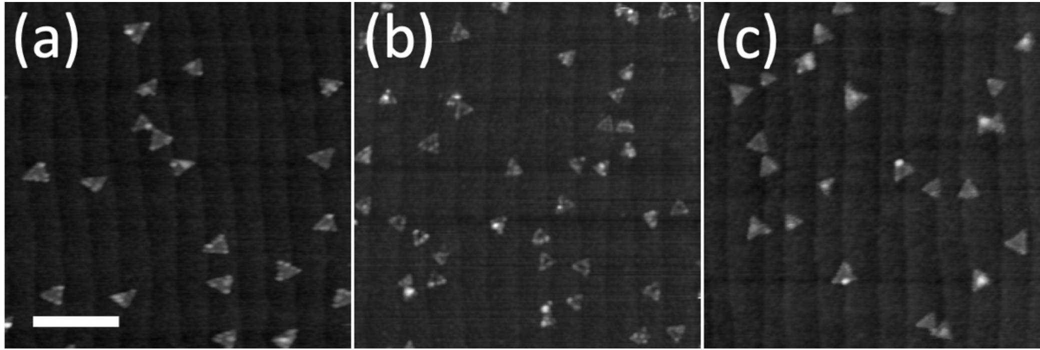

Figure 5.6: Height mode AFM images of three identically grown WS_2 films with NaCl in the gas line. Scale bar for all three images is 250 nm. These images show that this growth method with these sources produces repeatable feature morphology from growth-to-growth.

that under this growth configuration and using these source materials, we were able to retain exceptionally high run-to-run repeatability in coverage, 0.056 ± 0.007 ML, while also demonstrating run-to-run repeatability in both average feature size, 44.3 ± 3.1 nm, and nucleation density, $3.05 \pm 0.7 \times 10^9$ cm^{-2}.

Fig.	**Coverage (ML)**	**Avg. size (nm)**	**Density (cm^{-2})**
5.6(a)	0.051	47.4	2.22×10^9
5.6(b)	0.065	39.9	4.02×10^9
5.6(c)	0.052	45.1	2.90×10^{10}
Average	0.056 ± 0.007	44.3 ± 3.1	$3.05 \pm 0.7 \times 10^9$

Table 5.1: Summary of the monolayer coverage, measured by AFM at the center of the substrate, with average WS_2 nanocrystal size and nucleation density for the samples shown in Fig. 5.6. The nanocrystal sizes are square root of the areas covered by those of the features in the AFM images. At least 200 nanocrystals were involved in the statistical analysis of each sample.

5.3 Limitations and Motivation for Configuration Change

Using WHC and DES to grow WS_2 thin-films on Al_2O_3 was demonstrated to be a significant improvement over the previous method of co-depositing MoO_3 + S on a SiO_2/Si substrate. Further demonstrated was the ability to grow single-layer WS_2 films, with a dramatic improvement in feature morphology by switching to the cold-bath chilled, high purity WHC from the "slurry" cold-bath cooled MHC. Using WHC and DES, it was shown that increasing the main Ar flow slightly decreases nucleation density, while maintaining, or improving, the percentage of the grown area that is 1 ML tall. It

was further demonstrated the increasing the substrate temperature and the flux of DES to the sample, by increasing the Ar flow through the DES bubbler, has the effect of decreasing the nucleation density and increasing the feature size, but induces multi-layer growth. The popular addition of NaCl to the gas line was also investigated, showing that, at least for our growth configuration and sources, it made no difference. Lastly, it was demonstrated that with this growth method and configuration, we were able to repeat growths with a high degree of consistency, both in terms of coverage and morphology.

As discussed in the text above, our attempts to turn our improved repeatability and understanding of the effect of individually varying the growth parameters to produce large-scale single-layer, single-crystal TMDs was hampered by the presence of a currently unidentified parameter that induced multi-layer growth whenever we tried to increase the feature size. We speculate that this hinderance had to do with the impurity of the DES, only 98%, and/or the presence of excess C from the DES, $C_4H_{10}S$ and WHC, $W(CO_6)$. In an effort to eliminate these possibilities, we drew on the literature. Choudhury et al. reports an improvement in growth by switching from DES to H_2S [56, 123], and we elected to switch to an H_2S S source.

CHAPTER 6

SYNTHESIS OF WS_2 USING WHC AND H_2S

In this chapter, our use of tungsten hexacarbonyl (WHC) and hydrogen sulfide, H_2S, to grow WS_2 thin-films is described. Switching the S precursor from diethyl sulfide (DES) to H_2S required modifications to the chamber configuration, modifications to the LabVIEW program, detailed in section 4.1.1.4, and the design of a new heater to heat the Al_2O_3 substrates. These changes and developments are outlined in the experimental methods section of this chapter. Following that discussion is a detailing of the specific analysis methods used to characterize growth trends of WS_2 on Al_2O_3. In the Results and Discussion section, the effect of varying substrate temperature, H_2S flow and annealing, post-growth, in an H_2S flux is shown. Finally, the high repeatability and uniformity of this method are demonstrated. This chapter is concluded with a summary and the motivation for future changes.

6.1 Experimental Methods

As stated in the previous chapter, the use of DES as a source of S seemed to be what was limiting our ability to grow sufficiently large features for careful analysis [56]. It was therefore decided to switch from DES to H_2S. Because of the highly flammable, "fatal if inhaled" nature of H_2S, careful modifications to the chamber were required to accomplish this. These significant changes to the growth configuration necessitated a minor update to the LabVIEW program. Early in the investigation of H_2S as a S source, we found that H_2S somehow enabled the transport of Si to the growth surface. We identified the Si heating strip (described in chapter 4) as the source of Si and designed and tested a new heater to eliminate Si from the growth chamber. With the switch to this

new heater, we also began controlling the temperature of the substrate with a Eurotherm temperature controller in communication with the pyrometer and the power supply used to heat the sample.

6.1.1 Switch from DES to H_2S

To move away from the suspected limitations of DES, discussed in chapter 5, and in response to a few publications indicating that H_2S is a more stable source of S that yields better TMD films [56,123], we switched to H_2S as a precursor for S. At room temperature, H_2S is maintained as a liquid under its own vapor pressure, 252 psi, 13.0 kTorr. This highly toxic, highly flammable gas required significant care in both handling and in design of how the chamber was modified to accommodate it.

227 g of 99.5% H_2S were acquired from Praxair and added to the reaction chamber. Fig. 6.1(a) shows a schematic of the H_2S control system designed to safely employ the precursor. The H_2S was housed in a lecture bottle, with a 1 psi check valve (CV) immediately downstream to prevent backflow of gasses into the lecture bottle, contaminating the H_2S. A single-stage Tescom 44-2200 metal-to-metal diaphragm-to-body sealed regulator then stepped down the 252 psi H_2S vapor pressure to the 25 psi needed by the mass flow controller (MFC). This pressure was monitored by an inline pressure gauge (PG). The flow of H_2S into the chamber was controlled by a 20 sccm full-range MFC. Unlike the bubbler system used with DES, H_2S vapor is not "carried" by a carrier gas to the chamber, but rather flowed into the chamber and transported as a result of pressure differentials. As a failsafe, a Swagelok SS-DLV51 stainless steel high purity, high pressure shutoff valve (SOV), labeled "SOV 2" in 6.1(a), is placed downstream of the MFC. Farther downstream is a gas inlet SOV, which can isolate the chamber from all

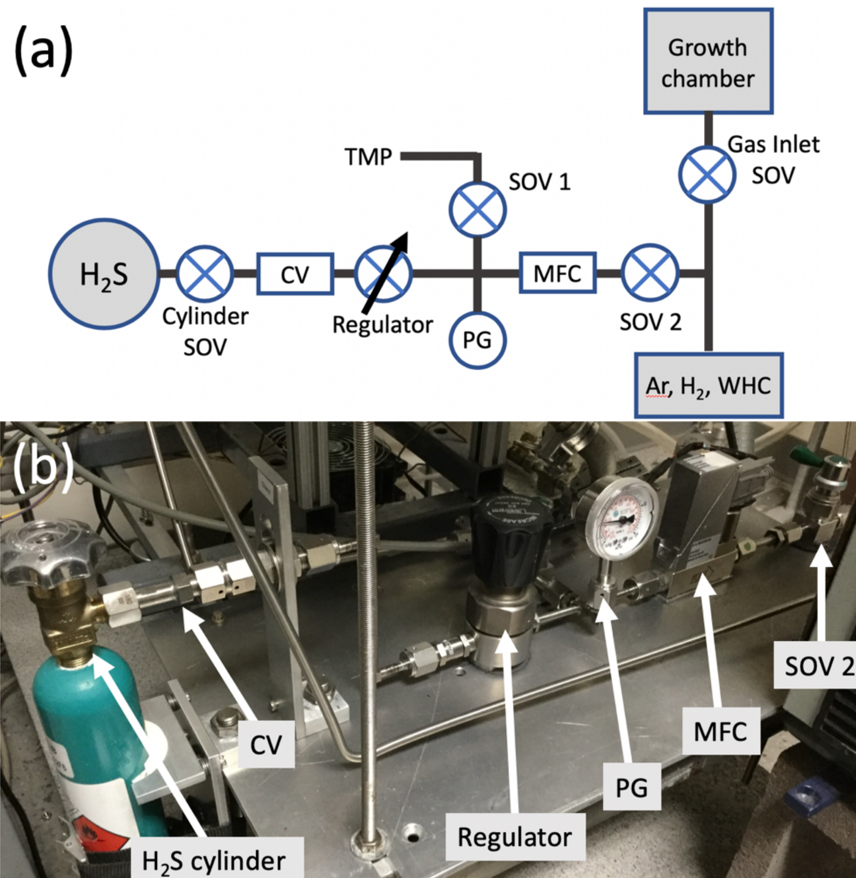

Figure 6.1: (a) Schematic of the H_2S control system used to introduce H_2S to the chamber. H_2S passes through the cylinder shutoff valve (SOV) to a 1 psi check valve (CV). A single-stage regulator reduces the 252 psi vapor pressure of the H_2S to the 25 psi required by the MFC for operation. This pressure is monitored by a pressure gauge (PG) upstream of the MFC. The line passes through SOV 2 before reaching the gas inlet SOV and finally the chamber. Note that the line is also equipped with a secondary pathway leading from the regulator, through SOV 1 and into the turbomolecular pump (TMP). This secondary line was used for evacuation of the H_2S line prior to growth and during configuration changes. (b) Labeled photograph of the realization of the schematic in (a). The secondary line is obscured by the chamber hardware and is not visible in (b).

gas sources. An additional Swagelok SS-DLV51 SOV, labeled "SOV 1" in 6.1(a), allows the line to be opened directly to the turbomolecular pump (TMP). This line was included for the evacuation of the H_2S line. Fig. 6.1(b) is a photograph of the realization of the schematic in (a). Since the H_2S flux was controlled by the flow through the MFC, the H_2S was maintained at room temperature.

6.1.2 Updates to the LabVIEW Control Program

The method of controlling Ar, H2, and WHC with the LabVIEW control program were unchanged. As the SOVs on the H_2S line are all manually controlled, the LabVIEW program was updated to merely control the flow of H_2S through the H_2S MFC. Because of the danger involved in working with a gas like H_2S, the program was also modified to include a "kill" button. This large, brightly-colored button on the user interface immediately closes all pneumatic valves, sets all MFC control voltage outputs to zero and stops the program. This feature allows the user, in a dangerous, high-stress situation, to end all gas flows before closing SOV 2, closing the cylinder SOV and exiting the room to safety.

6.1.3 New Heater Design

As was mentioned above, early growths with H_2S were performed using the Al_2O_3 heating method outlined in section 4.1.2, heating a Si heater strip Sn bonded to an Al_2O_3 substrate. These early films occasionally showed excellent feature morphology, with highly triangular features with a base length of ~ 60 nm. This indicated that the use of H_2S held promise. However, RBS analysis of these early growths showed the presence of Si in many of the films. Si was absent in the films with promising morphology. A number of experiments coupled with the careful cleaning of all the parts of the sample

holder and its surroundings indicated that this phenomenon only occurred during and after growths utilizing a high Si heater strip temperature, > 700 °C, and after 2 - 3 growths at lower temperatures, ~ 650 °C. We attempted substituting the Si heater strip with SiO_2/Si and Si_3N_4/Si heater strips, but were unsuccessful in eliminating the presence of Si on the growth surface. H_2S adsorption on Si(100) has been investigated [124-125]. These studies revealed that H_2 is desorbed from the Si surface as S atoms migrate into the substrate, and report that no Si species were desorbed. This is an interesting phenomenon that warrants further exploration, but is outside the scope of this project. Though we did not investigate the cause of this further, we concluded that Si could no longer be used as a heater for the sapphire.

To circumvent the use of Si as a heater and pursue the promising early results, we designed and implemented a new W heater for our Al_2O_3 substrates. In anticipation of the eventual possibility that a different method for heating Al_2O_3 would be needed, we had previously conducted a series of experiments to check the viability of W at temperature under growth conditions. These experiments were done to determine whether a hot W strip would sulfurize, presumably to WS_2, and whether that sulfurization would prevent the use of W as a heater material. These experiments were conducted during our experimentation with MHC and DES to grow MoS_2 films by inserting a W strip downstream from the MoS_2 growth and heating it to ~ 600 °C. This procedure was followed using the same W strip for 10 MoS_2 growths. The W strip was visibly sulfurized by the exposure. In spite of the sulfurization, the strip retained its electrical conductivity, and we were able to continue to heat it for all 10 of the experiments.

Therefore, our new heater design, shown in Fig. 6.2, utilized 26 mm x 2 mm strips cut from a sheet of 0.005" thick W. As it was unclear how long the W strip would last, especially under varying growth temperatures and times, the heater was designed to allow the W heater strip to be easily changed. The heater was also designed to minimize exposure of the W strip to the hot sulfurous environment. This was done by including a pyrolytic boron nitride (PBN) bottom plate, to shield the exposed underside of the W. A channel was milled into the top of the PBN bottom plate in which the W strip could lay. The walls of this channel shielded the sides of the W strip.

The Ta electrodes, arrowed in Fig. 6.2(c), were designed with opposing recessed areas for the PBN bottom plate to rest in. The W was then placed in the channel on top of the PBN bottom plate and held in place, sandwiched on each side between a Ta clamp piece and the Ta electrode. The Ta clamp pieces were bolted to stainless steel (SS) nut plates located underneath the Ta electrodes. The top of the W strip was shielded from the sulfurous environment by the Al_2O_3 substrate, which was held in place by two additional Ta clamp pieces bolted to the SS nut plates underneath the Ta electrodes.

Fig. 6.2(a) is a semi-exploded view of this design. Fig. 6.2(b) shows a cross-sectional view taken perpendicular to the long axis of the W strip. This view shows how the W strip is shielded on the top, sides and bottom from the sulfurous environment. (c) is a photograph of the heater, with a labeled Al_2O_3 substrate. Also visible in the image are the PBN pieces used to electrically isolate the heater from the sample holder. These pieces are visible under the Ta electrodes. A current is run through the W strip, resistively heating it to the target temperature. By a combination of contact and radiative heating, the Al_2O_3 substrate is heated.

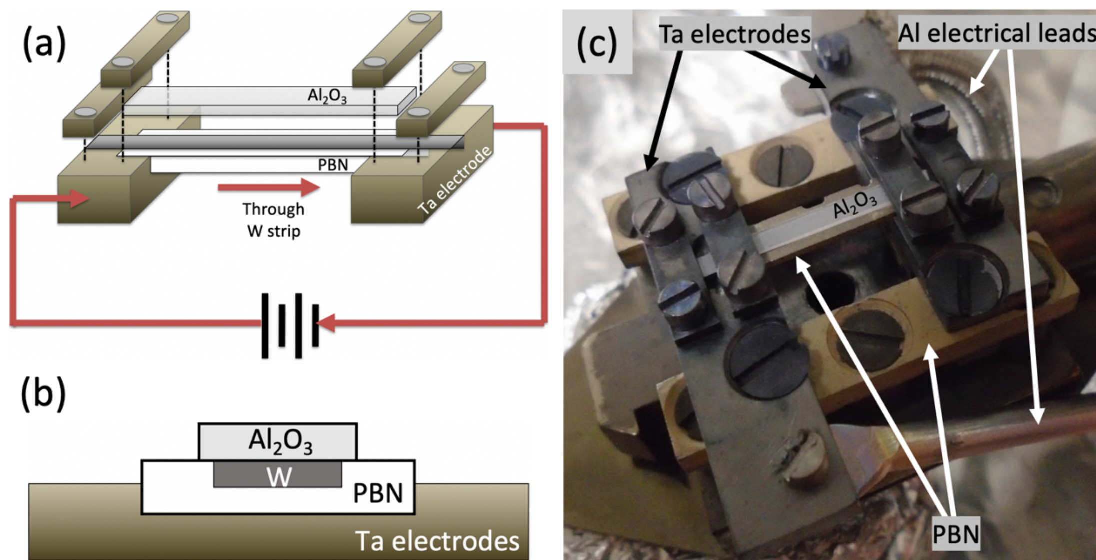

Figure 6.2: (a) Semi-exploded view of the sample heater implemented for this stage of the growth. A channeled piece of pyrolytic boron nitride (PBN) rests in opposing recesses machined into the Ta electrodes (labeled in (a), (b) and (c)). A W heater strip lays atop the channeled PBN and is clamped to the Ta electrodes by two Ta pieces, bolted to underlying stainless steel (SS) nut plates. The Al_2O_3 substrate is placed on top of this assembly and clamped down with two separate Ta pieces bolted to the SS nut plates. A current is passed through the W strip, resistively heating it, which in turn heats the Al_2O_3 substrate. (b) Cross-sectional view showing that all faces of the W heater strip are covered either by the PBN bottom plate or the Al_2O_3 substrate. (c) Photograph of the realization of this design.

Additionally visible in 6.2(c) are the Al electrical leads used to deliver current to the sample holder. These electrical leads are connected to the bottoms of the Ta electrodes with Mo screws. Phosphor bronze leads were used for all the work done with the Si heating method, but the switch to a W heater strip required significantly larger currents (approximately 3 A for Si and 32 A for W) to reach the target temperatures. As the phosphor bronze leads sulfurized, electrical contact between them and the Ta electrodes changed, causing inconsistent temperature profiles and, occasionally, the loss of electrical contact mid-growth. For the ~ 200 growths performed with Al leads, they never showed signs of sulfurization. The drawback to using Al so close to a hot W strip, regularly at 775 °C during growth, is its 660 °C melting point, which limited the range of substrate temperatures we could explore (discussed below).

A calibration of the sapphire temperature as a function of heater temperature, similar to that described in section 4.1.2 was conducted. As the sapphire is transparent to the IR pyrometer, the pyrometer measured the temperature of the W strip. Fig. 6.3 shows the results from this calibration. In an attempt to improve the agreement between the W and the Al_2O_3 temperatures, the width of the Al_2O_3 substrate was reduced from 3.9 mm, the width used for the WHC + DES and MHC + DES work, to 2.5 mm, 0.5 mm wider than the W strip. This change reduced the difference in temperature between the W and the sapphire substrate surface from 65 °C to 45 °C at a W temperature of 750 °C.

As experience was gained with this heater, it was found that the W heater strip needed to be changed approximately every 20 hr of usage. After that, the surface of the W was found to crumble off as a fine grey powder, presumably WS_2. An additional effect of exposure was the deformation of the W strip, which under thermal expansion caused

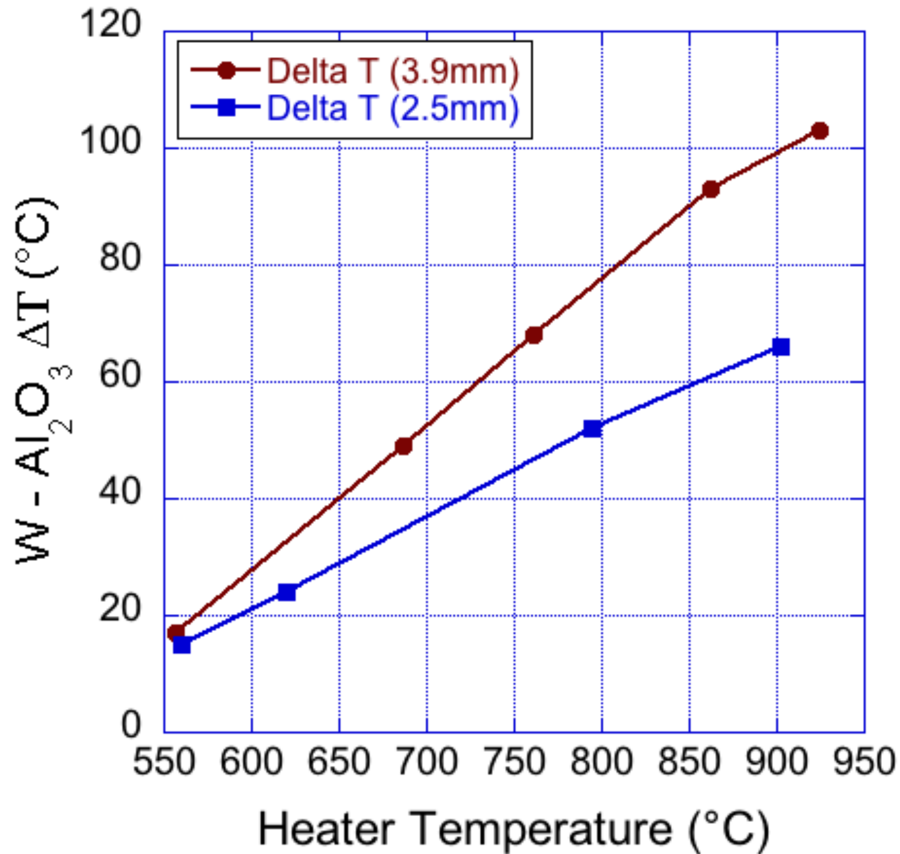

Figure 6.3: Plots the difference in temperature between the W heating strip and the Al_2O_3 growth surface as measured by the thermocouples, $T_{W,TC}$ - $T_{Sapphire,TC}$, as a function of the heater temperature measured by the pyrometer, $T_{W,pyrometer}$. The curves were obtained with two widths of Al_2O_3 substrates, indicated in the legend, clamped to the heater as described above (see Fig. 6.2). The data shows a dramatic improvement the agreement between the Al_2O_3 and W when a narrower sample is used, from a ΔT of ~ 65 °C with a 3.9 mm sample, to 45 °C with a 2.5 mm sample, at a heater temperature of 750 °C.

the Al_2O_3 sample to break during growth, altering the thermal contact between the Al_2O_3 and the W heater strip and rendering the growth useless. We also observed that, for some unidentified reason, exposure of the hot W strip to H_2S changed the heating properties of the W. After approximately 1 hr of exposure to H_2S, the power needed to maintain the setpoint temperature of the heater gradually increased from ~ 110 W to ~ 130 W. We attempted to compensate for this by using a Eurotherm PID controller in communication with the pyrometer and a slaved power supply to control the temperature of the heater. In spite of this, every first growth with a new W strip yielded a bimodal distribution of WS_2 features, which we interpreted to be indicative of growth at two distinct temperatures. Identical growths with the same strip on subsequent uses was consistently devoid of the bimodal distribution and mid-growth rise in power. Fluctuations in temperature resulting from subtle changes in electrical resistance was an obvious suspect. But, with the pyrometer controlling the temperature, we speculate the change is in the thermal contact between the substrate and the sulfurized heater strip.

6.1.4 Growth Procedure and Parameters

To help elucidate this section, it is first necessary to give a brief overview of the route taken to obtain samples with features large enough for analysis and the subsequent investigation of the parameter space. First, the substrate temperature was increased until samples with WS_2 features large enough for analysis were grown. Then, the flow of H_2S was varied to determine if this combination of precursors behaved in the same way as the WHC + DES samples, discussed in section 5.2. Following this, the effect of annealing the samples in H_2S was investigated.

The growth procedure for obtaining these films is first discussed, followed by an outlining of the parameters used in the growths. Note that two varieties of annealing are referred to in this chapter: (1) the 15 min anneal in Ar + H_2, that was used in the methods described in chapters 4 and 5 to prevent precursor material still in transit from reaching a "cold" substrate and (2) an anneal in Ar + H_2 + H_2S, which for simplicity is referred to herein as an anneal in H_2S. Both occur after the flow of Ar though the WHC bubbler has been terminated, and the anneal in H_2S occurs before the anneal in Ar + H_2.

Prior to loading in the heater described above, samples were cleaned per the description in section 4.1.2. The chamber was evacuated by pumping with the TMP for ~ 30 min to achieve a pressure in the 10^{-6} Torr range. The TMP was then isolated from the growth chamber and vented to atmospheric pressure with N_2. Following this, the flow of Ar and H_2 was initiated by the LabVIEW program and the pressure stabilized with the pressure control valve (PCV), as has been done throughout. Once the pressure was observed to be stable over timeframes relevant to the growth, the WHC bubbler was equilibrated to the growth chamber pressure by opening the downstream bubbler valve (BV) for 5 sec. 10 min were waited for remnant precursor vapor to be flushed before the H_2S cylinder SOV, and the SOV labeled "SOV 2" in Fig. 6.1 were opened. Another 10 min were waited before the capacitance manometer was isolated from the chamber and the heater temperature ramp-up procedure was started.

As stated above, sample temperature was PID controlled by a Eurotherm temperature controller to a manually entered setpoint temperature. The heater temperature ramp-up procedure varied, depending on the target temperature, but the ramp-up to 775 °C is detailed here as an example. A ramp-up procedure was used in

place of going from room temperature to the growth temperature in an attempt to minimize any mechanical stresses on materials in the heater due to differences in coefficients of thermal expansion. The room temperature heater was first increased to 525 °C and maintained there for 10 min. This temperature was chosen because it is well above the minimum temperature that the IR pyrometer could measure, which was about 350 °C. Then the setpoint was increased to 650 °C. After 10 min at 650 °C, the setpoint was increased to the heater temperature, 775 °C, which gave the desired substrate temperature of 730 °C. This temperature was maintained for 5 min.

At this point, H_2S flow was initiated in the LabVIEW program. MFCs are PID controlled devices and as such require an amount of time to stabilize at a given flow. This is usually on the order of seconds. To account for this and to allow the flow to reach a steady-state value, 5 min were allowed before continuing. Note that we have again relied on the assumption that S will not stick to a hot substrate without the presence of the transition metal precursor. At this point, growth was initiated in the LabVIEW program by redirecting the flow of Ar in the WHC line to pass through the WHC bubbler, beginning the delivery of WHC to the substrate.

After the determined growth time, the flow of Ar through the WHC bubbler was redirected through the bBV, ending the flux of WHC from the bubbler. Simultaneous with this, flow through the H_2S MFC was stopped by providing it a 0 V control voltage, and the H_2S cylinder and SOV 2 were closed. The sample was then annealed for 15 min at the growth temperature under a flow of Ar and H_2 for 15 min. Following this anneal, the sample was rapidly cooled to room temperature before removal for analysis.

All WS_2 growths presented in this chapter were conducted with the WHC submerged in a Lauda RM6 S/C cold-bath chiller held at -21 °C. All growths employed the same main Ar flow, 1550 sccm, Ar flow through the WHC bubbler, 7.7 sccm, H_2 flow, 25 sccm, and pressure, 100 Torr. The main Ar flow was kept low, compared to the 4725 sccm used in chapter 5, to limit growth times, expediting the investigation of growth trends. Drawing on the trends presented in chapters 4 and 5, the heater temperature was varied to obtain features large enough for analysis, from 700 °C to 775 °C, corresponding to substrate temperatures from 663 °C and 730 °C. Higher temperatures were not investigated as a precaution against melting the Al electrical leads bolted to the Ta electrodes, as discussed in section 6.1.3. All samples were grown in a flux of WHC and H_2S for 4 hr. To investigate the effect of increasing the S:W ratio at the substrate during growth, the H_2S flow was varied from 3.17 sccm to 6.33 sccm.

To investigate the reported ripening of TMD features under a chalcogen flux [55, 56], select samples were annealed in H_2S immediately following growth. These samples were grown at a substrate temperature of 775 °C using an H_2S flow of 3.17 sccm. H_2S anneal times were varied from 30 min to 60 min and compared to an identically grown sample without the H_2S anneal.

6.1.5 Characterization Methods Used

Scanning electron microscopy was used to analyze film morphology and uniformity across the sample. A detailed discussion of this process has been given in section 3.1.4. Height mode atomic force microscopy (AFM) was by far the most useful tool to this investigation, as it provided feature morphology, including feature height, and nucleation density. A detailed description of how this information is extracted from AFM

images is given in section 5.1.5. An additional presentation of the data extracted from AFM images is given in this chapter (Fig. 6.6(d)). The square root of each feature area is taken, giving a measure of length to represent feature size. Histograms of island size were formed to enable investigation of the island size distribution evolution of samples grown using different conditions. As was observed with the WHC + DES experiments (discussed in section 5.1.5), low film coverage precluded obtaining a measurable signal to noise ratio using Raman and photoluminescence spectroscopy (PL). Acquiring an adequate signal to noise ratio would require acquiring data for unacceptable lengths of time.

We would have liked to obtain compositional information on all of the samples presented here to verify stoichiometry and the absence of contaminants. However, during the time we were investigating the use of H_2S to grow WS_2, the Rutherford backscattering spectrometry (RBS) system was unavailable due to system maintenance. Before the maintenance, we were able to obtain RBS spectra of a few samples grown with H_2S, each of which was confirmed to be stoichiometric WS_2, two S atoms /cm^2 for every W atom /cm^2. Normally, we could obtain compositional information with Auger electron spectroscopy (AES). However, as discussed in chapter 2, a very low sensitivity to W, made full compositional analysis with AES impossible. Therefore AES was used on only a few samples, primarily to ensure the absence of contaminants, such as Si, see the discussion in section 6.1.3.

6.2 Results and Discussion

First, we investigated how growth temperature effected film morphology. We grew WS_2 films at substrate temperatures of 663 °C, 705 °C and 730 °C. These growths

were performed with the parameters outlined above, see section 6.1.4, with an H_2S flow of 3.17 sccm. Similar to the observations made in chapters 4 and 5, see Figs. 4.11 and 5.3, increasing the substrate temperature was found to decrease the nucleation density, from 6.29 x 10^{10} cm^{-2} at a substrate temperature of 663 °C to 2.16 x 10^{10} cm^{-2} at 730 °C. Height mode AFM images of these samples are given in Fig. 6.4(a)-(c) and a plot of nucleation density and feature size as a function of substrate temperature is given in Fig. 6.4(d).

The same investigation into the effect of increasing the substrate temperature using WHC and DES precursors, discussed in chapter 5, showed that this decrease in nucleation density was accompanied by the increased growth of multi-layer features. Using WHC and H_2S, increasing the substrate temperature showed no change in the percentage of single-layer films, each yielding a film where > 90 % of the film is attributable to single-layer growth. The reduction in nucleation density is instead accompanied by an increase in average feature size, from 20.1 nm at 663 °C to 32.1 nm at 730 °C.

Unfortunately, the obvious desire to further increase the feature size by increasing the substrate temperature was precluded by the relatively low melting point, 660 °C, of the Al electrical leads. As discussed above, the proximity of these leads to the hot W heater strip prevented our ability to safely increase the heater temperature above 775 °C. Because of the increase in feature size and decrease in nucleation density without a decrease in the percentage of single-layer growth, the remainder of the growths presented herein were performed at a substrate temperature of 730 °C.

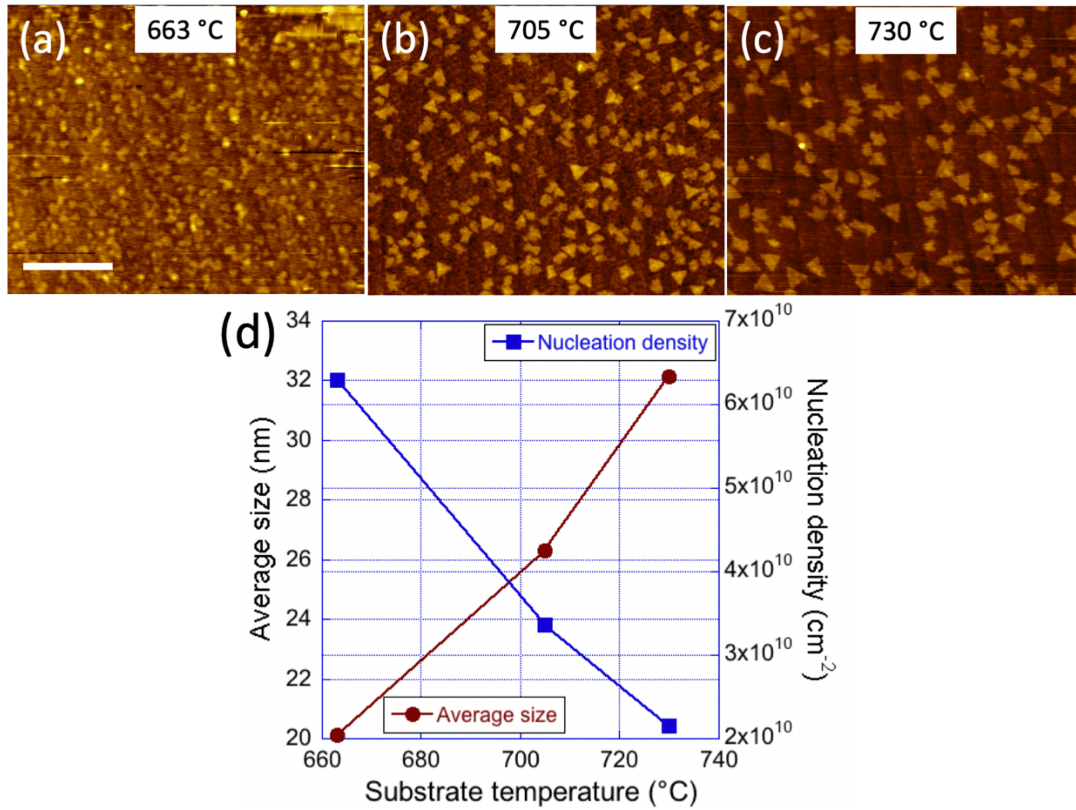

Figure 6.4: (a)-(c) Height mode AFM images of samples grown at different substrate temperatures, (a) 663 °C, (b) 705 °C and (c) 730 °C. The white scalebar in (a) is 250 nm and applies to (a)-(c). (d) Plots the changes in nucleation density and average feature size for the samples in (a)-(c). It shows what is evident in the images, that increasing the substrate temperature decreases the nucleation density while increasing the average feature size.

We then investigated the effect of increasing the H_2S flow at the growth parameters outlined above. Height-mode AFM images from these experiments are given in Fig. 6.5(a)-(b). Similar to the results obtained by increasing the flow of Ar through the DES bubbler, a decrease in nucleation density was observed, from 2.16×10^{10} cm^{-2} at an H_2S flow of 3.17 sccm to 1.08×10^{10} cm^{-2} at 6.33 sccm. This was accompanied by a corresponding increase in feature size from 32.1 nm at 3.17 sccm to 42.3 nm at 6.33 sccm. These results are plotted in Fig. 6.5(c). Fig. 6.5(d) shows the percentage of the covered area attributable to single- (red), double- (blue), triple- (green), quadruple- (black), or many-layer (pink) WS_2 as a function of H_2S flow. This analysis is identical to that used in Figs. 5.2, 5.3 and 5.4, and shows that increasing the H_2S flow also decreases the percentage of the growth attributable to single-layer WS_2 from 91 % at a flow of 3.17 sccm to 68 % at 6.33 sccm. The difference is made up almost exclusively in 2 layer growth, increasing from 2 % to 27 % at 3.17 sccm and 6.33 sccm, respectively.

Our previous speculations led to two hypotheses: that the vertical growth of WS_2 at a higher DES flux occurs because of (1) defects introduced by the carbonaceous DES, and/or (2) because of the presence of catalytic decomposition on the existing WS_2 features. Because these growths were performed without the C-rich DES, this observation provides further evidence for the hypothesis that catalytic decomposition of precursor materials on the existing WS_2 features occurs in this process. However, it must be noted that where the flow of DES and H_2S were both increased by a factor of 2, the reduction in the percentage of single-layer growth was significantly higher in the DES, 71 % to 31 % with DES and 91 % to 68 % with H_2S. Because the increase in percentage of multi-layer

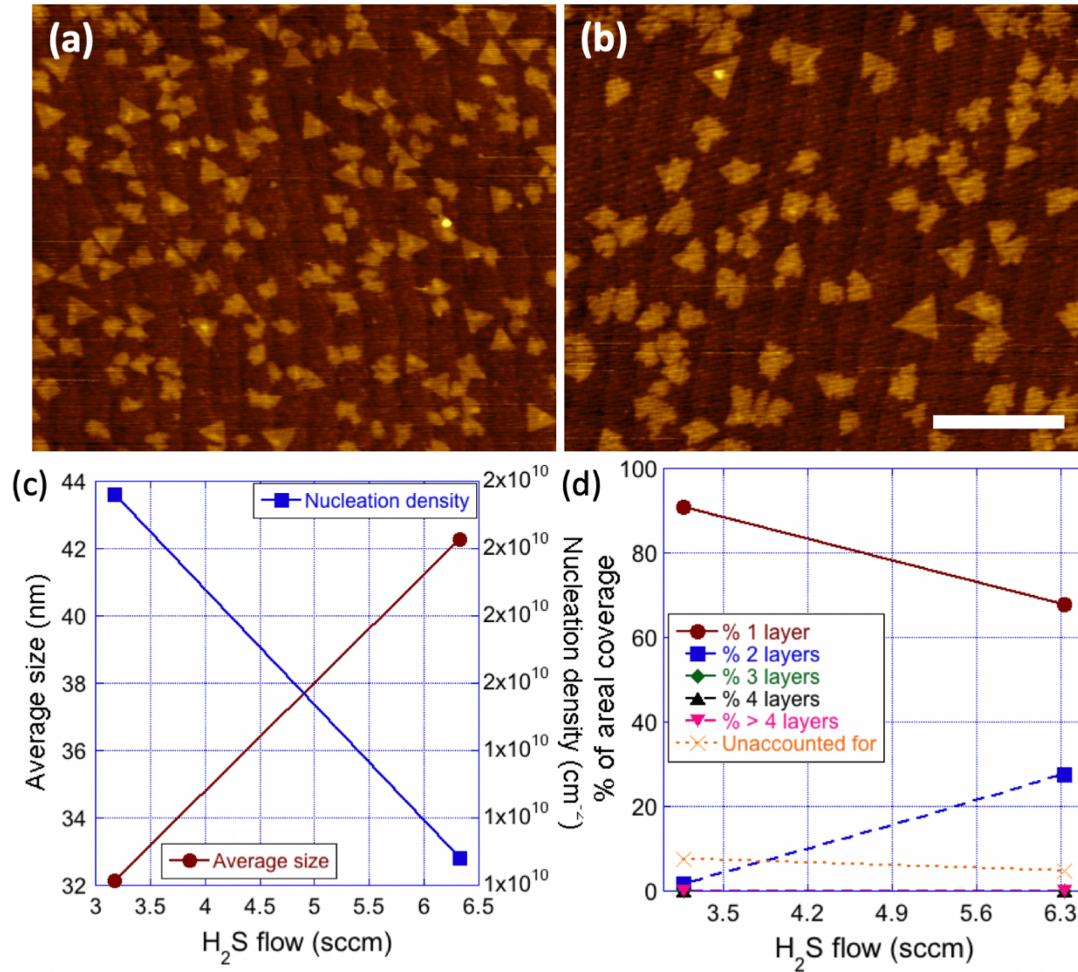

Figure 6.5: (a)-(b) Height mode AFM images of samples grown at different flows of H_2S, (a) 3.17 sccm and (b) 6.33 sccm. The white scalebar in (b) is 250 nm and applies to (a)-(b). (c) Plots the changes in nucleation density and average feature size for the samples in (a)-(b). It shows that increasing the H_2S flow decreases the nucleation density while increasing the average feature size. (d) plots the percent of areal coverage attributable to 1 layer, 2 layer, etc. heights as a function of H_2S flow, showing that increasing the H_2S flow decreases the percent of single layer growth.

growth is detrimental to the aim of this study, an H_2S flow of 3.17 sccm was maintained for the remainder of the project.

Catalytic decomposition may account for the induction of vertical growth, but the reason for the decrease in nucleation density with increased chalcogen flux remained elusive. As discussed in chapter 5, two publications have shown, using cold-wall reactors, that if a TMD film is annealed in a chalcogen flux, after growth, the TMD features "ripen" [55,56]. Evidence of such ripening under a S flux, would indicate that S mobilizes energetic W in existing WS_2 features, offering a plausible explanation for why increasing the S flux decreases the nucleation density of WS_2 features.

At this point it is necessary to introduce Ostwald ripening. Ostwald ripening, referred to herein simply as ripening, is a thermodynamic effect observed in many classes of materials and liquids. Consider an equilateral triangle of side length S, which accurately reflects the crystallinity of WS_2 and is consequently the feature morphology most commonly observed for highly crystalline films. The triangle has a perimeter $P = 3S$, and an area:

$$A = \left(\frac{\sqrt{3}}{2}\right)S^2 \tag{4}$$

If we call the area projected onto the substrate of a WS_2 molecule, a formular unit, σ, then there are:

$$N = \frac{\left(\frac{\sqrt{3}}{2}\right)S^2}{\sigma} \tag{5}$$

formular units in the triangle. We can then define S in terms of N by:

$$S = \alpha N^{1/2} \quad (6)$$

where:

$$\alpha = \left(\frac{2\sigma}{\sqrt{3}}\right)^{1/2} \quad (7)$$

We call the edge energy per unit length γ. The chemical potential of a WS_2 formular unit in the condensed phase, in an island, and the chemical potential of a WS_2 formular unit in the dilute phase, diffusing across the substrate, are represented by μ_c and μ_d, respectively. Then a triangle with a side length S has Gibbs free energy:

$$G = N\mu_c + \gamma P = N\mu_c + 3\gamma\alpha N^{1/2} \quad (8)$$

Since the chemical potential is dG/dN, the chemical potential of a WS_2 formular unit in an equilateral triangle of side length S is:

$$\mu = \mu_c + \frac{3}{2}\gamma\alpha N^{-1/2} \quad (9)$$

So the chemical potential of a WS_2 formular unit in a triangular feature decreases as the area of the feature increases. This disparity between the chemical potential of large and small islands drives ripening.

As the flux of WHC to the sample is stopped, the supersaturation, required for nucleation, rapidly drops until it is equal to the chemical potential of WS_2 in the smallest feature. At this point it is more energetically favorable for the WS_2 to go to the larger features. This causes the supersaturation to drop below the chemical potential of WS_2 in the smallest feature. It is then energetically favorable for the small features to dissolve and contribute their material to the 'free concentration' of WS_2 diffusing on the substrate. As the anneal progresses, these diffusing materials settle on existing features, further

reducing the supsersaturation and increasing the minimum feature size that can maintain equilibrium with the supersaturation. This is Ostwald ripening [126-128]. Features above the equilibrium size grow larger and features below it continue to dissolve contributing the growth of the larger features.

The investigation of ripening was conducted by growing WS_2 samples at a substrate temperature of 730 °C and an H_2S flow of 3.17 sccm. Immediately after termination of Ar flow through the WHC bubbler, the samples were annealed in H_2S for 30 min and 60 min. The Ar, H_2 and H_2S flows were maintained at the values used for growth of the WS_2 film. Results from this investigation were compared to an identically grown WS_2 film without annealing in H_2S and are given in Fig. 6.6. Figs. 6.6(a)-(c) are height mode AFM images for samples grown for 4 hours before annealing under an H_2S flux for (a) 0 min, (b) 30 min and (c) 60 min.

Immediately apparent from the figures is an increase in average feature size, coupled with a decrease in the areal density of features and an increase in the triangularity of the features with increased ripening times. Note that we can no longer refer to 'nucleation density', because the areal density of features no longer reflects the density of WS_2 islands that formed during growth. Fig. 6.6(d) shows island size distributions for (a)-(c). The red curve, for 0 min ripening, shows a broad distribution of island sizes centered around 32 nm. Increasing the ripening time to 30 min, blue curve, shows a splitting of the broad 0 min curve into two peaks, the tallest one centered around 15 nm and the shorter one centered at 50 nm. Further increase in the ripening time shows further shrinking of the small islands to ~ 10nm and an increase in the number of ~50 nm islands. This evolution of the size distribution with H_2S annealing shows in essence that

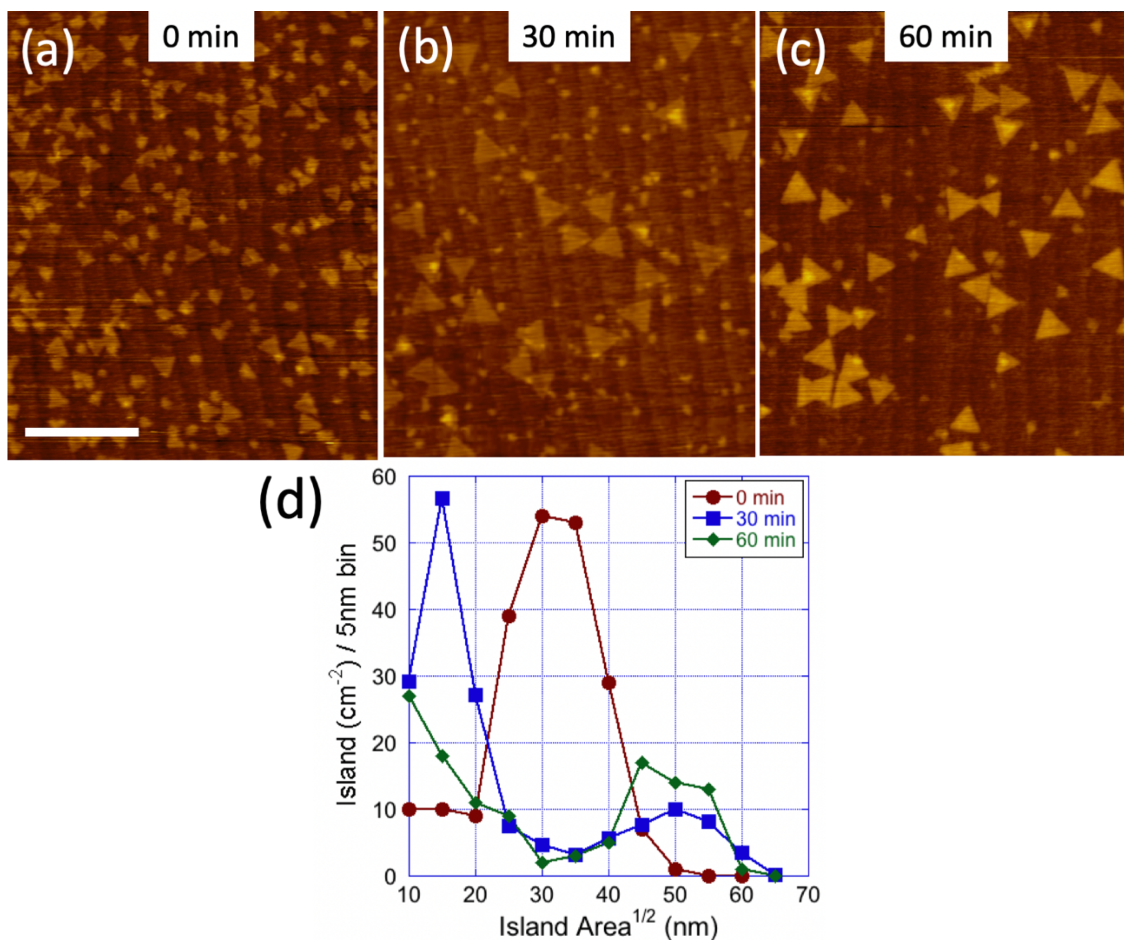

Figure 6.6: (a)-(c) Height mode AFM images of identically grown samples ripened under H_2S + H_2 + Ar for (a) 0 min, (b) 30 min and (c) 60 min. The white scalebar in (a) is 250 nm and applies to (a)-(c). (d) is a plot of size distributions for the 0 min, 30 min and 60 min ripening times. It shows that the broad peak, centered around 32 nm, in the 0 min curve, is split to a bimodal distribution of small and large features after ripening for 30 min. The separation between these two peaks is separated even further by the shrinking of the small features after ripening for 60 min.

as the H_2S anneal time increases, small islands get smaller and less numerous, while other islands form highly triangular features ~ 50 nm in size. Less obvious from Fig. 6.6(d) is the decrease in areal density of features from 2.16 x 10^{10} cm^{-2}, with no H_2S anneal, to 1.65 x 10^{10} cm^{-2}, after a 30 min anneal, to 1.36 x 10^{10} cm^{-2}, after a 60 min H_2S anneal. These observations agree with the description of ripening given above. Note that we can only conclude that Ostwald Ripening is operative if the total volume of WS_2 is conserved during the anneal. AFM image analysis suggests that it is, but verification with a compositional analysis tool, such as RBS, is necessary before the involvement of Ostwald ripening can be determined.

Furthermore, the observation that the WS_2 islands become more triangular as the anneal progresses should be discussed, Fig. 6.6(a), (b) and (c). This likely occurs because the rate at which adatoms arrive at the feature edges during growth is faster than the surface diffusion along the edges of the features. This can 'trap' atoms at the edges, resulting in rough feature perimeters. Under the anneal, there is no longer an 'external' supply of atoms to the substrate, so the rate at which atoms arrive at the feature edges decreases. This slowing of the arrival of adatoms allows each newly arrived atom to 'find its place', resulting in features that reflect the crystallinity of the material. This is indicates that slowing the flux of WHC to the sample, by either decreasing the temperature of the WHC or by diluting the delivered gas with Ar, would also increase the triangularity of the features.

To verify that we were still getting acceptable uniformity, SEM images were acquired every 1 mm across the central 6 mm of the sample shown in Fig. 6.6(a), grown at a substrate temperature of 730 °C and not annealed in H_2S. The nucleation density and

average size analysis employed in chapter 3 was performed on each of the images. Five of the seven SEM images used are shown in Fig. 6.7(a). Directly below in Fig. 6.7(b) is a plot of nucleation density and average feature as a function of distance along the sample. It is worth noting here that our new heater design allows for samples with an exposed length of 8 mm, considerably smaller than the 20 mm of exposed growth surface for past heating schemes. Despite this, 6.7(b) shows uniformity across the central 5 mm of the growth surface. Unlike the corresponding result in chapter 3, where we speculated that the curves in Fig. 3.11 were a result of the combination of temperature variations along the substrate and the varying distance along the sample from the MoO_3 source basket, we are forced to conclude that the curve in Fig. 6.7(b) is a result of temperature variation along the sample only.

Repeatability using this growth method, with these sources, was tested as was done in each of the previous chapters. The same growth was performed identically three separate times, identical to and including the one shown in Fig. 6.4(c). The samples were analyzed and the average feature size, coverage and nucleation density are given in Table 6.1. This data shows high run-to-run repeatability in coverage, 0.23 ± 0.009 ML, while also demonstrating run-to-run repeatability in both average feature size, 28.8 ± 2.6 nm, and nucleation density, $2.64 \pm 0.35 \times 10^{10}$ cm^{-2}.

6.3 Conclusion

The co-deposition of WHC and H_2S was demonstrated to be a viable method of growing WS_2 thin-films on Al_2O_3 in a cold-wall reactor. Using this growth method, it was verified that increasing the substrate temperature has the effect of decreasing the nucleation density. Unlike what was observed with DES, however, this decrease in

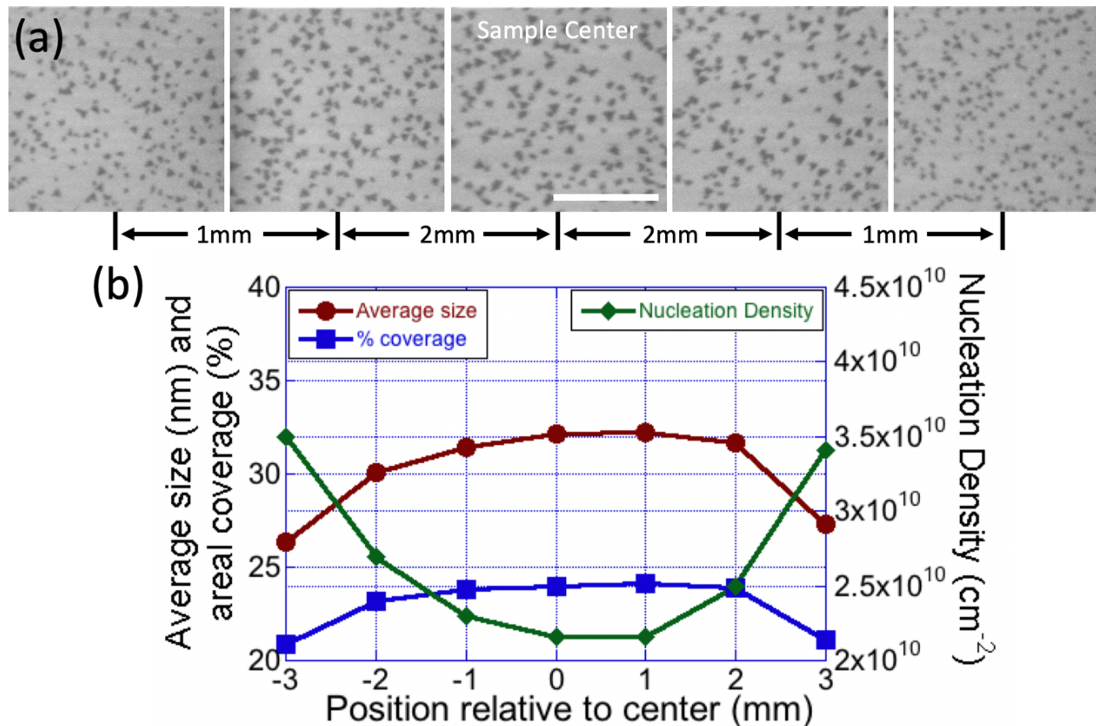

Figure 6.7: (a) SEM images acquired at the indicated positions relative to the center of a WS_2 sample. The white scalebar on the "sample center" image is 500 nm and applies to all. (b) plots feature density, average size and the fractional coverage of WS_2 nanocrystals. The fractional coverage of WS_2 nanocrystals, average feature size and nucleation density were determined from SEM images similar to those shown in (a).

Coverage (ML)	Avg. size (nm)	Density (cm^{-2})
0.24	32.1	2.16×10^{10}
0.22	25.7	3.00×10^{10}
0.24	28.7	2.75×10^{10}
0.23 ± 0.009	28.8 ± 2.6	$2.64 \pm 0.35 \times 10^{10}$

Table 6.1: Summary of the monolayer coverage, measured by AFM at the center of the substrate, with average WS_2 nanocrystal size and nucleation density. The nanocrystal sizes are the square roots of the areas covered by those of the features in the AFM images. At least 200 nanocrystals were involved in the statistical analysis of each sample.

nucleation density was not accompanied by an increase in multi-layer growth. Instead, increasing the substrate temperature increased the feature size without any increase in multi-layer growth. This method was further used to demonstrate that increasing the flux of H_2S to the sample has a similar effect to increasing the flow of DES to the sample: nucleation density decreases, average feature size increases and percentage of multi-layer growth increases.

It was also demonstrated that annealing the samples in H_2S causes a change in the size distribution of WS_2 islands on the substrate, providing evidence for the presence of Ostwald ripening.. This demonstration agrees with current literature and produced features of unmistakably triangular morphology. Run-to-run repeatability and uniformity across large areas of the sample, reported in previous chapters, were demonstrated to be maintained with the substitution of H_2S for DES.

Though this method was able to produce interesting results, it was limited by the use of the low melting point Al electrical leads. The evidence that increasing the temperature increases feature size, while decreasing nucleation density, indicates that larger area crystals would be attainable at higher substrate temperatures. Replacement of these electrical leads with machined refractory metal substitutes would allow for higher temperatures to be investigated, but would likely need frequent adjustments and replacements as the metal formed sulfides. A less economical option would be to use relatively inert, low resistivity Au. The high cost of pure Au leads could be mitigated electrodepositing Au on Cu leads.

An additional limitation to this method was the frequent need to change the W heater strip in our heater. Of further hinderance was the discovery that the first growth with a W strip was inconsistent with subsequent growths. Changing heater strips after every five growths, while needing to 'pre-sulfurize' the W heater strip before use in a growth is inefficient. Apparently, our design efforts to minimize the exposure of the hot W to the sulfurous environment were inadequate to prevent the sulfurization of the W strip. This problem could be avoided, or minimized, by better insulating the W from the hot sulfurous environment. Application of alumina to the strip, or, again, by electrodepositing Au on the strip, could provide the necessary barrier between the hot W and the sulfurous ambient. The benefit to Au would be that the whole strip could be coated without the need to leave exposed areas of W for electrical contact with the Ta electrodes. Additionally, the malleability of Au would likely allow for better thermal contact with the Al_2O_3 substrate than the alumina.

CHAPTER 7

CONCLUSIONS AND FUTURE WORK

Growth of the transition metal dichalcogenide (TMDs) molybdenum disulfide, MoS_2, was investigated using a home-built cold-wall chemical vapor deposition (CVD) reactor capable of independent control over the growth parameters. The growth system was designed as an analog to the majority of the hot-wall CVD work currently being done, with the following improvements: the reaction chamber was assembled using ultra-high vacuum (UHV) components to facilitate quick evacuation of the chamber to pressures in the 10^{-6} Torr range, the reactor utilized a more industry-relevant cold-wall configuration and each of the growth parameters was independently controllable to isolate growth trends resulting from changing each parameter. In this method, molybdenum trioxide, MoO_3, and S were evaporated from alumina coated W baskets and transported by a carrier gas, Ar, to a hot SiO_2/Si substrate. The growth method was demonstrated to have repeatability in coverage and uniformity far superior to the majority of the published work using hot-walled reactors. Using this growth method and chamber configuration, growth of single-layer MoS_2 crystals was demonstrated, as was the effect of varying the growth pressure and the flux of MoO_3 to the growth surface.

Though films grown by evaporating MoO_3 and S from alumina coated W baskets yielded excellent uniformity, uniform across the central 1 cm of the sample, and run-to-run repeatability in coverage, 0.30 ± 0.03 ML as determined by Rutherford backscattering spectrometry (RBS), progress with that method was hindered by a lack of run-to-run repeatability in crystal morphology. The high consistency in coverage coupled with the assumption that S will not stick to a hot substrate without the presence of

transition metal atoms indicated that inconsistencies were not a result of MoO_3 evaporation, but a result of variation in the evaporation of the highly volatile chalcogen source, S. It was therefore decided to switch from elemental S as a chalcogen precursor to diethyl sulfide (DES), $C_4H_{10}S$.

To include DES as a S precursor a custom bubbler system was designed and fabricated. Though not a true bubbler, as commonly used in (CVD), our design was similar in many respects and is thus referred to as a "bubbler". The bubbler system housed the DES and was equipped with two separate gas pathways for the Ar carrier gas: (1) a bypass pathway that allowed the flow of Ar directly into the chamber, bypassing the DES bubbler and (2) a pathway that forced the Ar through the DES bubbler, carrying the Ar vapor to the hot substrate. Initial growths were done flowing Ar through the DES bubbler while simultaneously evaporating MoO_3 from an alumina coated W basket. Little progress was made with these initial DES + MoO_3 experiments because the DES was found to irreversibly contaminate the MoO_3 basket. It was thus decided to switch to an Ar transported Mo source that would utilize our bubbler design. Molybdenum hexacarbonyl (MHC), $Mo(CO)_6$, was selected as a viable Mo precursor.

An additional bubbler system was added to the chamber to house the MHC and deliver its vapor to the substrate. Simultaneous with the switch to MHC, it was decided to switch to an Al_2O_3 growth substrate, for its robustness at high temperatures and the ease by which an atomically flat surface is obtained. Heating Al_2O_3 required the development of a heating system, which utilized a resistively heated Si strip Sn bonded to the underside of the Al_2O_3 substrate, similar to the common practice of In bonding in molecular beam epitaxy (MBE). This method of heating the Al_2O_3 met with great success

until the introduction of hydrogen sulfide, H_2S, as a S precursor, discussed below. Additional changes to the growth scheme included the addition of independently controlled ultra-high purity (UHP) Ar and H_2 lines. The Ar was included to allow the dilution of the precursor-rich gas mixture and the H_2 was added as a means of removing C from the growth surface, a practice commonly employed in metal-organic CVD (MOCVD). Because of the large number of valves and MFCs that required simultaneous manipulation, a LabVIEW program was written to provide control over the Ar flow directions (bypassing and passing through the bubblers) and over all the flow values. It was also necessary to design and fabricate a number of custom electronic parts to facilitate communication between the LabVIEW program and the MFCs and pneumatic valves.

Because of the relatively high vapor pressure of MHC and DES, it was necessary to cool the precursors during growth. At this stage in the project, this was done by submerging the bubblers in liquid/solid "slurry" cold-baths of a solution, with a freezing point equal to the desired temperature. The solution was cooled throughout the growth using small, $< 1\ cm^3$, chunks of dry ice. Variation in the temperature of the slurry bath during growth, and the difficulty in obtaining the same temperature between growths to a high enough precision led to poor repeatability between growths and an inability to identify the effect of varying growth parameters with any degree of confidence. One trend that was consistent throughout the MHC + DES MoS_2 growths was that increasing the substrate temperature significantly reduced the feature size, but induced multi-layer growth, an effect that would be confirmed through the remainder of the project.

To circumvent the need to employ the unreliable slurry cold-baths, it was decided to switch to liquid cold-bath chillers that provide a consistency in temperature to ± 0.1 °C. The commercially available chillers at our disposal were unable to achieve the low temperatures, -45 °C, determined necessary to slowly deposit Mo on the substrate. Therefore, a thermoelectric cooled liquid cold-bath chiller was designed, fabricated and tested (appendix A). The custom thermoelectric cooled chiller was also unable to reach the -45 °C target, so it was decided to switch transition metal sources to tungsten hexacarbonyl (WHC), $W(CO)_6$, which has a lower vapor pressure than MHC.

To effect this change, the MHC bubbler was replaced with a new one for the WHC. WHC + DES experiments growing a different TMD, tungsten disulfide, WS_2, commenced. This combination of precursors in our custom, cold-wall reactor was used to demonstrate the effect of varying a number of growth parameters on the resulting film morphology and feature density. First, increasing the independent, "main", flow of Ar through the chamber was demonstrated to dilute the gas mixture at the substrate. This had the effect of significantly reducing the coverage from 5.25 % of the imaged area being covered by WS_2 features at 2770 sccm to 2.92 % at 4725 sccm. This dilution of the precursor/gas mixture reduced the nucleation density in the growth films from 8.0×10^9 cm^{-2} to 1.08×10^{10} cm^{-2}, at 2770 sccm and 4725 sccm respectively. An analysis of the film, determining the percentage of the film attributable to single-, double-, triple-, quadruple- and many-layer growths indicated that the increase in main Ar flow increased the percentage of the film that was single-layer.

As was observed with MHC + DES growth of MoS_2, increasing the substrate temperature with WHC and DES also decreased the nucleation density from 1×10^{10} cm^{-2}

at a substrate temperature of 545 °C to 3.6 x 10^7 cm^{-2} at 585 °C. This significant decrease demonstrates the significance of the role diffusion of adatoms on the surface plays in the nucleation of TMD features. However, this decrease was accompanied by an increase in vertical growth. Films grown at 545 °C were measured to be 54 % single-layer, while films grown at 585 °C were only 19 % single-layer.

Similar trends were observed when varying the flow of Ar through the DES bubbler. Nucleation density decreased from 1.08 x 10^{10} cm^{-2} at 27.0 sccm to 3.40 x 10^9 cm^{-2} at 41.6 sccm, down to 7.44 x 10^8 cm^{-2} at 60.1 sccm, while the % of single-layer area decreased from 71 % to 46 % to 31 % over the same flows. The increase in multi-layer growth when increasing the substrate temperature and the flow through the DES bubbler is suspected to indicate the presence of catalytic decomposition on top of existing WS_2 features. Hot-wall CVD studies reporting the effect of increased S flux to the growth surface have observed an increase in nucleation density with S flux and report no multi-layer growth [39,123]. This is likely because in a hot-wall reactor, precursor decomposition is dominated by thermal decomposition, which can happen anywhere in the hot furnace. In our cold-wall reactor, precursor decomposition is limited to the growth surface, where both thermal and catalytic decomposition are in competition.

Another reported phenomenon is that placing salt upstream from the TMD growth surface drastically lowers nucleation density and increases feature size [39-40,122]. NaCl has been reported to be the best to achieve this [39]. Our reactor was modified to investigate this phenomenon by including a 4" long by 1.3" diameter cylindrical mesh tube filled with NaCl to the gas inlet. Though many experiments were conducted to

observe the reported results, it was concluded that the addition of NaCl to our reactor made no difference to the final film morphology.

Finally, the growth of WS_2 using the vapor transport of WHC and DES was concluded by demonstrating the improvement in run-to-run repeatability over our previous growth method of co-depositing MoO_3 and S on SiO_2/Si. Unlike the MoO_3 + S growths, which gave run-to-run repeatability in coverage, but not morphology, the use of transporting WHC and DES vapors to grow WS_2 yielded exceptional repeatability in both coverage, 0.056 ± 0.007 ML, and morphology (average feature size, 44.3 ± 3.1 nm, and nucleation density, $3.05 \pm 0.7 \times 10^9$ cm^{-2}). In spite of this high level of repeatability, progress was hampered by the inability to push growth parameters to produce features large enough for analysis, without inducing multi-layer growth. A couple of articles in the literature indicate that hydrogen sulfide, H_2S, is a far better source of S than DES. The claim is that this is because of the lack of spurious carbon in H_2S [56,123]. It was decided to investigate this in hopes of overcoming the limitations seen in the WHC + DES growths.

H_2S is a highly flammable, highly toxic gas at room temperature and special care was taken to customize the reaction chamber to safely employ it as a S precursor. H_2S was added to the reaction chamber, replacing the DES bubbler system described above, and experimentation with H_2S + WHC to grow WS_2 began. Initial growths using this combination of precursors were performed using the Al_2O_3 heating scheme described above, however RBS showed that Si was migrating the growth surface. Careful experimentation was done to determine that the hot Si heating strip in the presence of

H_2S was the source of Si. Having determined this, it was necessary to develop a new way to heat the Al_2O_3.

A custom heater was designed that clamped the Al_2O_3 substrate to a resistively heated W heater strip. Because of the propensity of sulfur to sulfurize anything it can, the heater was designed to minimize exposure of the hot W strip to the sulfurous ambient. This was done by sandwiching the W strip between a pyrolytic boron nitride (PBN) bottom plate and the sample. Though this heater had its limitations, discussed below, it was found to eliminate Si from the growth surface and was used to further our understanding of the growth mechanisms of WS_2 on Al_2O_3. It is noteworthy that at this point, a Eurotherm temperature controller in communication with the infrared pyrometer and a "slaved" power supply was added to control the substrate temperature.

Using this combination of precursors in conjunction with the modifications to the reactor and its hardware, the effect of increasing substrate temperature was once again demonstrated. With these precursors, it was shown that increasing the substrate temperature decreased the nucleation density, from 6.29×10^{10} cm^{-2} at a substrate temperature of 663 °C to 2.16×10^{10} cm^{-2} at 730 °C. This effect was accompanied by an increase in average feature size from 20.1 nm at 663 °C to 32.1 nm at 730 °C. No induction of multi-layer growth at higher substrate temperatures was observed. The desire to increase the substrate temperature further was quelled by the low melting point, 660 °C, of the Al electrodes used to provide a DC current to the sample heater.

H_2S and WHC were further used to investigate the effect of increased flux of S to the growth surface. This was done by increasing the flow of H_2S into the reactor. Similar to the results increasing the flow of Ar through the DES bubbler, a decrease in nucleation

density was observed, from 2.16 x 10^{10} cm^{-2} at an H_2S flow of 3.17 sccm to 1.08 x 10^{10} cm^{-2} at 6.33 sccm. This was accompanied by a corresponding increase in feature size from 32.1 nm at 3.17 sccm to 42.28 nm at 6.33 sccm. Analysis of this series of experiments further showed that increasing the flow of H_2S also decreases the percentage of the growth attributable to single-layer WS_2 from 91 % at a flow of 3.17 sccm to 68 % at 6.33 sccm. The difference is made up almost exclusively in 2 layer growth, increasing from 2 % to 27 % at 3.17 sccm and 6.33 sccm, respectively.

To investigate the reason behind the increase in feature size and the decrease in nucleation density with an increased flow of H_2S, after growth a series of samples were annealed in a flow of Ar + H_2 + H_2S for 0 min, 30 min and 60 min. The effect of this post-growth anneal in H_2S was demonstrated by size distribution plots for the 3 samples. Ripening of the existing WS_2 features is evident in these distributions by the splitting of the broad distribution of feature sizes at 0 min into two separate peaks in the distribution at 30 min and 60 min. The peak representative of the larger features, ~ 60 % larger than the average feature size in the 0 min distribution, increases in count from 30 min to 60 min, while the peak representative of the smaller features, ~ 50 % the size of the average feature size in the 0 min distribution, continues to decrease in size from 30 min to 60 min, while also decreasing in count. In essence, the larger features increase to a thermodynamically stable size, ~ 50 nm for the growth parameters used, while the small features get smaller and less numerous. This is evidence for the ripening of WS_2 features under a flux of H_2S.

The experiments using H_2S + WHC to grow WS_2 films was concluded by the demonstration that the new method of growth did not hinder the film uniformity across

the sample, nor the run-to-run repeatability in terms of both coverage and morphology. Films were demonstrated to be uniform across the central 60 % of the 8 mm sample, compared to the 50 % of the 20 mm sample grown using MoO_3 and S. A high run-to-run repeatability in coverage, 0.23 ± 0.009 ML, was demonstrated, while also demonstrating run-to-run repeatability in both average feature size, 28.83 ± 2.6 nm, and feature density, $2.64 \pm 0.35 \times 10^{10}$ cm^{-2}.

S was the main hinderance in every step of this project. It seems a bit Midas-esque to suggest that everything be coated in Au, but an inert barrier between the sulfurous environment and the components of the heater would minimize various limitations in the growth process. The W heater strip, for example, where perfectly viable for obtaining good data, was found to sulfurize and deform after approximately five growths of 4 hr each. The sulfurization caused a fine grey powder, presumably WS_2, to cover the W heater strip, coat the top of the PBN bottom plate and rub off on the bottom of the Al_2O_3 substrate. The deformation applied uneven pressure to the Al_2O_3 causing it to break mid-growth. Mid-growth breakage yielded a bimodal growth distribution indicative of growth at two temperatures, signifying that thermal contact between the W and the Al_2O_3 was changed during the growth. These samples were discarded. The sulfurization of the W also caused a change in the thermal contact between the W heater strip and the Al_2O_3 after approximately 1 hr after the first growth with a new W heater strip was initiated. This was observed by an increase in the power needed to maintain the Eurotherm controlled heater temperature, 111 W to 130 W, and a bimodal distribution of feature sizes, again indicative of changing thermal contact. Therefore, the first growth

with each new heater strip was discarded, significantly limiting the efficiency of data acquisition.

This could be mitigated or eliminated by electrodepositing Au onto the W heater stirp. Au has a high melting point, low resistivity and is essentially inert. A more cost-conscious alternative would be coating the W heater strip in alumina, in the same way alumina coated W baskets are. A drawback to this over Au is that the hardness and porosity of alumina might yield poor thermal contact between the alumina coating and the sapphire substrate. Additionally, alumina is not electrically conductive necessitating portions of the W to be exposed for electrical contact to the Ta electrodes, subjecting them to potential sulfurization. Other possibilities include attempting growth on other substrates. Highly-oriented pyrolytic graphite is a good choice as it can be resistively heated and should be inert to the sulfurous environment.

The Al electrical leads (discussed in section 6.1.3), used to replace the phosphor bronze leads employed early this project, limited the maximum substrate temperature that could be grown on. As discussed above, growth trends indicated that using H_2S and WHC, nucleation density could be decreased, while increasing feature size, without reducing the percentage of single layer film. The low melting point of Al, 660 °C, precluded increasing the heater temperature above 775 °C. Replacing these electrical leads with a higher melting-point material, such as W or Ta, would eliminate this limitation. However, as has been observed throughout, even these high-temperature refractory metals are vulnerable to sulfurization. Where it is possible that the temperatures of the electrical leads are not high enough for sulfurization to occur, use of a more resistant material would eliminate the concern. Electrodepositing Au on refractory

metal, or even Cu, electrodes is a possible way to eliminate the limitation imposed by the low melting point of the Al electrical leads, without introducing a new sulfurization limitation.

It is believed that with these minor, if expensive, modifications to the heater system, a wider range of temperatures could be investigated. Beyond modifications to the heater, cooling the WHC to lower temperatures would reduce the flux of WHC to the sample, eliminating the need to accomplish this by diluting the precursor vapors with an Ar flow of 4725 sccm. This would allow for longer growths yielding larger area films with a lower density, without exhausting the available Ar supply. As discussed in chapter 6, slowing the growth in this way would likely increase the triangularity of the WS_2 features.

Future work should include these changes, or at least adapt to these inevitable limitations. Some elements in the understanding of the growth mechanisms behind TMD growth remain and should be investigated by a careful set of experiments investigating the dependence of growth time on the films. This investigation would determine if increasing the growth time of a given set of growth parameters simply increases the size of the features, or if, by some thermodynamic equilibrium, akin to the mechanism behind ripening, features reach a stable size under a set of growth parameters and prolonged exposure merely increases the number of those features. Some of our experiments, not presented herein, suggest that the latter might be the case.

Another interesting phenomenon that future work should investigate is the ripening of samples. As stated in chapter 6, it is still not clear if the rearrangement of WS_2 on the surface can be fully attributed to Ostwald ripening. Compositional analysis is

needed to verify this. However, it was clear from the samples grown that not only do the islands grow under "ripening", but that islands annealed in H_2S more accurately reflect the crystallinity of the material, i.e. they are, on average, discernably more triangular than un-annealed islands. Future work should include transmission electron microscopy (TEM) or x-ray diffraction on these samples to see if the crystallinity of H_2S annealed films is higher than in their un-annealed counterparts.

It would also be informative to determine if one chalcogen precursor, hydrogen selenide, for example, can be used to "ripen" a film with a different chalcogen, such as WS_2. If it can, it would be interesting to do obtain TEM of the sample to determine if the chalcogen is being replaced, and if so where it's being replaced. Not only would this provide valuable information about the ripening process and the mobility of transition metal / chalcogen moieties along the substrate, but it would indicate whether or not ripening can be used as a procedural step in the synthesis of chalcogenide heterostructures, such as WS_xSe_{2-x}. If chalcogen substitution happens throughout the crystal, then care will be need to be taken synthesizing such heterostructures. More likely, it is the edge states that are under threat of substitution and relocation. If that's the case, ripening may prove a facile method of growing lateral, in-plane, heterostructures, in this example: WS_xWSe_{2-x}. A similar set of experiments on an alloyed film, i.e. $Mo_xW_{1-x}S_2$, would be interesting as well.

Beyond a deeper investigation of ripening, future work should begin to vigorously explore the ability of the methods presented herein to grow lateral, in-plane, and vertical, out-of-plane, heterostructures of TMD materials. With the growth mechanisms determined and the "recipes" for growths of a prescribed feature size and island density

on hand, growing heterostructures should prove facile. If not, interesting features will be interpretable by the different optical properties of the materials involved, or by high resolution microscopy. Raman and photoluminescence (PL) mapping can be used to quickly and easily locate the distinct materials in the films. For higher resolution pinpointing, TEM would be ideal. Alloy growth, meaning the simultaneous supplying of WHC, MHC and H_2S, for instance, should also be explored. Where such synthesis is expected to be predictable under the highly controlled growths outlined in this dissertation, it would be informative and necessary to the careful cataloguing of the available TMD properties.

From the onset of this project, a reactor capable of staggered or simultaneous deposition of Mo, W, S and Se precursors was envisioned. The challenges inherent to this project prevented our getting there. Instead, a great deal of time and effort was spent developing a growth method that would allow such a four- source, or more, reactor to be used to great effect. Future work should continue to that end, take what has been detailed herein and begin to explore the vast possibilities available when combinations of these materials are used.

REFERENCES

[1] M. M. Waldrop, *Nature* **530**, 144 (2016).

[2] K. S. Novoselov, A. K. Geim, S. V. Morozov, D. Jiang, Y. Zhang, S. V. Dubonos, I. V. Grigorieva, and A. A. Firsov, *Science* **306**, 666 (2004).

[3] G. Cassabois, P. Valvin, and B. Gil, *Nature Photon.* **10**, 262 (2016).

[4] W. Zhang, J. Huang, C. Chen, Y. Chang, Y. Cheng, and L. Li, *Adv. Mater.* **25**, 3456 (2013).

[5] A. Splendiani, L. Sun, Y. Zhang, T. Li, J. Kim, C. Chim, G. Galli, and F. Wang, *Nano Lett.* **10**, 1271 (2010).

[6] K. F. Mak, C. Lee, J. Hone, J. Shan, and T. F. Heinz, *Phys. Rev. Lett.* **105**, 136805 (2010).

[7] N. Peimyoo, W. Yang, J. Shang, X. Shang, Y. Wang, and T. Yu, ACS Nano 8(11), 11320 (2014).

[8] K. Cho, J. Yang, and Y. Lu, *J. Mater. Res.* **32**(15), 2839 (2017).

[9] S. Helveg, J. V. Lauritsen, E. Lægsgaard, I. Stensgaard, J. K. Nørskov, B. S. Clausen, H. Topsøe, and F. Besenbacher, *Phys. Rev. Lett.* **84**(5), 951 (2000).

[10] T. W. Hickmott, *J. Appl. Phys.* **37**(4), 1928 (1966).

[11] M. Chhowalla, H. S. Shin, G. Eda, L. Li, K. P. Loh, and H. Zhang, *Nat. Chem.* **5**, 263 (2013).

[12] J. Kang, S. Tongay, J. Li, and J. Wu, *J. Appl. Phys.* **113**, 143703 (2013).

[13] R. J. Wu, M. L. Odlyzko, K. A. Mkhoyan, *Ultramicroscopy* **147**, 8 (2014).

[14] Y. Zhan, Z. Liu, S. Najmaei, P. M. Ajayan, and J. Lou, *Small* **8**(7), 966 (2012).

[15] D. Xiao, G. Liu, W. Feng, X. Xu, and W. Yao, *Phys. Rev. Lett.* **108**, 196802 (2012).

[16] T. Cao, G. Wang, W. Han, H. Ye, C. Zhu, J. Shi, Q. Niu, P. Tan, E. Wang, B. Liu, and J. Feng, *Nat. Commun.* **3**, 887 (2012).

[17] J. Wu, H. Li, Z. Yin, H. Li, J. Liu, X. Cao, Q. Zhang, and H. Zhang. *Small* **9**(19), 3314 (2013).

[18] F. Wang, I. A. Kinloch, D. Wolverson, R. Tenne, A. Zak, E. O'Connell, U. Bangert, and R. J. Young, *2D Mater.* **4**, 015007 (2016).

[19] G. Cunningham, M. Lotya, C. S. Cucinotta, S. Sanvito, S. D. Bergin, R. Menzel, M. S. P. Shaffer, and J. N. Coleman, *ACS Nano* **6**(4), 3468 (2012).

[20] A. Gurarslan, Y. Yu, L. Su, Y. Yu, F. Suarez, S. Yao, Y. Zhu, M. Ozturk, Y. Zhang, and L. Cao, *ACS Nano* **8**(11), 11522 (2014).

[21] B. V. Lotsch, *Annu. Rev. Mater. Res.* **45**, 85 (2015).

[22] S. Najmaie, Z. Liu, W. Zhou, X. Zou, G. Shi, S. Lei, B. I. Yakobson, J. Idrobo, P. M. Ajayan, and J. Lou, *Nat. Mater.* **12**, 754 (2013).

[23] Y. Lee, X. Zhang, W. Zhang, M. Chang, C. Lin, K. Chang, Y. Yu, J. T. Wang, C. Chang, L. Li, and T. Lin, *Adv. Mater.* **24**, 2320 (2012).

[24] J. Zhang, H. Yu, W. Chen, X. Tian, D. Liu, M. Cheng, G. Xie, W. Yang, R. Yang, X. Bai, D. Shi, and G. Zhang, *ACS Nano* **8**(6), 6024 (2014).

[25] T. H. Ly, M. Chio, M. Li, J. Zhao, D. J. Perello, M. O. Cichocka, H. M. Oh, S. H. Chae, H. Y. Jeong, F. Yao, L. Li, and Y. H. Lee, *ACS Nano* **8**(11), 11401 (2014).

[26] S. Najmaei, Z. Liu, W. Zhou, X. Zou, G. Shi, S. Lei, B. I. Yakobson, J. Idrobo, P. M. Ajayan, and J. Lou, *Nat. Mater.* **12**, 754 (2013).

[27] R. Ionescu, W. Wang, Y. Chai, Z, Mutlu, I. Ruiz, Z. Favors, D. Wickramaratne, M. Neupane, L. Zavala, R. Lake, M. Ozkan, and C. S. Ozkan, *IEEE Trans. Nanotech.* **13**, 749 (2014).

[28] Y. Li, W. Zhang, J. Huang, K. Liu, Y. Lee, C. Liang, C. Chu, and L. Li, *Nanoscale* **4**, 6637 (2012).

[29] A. Azizi, S. Eichfeld, G. Geschwind, K. Zhang, B. Jiang, D. Mukherjee, L. Hossain, A. F. Piasecki, B. Kabius, J. A. Robinson, and N. Alem, *ACS Nano* **9**, 4882 (2015).

[30] C. J. Docherty, P. Parkinson, H. J. Joyce, M. Chiu, C. Chen, M. Lee, L. Li, L. Herz, M. B. Johnston, *ACS Nano* **8**, 11147 (2014).

[31] T. H. Ly, M. Chiu, M. Li, J. Zhao, D. Perello, M. O. Cichocka, H. M. Oh, S. H. Chae, H. Y. Jeong, F. Yao, L. Li, and Y. H. Lee, *ACS Nano* **8**, 11401 (2014).

[32] W. Wu, D. De, S. Chang, Y. Wang, H. Peng, J. Bao, and S. Pei, *Appl. Phys. Lett.* **102**, 142106 (2013).

[33] A. M. van der Zande, P. Y. Huang, D. A. Chenet, T. C. Berkelbach, Y. You, G. Lee, T. F. Heinz, D. R. Reichman, D. A. Muller, and J. C. Hone, *Nat. Mater.* **12**, 554 (2013).

[34] S. Wang, Y. Rong, Y. Fan, M. Pacios, H. Bhaskaran, and K. He, *Chem. Mater.* **26**(22), 6371-6379 (2014).

[35] K. M. McCreary, A. T. Hanbicki, J. T. Robinson, E. Cobas, J. C. Culbertson, A. L. Friedman, G. G. Jernigan, and B. T. Jonker, *Adv. Funct. Mater.* **24**, 6449 (2014).

[36] Y. Yu, C. Li, Y. Liu, L. Su, Y. Zhang, and L. Cao, *Sci. Rep.* **3**, 1866 (2013).

[37] A. Gurarslan, Y. Yu, L. Su, Y. Yu, F. Suarez, S. Yao, Y. Zhu, M. Ozturk, Y. Zhang, and L. Cao, *ACS Nano* **8**, 11522 (2014).

[38] Y. Yu, C. Li, Y. Liu, L. Su, and L. Cao, *Sci. Rep.* **3**, 1866 (2013).

[39] K. Kang, S. Xie, L. Huang, Y. Han, P. Y. Huang, K. F. Mak, C. Kim, D. Muller, J. Park, *Nature* **520**, 656 (2015).

[40] H. Kim, D. Ovchinnikov, D. Deiana, D. Unuchek, and A. Kis, *Nano Lett.* **17**, 5056 (2017).

[41] A. Tuxen, H. Gøbel, B. Hinnermann, Z. Li, K. G. Knudsen, H. Topsøe, J. V. Lauritsen and F. Besenbacher, *J. Catal.* **281**(2), 345 (2011).

[42] M. Shanmugam, C. A. Durcan, and B. Yu, *Nanoscale* **4**, 7399 (2012).

[43] I. Bilgin, F. Liu, A. Vargas, A. Winchester, M. K. L. Man, M. Upmanyu, K. M. Dani, G. Gupta, S. Talaparta, A. D. Mohite, and S. Kar, *ACS Nano* **9**(9), 8822 (2015).

[44] X. Wang, H. Feng, Y. Wu, and L. Jiao, *J. Am. Chem. Soc.* **135**, 5304 (2013).

[45] Y. Lin, W. Zhang, J. Huang, K. Liu, Y. Lee, C. Liang, C. Chu, and L. Li, *Nanoscale* **4**, 6637 (2012).

[46] K. iu, W. Zhang, Y. Lee, Y. Lin, M. Chang, C. Su, C. Chang, H. Li, Y. Shi, H. Zhang, C. Lai, and L. Li, *Nano Lett.* **12**(3), 1538 (2012).

[47] A. Koma, *Surf. Sci.* **267**, 29 (1992).

[48] S. E. Kazzi, W. Mortelmans, T. Nuytten, J. Meersschut, P. Carolan, L. Landeloos, T. Conrad, I. Radu, M. Heys, and C. Merkling, *J. Appl. Phys.* **123**, 135702 (2018).

[49] M. Nakano, Y. Wang, W. Kashiwabara, H. Matsuoka, and Y. Iwasa, *Nano Lett.* **17**(9), 5595 (2017).

[50] H. C. Diaz, Y. Ma, R. Chaghi, and M. Batzill, *Appl. Phys. Lett.* **108**, 191606 (2016).

[51] B. Groven, A. N. Mehta, H. Bender, J. Meersschaut, T.Nuytten, P. Verdonck, T. Conard, Q. Smets, T. Schram, B. Schoenaers, A. Stesmans, V. Afanas'ev, W. Vandervorst, M. Heyns, M. Caymax, I. Radu, and A. Delabie, *Chem. Mater.* **30**(21), 7648 (2018).

[52] Y. Yu, M. H. Raza, Y. Chen, P. Amsalem, S. Wahl, K. Skrodczky, X. Xu, K. S. Lokare, M. Zukush, P. Gaval, N. Koch, E. A. Quadrelli, and N. Pina, *Chem. Mater.* **31**(6), 1881 (2019).

[53] S. Yeo, D. K. Nandi, R. Rahul, T. H. Kim, B. Shong, Y. Jang, J. Bae, J. W. Han, S. Kim, and H. Kim, *Appl. Surf. Sci.* **459**, 596 (2018).

[54] Y. Huang, L. Liu, and Y. Chen, *Langmuir* **35**(10), 3651 (2019).

[55] X. Zhang, T. H. Choudhury, M. Chubarov, Y. Xiang, B. Jariwala, F. Zhang, N. Alem, G. Wang, J. A. Robinson, and J. M. Redwing, *Nano Lett.* **18**(2), 1049 (2018).

[56] T. H. Choudhury, H. Simchi, R. Boichot, M. Chubarov, S. E. Mohney, and J. M. Redwing, *Cryst. Growth Des.* **18**(8), 4357 (2018).

[57] S. Wang, M. Pacios, H. Bhaskaran, and J. H. Warner, *Nanotechnology* **27**, 085604 (2016).

[58] Z. He, Y. Sheng, Y. Rong, G. Lee, J. Li, and J. H. Warner, *ACS Nano* **9**(3), 2740 (2015).

[59] W. Zhang, J. Huang, C. Chen, Y. Chang, Y. Cheng, and L. Li, *Adv. Mater.* **25**, 3456 (2013).

[60] W. Wu, D. De, S. Chang, Y. Wang, H. Peng, J. Bao, and S. Pei, *Appl. Phys. Lett.* **102**, 142106 (2013).

[61] S. Wu, C. Huang, G. Aivazian, J. S. Ross, D. H. Cobden, and X. Xu, *ACS Nano* **7**(3), 2768 (2013).

[62] B. Li, L. Huang, M. Zhong, N. Huo, Y. Li, S. Yang, C. Fan, J. Yang, W. Hu, Z. Wei, and J. Li, *ACS Nano* **9**(2), 1257 (2015).

[63] K. P. Dhakal, S. Roy, H. Jang, X. Chen, W. S. Yun, H. Kim, J. Lee, J. Kim, and J. Ahn, *Chem. Mater.* **29**(12), 5124 (2017).

[64] J. Mann, Q. Ma, P. M. Odenthal, M. Isarraraz, D. Le, E. Preciado, D. Barroso, K. Yamaguchi, G. von Son Palacio, A. Nguyen, T. Tran, M. Wurch, A. Nguyen, V. Klee, S. Bobek, D. Sun, T. F. Heinz, T. S. Rahman, R. Kawakami, and L. Bartels, Adv. Materi. **26**, 1399 (2014).

[65] Y. Chen, J. Xi, D. O. Dumcenco, Z. Liu, K. Suenaga, D. Wang, Z. Shuai, Y. Huang, and L. Xie, *ACS Nano* **7**(5), 4610 (2013).

[66] Z. Lin, M. T. Thee, A. L. Elias, S. Feng, C. Zhou, K. Fujisawa, N. Perea-Lopez, V. Carozo, H. Terrones, and M. Terrones, *Appl. Mater.* **2**, 092514 (2014).

[67] Y. Gong, S. Lei, G. Ye, B. Li, Y. He, K. Keyshar, X. Zhang, Q. Wang, J. Lou, Z. Liu, R. Vajtai, W. Zhou, and P. M. Ajayan, *Nano Lett.* **15**, 6135 (2015).

[68] S. Xie, L. Tu, Y. Han, L. Huang, K. Kang, K. U. Loa, P. Poddar, C. Park, D. A. Muller, R. A. DiStasio Jr., and J. Park, *Science* **359**, 1131 (2018).

[69] C. H. Naylor, W. M. Parkin, A. Goa, J. Berry, S. Zhou, Q. Zhang, J. B. McClimon, L. Z. Tan, C. E. Kehayias, M. Zhao, R. S, Gona, R. W. Carpick, A. M. Rappe, D. J. Srolovitz, M. Drndic, and A. T. C. Johnson, *ACS Nano* **11**(9), 8619 (2017).

[70] Y. Gong, J. Lin, X. Wang, G. Shi, S. Lei, Z. Lin, X. Zou, G. Ye, R. Vajtai, B. I. yakobson, H. Terrones, M. Terrones, B. K. Tay, J. Lou, S. T. Pantelides, Z. Liu, W. Zhou, and P. M. Ajayan, *Nat. Mater.* **13**, 1135 (2014).

[71] S. Pak, J. Lee, Y. Lee, A. Jang, S. Ahn, K. Y. Ma, Y. Cho, J. Hong, S. Lee, H. Y. Jeong, H. Im, H. S. Shin, S. M. Morris, S. Cha, J. I. Sohn, and J. M. Kim, *Nano Lett.* **17**(9), 5634 (2017).

[72] C. Lunceford and J. Drucker, *J. Vac. Sci. Technol. A* **30**, 061509 (2012).

[73] S. J. Rathi, D. J. Smith, and J. Drucker, *Crystal Growth Des.* **14**(9), 4617 (2014).

[74] S. Das and J. Drucker, *Nanotechnology* **28**, 105601 (2017).

[75] S. J. Rathi, D. J. Smith, and J. Drucker, *Nano Lett.* **13**(8), 3878 (2013).

[76] E. Dailey and J. Drucker, *J. Appl. Phys.* **105**, 064317 (2009).

[77] P. Madras, E. Dailey, and J. Drucker, *Nano Lett.* **10**(5), 1759 (2010).

[78] J. W. Dailey, J. Taraci, T. Clement, D. J. Smith, and J. Drucker, *J. Appl. Phys.* **92**(12), 7556 (2004).

[79] S. Barrett, Image SXM, University of Liverpool, Liverpool, UK, https://www.liverpool.ac.uk/~sdb/ImageSXM/, (2018).

[80] Veeco Instruments Inc., *SPM training notebook*, (2013).

[81] Hitachi Ltd., *Hitachi S-4700 SEM Training and Reference Guide*, (2007).

[82] W. S. Rasband, ImageJ, U. S. National Institutes of Health, Bethesda, Maryland, USA, http://imagej.nih.gov/ij/, (1997-2014).

[83] C. Lunceford, E. Borcean, and J. Drucker, *Cryst. Growth Des.* **16**(2), 988 (2016).

[84] J. Goldstein, D. E. Newbury, P. Echlin, D. C. Joy, C. Fiori, and E. Lifshin, *Scanning Electron Microscopy and X-Ray Microanalysis*, Springer US (1981).

[85] C. Lee, H. Yan, L. E. Brus, T. F. Heinz, J. Hone, S. Ryu, *ACS Nano* **4**, 2695 (2010).

[86] C. Lee, B. G. Jeong, S. J. Yun, Y. H. Lee, S. M. Lee, and M. S. Jeong, *ACS Nano* **12**(10), 9982 (2018).

[87] C. Lee, H. Yan, L. E. Brus, T. F. Heinz, J. Hone, and S. Ryu, *ACS Nano* **4**(5), 2695 (2010).

[88] M. P. Seah and W. A. Dench, *Surf. Interface Anal.* **1**, 2 (1979).

[89] H. Li, Q. Zhang, C. C. R. Yap, B. K. Tay, T. H. T. Edwin, A. Olivier, and D. Baillargeat, *Adv. Funct. Mater.* **22**, 1385 (2012).

[90] W. Li, A. G. Birdwell, M. Amani, R. A. Burke, X. Ling, Y. Lee, X. Liang, L. Peng, C. A. Richter, J. Kong, D. J. Gundlach, and N. V. Nguyen, *Phys. Rev. B* **90**, 195434 (2014).

[91] H. J. Conley, B. Wang, J. I. Ziegler, R. F. Haglund, S. T. Pantelides, and K. I. Bolotin, *Nano Lett.* **13**, 3626 (2013).

[92] Y. Lin, N. Lu, N. Perea-Lopez, J. Li, Z. Lin, X. Peng, C. H. Lee, C. Sun, L. Calderin, P. N. Browning, M. S. Bresnehan, M. J. Kim, T. S. Mayer, M. Terrones, and J. A. Robinson, *ACS Nano* **8**, 3715 (2014).

[93] G. Eda, H. Yamaguchi, D. Voiry, T. Fujita, M. Chen, and M. Chhowalla, *Nano Lett.* **11**, 5111 (2011).

[94] M. Tsai, S. Su, J. Chang, D. Tsai, C. Chen, C. Wu, L. Li, L. Chen, and J. He, *ACS Nano* **8**, 8317 (2014).

[95] E. Fromm, *Metall. Trans. A.* **9A**, 1835 (1978).

[96] J. S. Chickos and W. E. Acree, *J. Phys. Chem. Ref. Data* **32**, 519 (2003).

[97] M. V. Bollinger, J. V. Lauritsen, K. W. Jacobsen, J. K. Norskov, S. Helveg, and F. Besenbacher, *Phys. Rev. Lett.* **87**, 196803 (2001).

[98] G. Du, Y. Zhou, and B. Xu, *Mater. Character.* **61**, 427 (2010).

[99] O. Ostinelli, and C. R. Bolognesi, *Appl. Phys. Exp.* **4**, 085501 (2011).

[100] D. R. Stull, *Ind. Eng. Chem.* **39**(4), 517 (1947).

[101] see https://mdcvacuum.com/DisplayProductContentResp.aspx?d=MDC&wr=US&p=m.f.3.1.1 for sealed-off 7052 Glass-UHV Series, mdcvacuum.com (2018).

[102] T. Ohta, F. Cicoira, P. Doppelt, L. Beitone, and P. Hoffmann, *Chem. Vap. Deposition* **7**(1), 33 (2001).

[103] R. Chellapa and D. Chandra, J. Chem. Thermodynamics **37**, 377 (2005).

[104] see http://www.ni.com/en-us/support/model.usb-6001.html for USB-6001, ni.com (2019).

[105] M. Yoshimoto, T. Maeda, T. Ohnishi, H. Koinuma, O. Ishiyama, M. Shinohara, M. Kubo, R. Miura, and A. Miyamoto, *Appl. Phys. Lett.* **67**(18), 2615 (1995).

[106] T. Yatsui, K. Kuribara, T. Sekitani, T. Someya, and M. Yoshimoto, *J. Phys. D: Appl. Phys.* **49**, 115302 (2016).

[107] Y. Shiratsuchi, M. Yamamoto, and Y. Kamada, *Jpn. J. Appl. Phys.* **41**, 5719 (2002).

[108] J. R. Heffelfinger, M. W. Bench, C. B. Carter, *Surf. Sci.* **370**, L168 (1997).

[109] O. Kurnosikov, L. Pham Van, and J. Coutsy, *Surf. Sci.* **459**, 256 (2000).

[110] S. Curiotto and D. Chatain, *Surf. Sci.* **603**, 2688 (2009).

[111] P. T. Terziyska, K. S. A. Butcher, P. Rafailov, and D. Alexandrov, *Appl. Surf. Sci.* **353**, 103 (2015).

[112] J. A. Venebles, G. D. Spiller, and M. Handbücken, *Rep. Prog. Phys.* **47**, 399 (1984).

[113] J. D. Weeks and G. H. Gilmer, *Adv. Chem. Phys.* **40**,157 (1979).

[114] M. C. Bartlet and J. W. Evans, *Phys. Rev. B* **46**(19), 12675 (1992).

[115] J. W. Evans, P. A. Thiel, and M. C. Bartlet, *Surf. Sci. Rep.* **61**, 1 (2006).

[116] J. A. Stroscio and D. T. Pierce, *Phys. Rev. B* **49**(12), 8522 (1993).

[117] K. Suenaga, H. G. Ji, Y. Lin, T. Vincent, M. Maruyama, A. S. Aji, Y. Shiratsuchi, D. Ding, K. Kawahara, S. Okada, V. Panchal, O. Kazakova, H. Hibino, K. Suenaga, and H. Ago, *ACS Nano* **12**(10), 10032 (2018).

[118] H. F. Liu, S. L. Wong, and D. Z. Chi, *Chem. Vap. Deposition* **21**, 241 (2015).

[119] A. G. Rajan, J. H. Warner, D. Blankschtein, and M. S. Strano, *ACS Nano* **10**(4), 4330 (2016).

[120] W. Zhang, Y. Lin, Q. Wang, W. Li, Z. Wang, J. Song, X. Li, L. Zhang, L. Zhu, and X. Xu, *ACS Nano* **11**(10), 10608 (2017).

[121] D. Chandra, K. H. Lau, W. M. Chien, and M. Garner, *J. Phys. Chem. Solids* **66**, 241 (2005).

[122] Z. Wang, Y. Xie, H. Wang, R. Wu, T. Nan,Y. Zhan, J. Sun, T. Jiang, Y. Zhao, Y. Lei, M. Yang, W. Wang, Q. Zhu, X. Ma, and Y. Hao, *Nanotechnology* **28**, 325602 (2017).

[123] T. Kim, J. Mun, H. Park, D. Joung, M. Diware, C. Won, J. Park, S. Jeong, and S. Kang, *Nanotechnology* **28**(18), 18LT01 (2017).

[124] Y. Lai, C. Yeh, Y. Lin, and W. Hung, *Surf. Sci.* **519**, 150 (2002).

[125] M. Han, Y. Lou, N. Camillone, and R. M. Osgood Jr., *J. Phys. Chem. B* **104**, 65767 (2000).

[126] A. Baldan, *J. Mat. Sci.* **37**, 2171 (2002).

[127] I. M. Lifshitz and V. V. Slyozov, *J. Phys. Chem. Solids* **19**, 35 (1961).

[128] M. Zinke-Allmang, L. C. Feldman, and M. H. Grabow *Surf. Sci. Rep.* **16**(8), 377 (1992).

[129] C. Lunceford and J. Drucker *Rev. Sci. Instrum.* **89**, 125101 (2018).

[130] see tetech.com, https://tetech.com/product/tp-1/ for TP-1 Thermal Paste, tetech.com (2018).

[131] Thermoelectric Module Peltier Element Mounting Procedure, tetech.com, https://tetech.com/wp-content/uploads/2013/11/tem_thermoelectric_module_mounting _procedure.pdf (2007).

[132] see https://www.kjmagnetics.com/proddetail.asp?prod=B999 for B999, kjmagnetics.com (2018).

[133] R. R. Zarr, J. A. Chavez, A. Y. Lee, G. Dalton, and S. L. Young, NIST Heat Transmission Properties of Insulating and Building Materials, NIST Standard Reference Database Number 81, National Institute of Standards and Technology, Gaithersburg MD, 20899 (retrieved 2018).

[134] HP-119-1.4-0.8 Thermoelectric Module Specifications, tetech.com, https://tetech.com/wp-content/uploads/2013/11/HP-199-1.4-0.8.pdf (2018).

[135] HP-119-1.4-1.5 Thermoelectric Module Specifications, tetech.com, https://tetech.com/wp-content/uploads/2013/11/HP-199-1.4-1.5.pdf (2018).

[136] LC-SSX1Heat Exchanger, tetech.com, https://tetech.com/wp-content/uploads/2015/09 /LC-SSX1.pdf (2010).

[137] T. Sun and A. S. Teja, *J. Chem. Eng. Data* **48**, 198 (2003).

APPENDIX A

THERMOELECTRIC-COOLED LIQUID BATH CHILLER CAPABLE OF UNATTENDED OPERATION AT -28 °C

*This appendix has been published in *Review of Scientific Instruments* in 2018 [129].

A.1 Introduction

The capability to continuously cool a material or small experimental apparatus is often desirable. For example, reducing temperature can slow biological processes and chemical reactions. In our own work, we maintain solid and liquid chemical vapor deposition (CVD) precursors at temperatures in the -20 to -40 °C range in order to suppress their vapor pressures. This reduced vapor pressure provides increased control over the growth process. To study nucleation and growth of the transition metal dichalcogenides (TMDs) MoS_2 and WS_2, we load the CVD precursors into glass "bubblers" through which a carrier gas can be flowed. The carrier gas transports the precursors into the growth chamber where they pyrolyze on a heated sapphire substrate and form the target materials.

To achieve these reduced temperatures, we initially employed dry ice-cooled mixtures of methanol (MeOH) and H_2O as cold baths. As with many miscible substances, it is well known that diluting H_2O with MeOH lowers the freezing point of the mixture to a value determined by the MeOH:H_2O ratio. In the case of MeOH in H_2O, the freezing point can be varied from 0 °C for pure H_2O to -97.6 °C for pure MeOH. In this temperature range, dry ice (−78.5 °C) or liquid N_2 (-195.8 °C) is commonly employed to cool the mixture to its freezing point. Irrespective of the cooling additive, a dual phase, solid/liquid, "slurry" is ultimately achieved at the freezing point temperature of the mixture.

For our purposes, this method was initially adequate. However, systematic correlation of TMD film morphology with growth parameters necessitated deposition times in excess of 12 h. These extended deposition times required the tedious and continual recharging of the cold baths with dry ice to maintain their dual phase freezing point temperatures. Consequently, we searched for an alternative method to maintain the precursors at their optimum temperatures. Many chillers of various capacities are commercially available. Among the more common configurations are compressor-based liquid cold baths and immersion probe chillers. The liquid cold baths employ a compressor to refrigerate the bath while immersion probe chillers use a so-called 'cold-finger' probe submerged in the liquid to extract heat.

We were able to estimate the cooling capacity required for our application by monitoring the rate at which known volumes of dry ice were added to our thermally insulated 1:1 MeOH:H_2O mixture. Using the density and latent heat of sublimation of dry ice, we found that we needed to remove 15 W of heat from our cold bath to maintain its -40 °C temperature. Finding a commercially available chiller capable of maintaining this temperature, while removing the 15 W heat load was easy. However, given the relatively high cost of that option, we investigated the feasibility of employing thermoelectric elements to pump heat away from a liquid reservoir in which our sources could be submersed. Fabrication of the design described below cost roughly 1/5 of commercially available options.

Thermoelectric elements (TEs) are compact semiconductor devices that rely on the Peltier effect. The Peltier effect is a phenomenon that produces a temperature difference, ΔT, across a junction between dissimilar materials when a current is passed

through the device. Ours is a simple design that exploits this property to extract heat from a liquid reservoir, in which a small experimental apparatus can be immersed. The cold side of the TE was thermally bonded to the reservoir and the hot side was bonded to a liquid heat exchanger (LHE). Seeking to minimize the temperature of the bath, T_{bath}, we explored TEs of different heat-pumping capacities in addition to the use of 2 TEs mounted in a parallel configuration. We also explored the effect of varying experimentally accessible heat removal parameters: flow rate, temperature, and composition of the liquid flowed through the LHE.

The simple design presented here will enable straightforward adaptation of this concept to various applications requiring long-term, stable cooling of small experimental apparatus. We demonstrate that flowing 15 °C 'house' chilled water through the LHE enabled us to achieve a T_{bath} of -22 °C and hold it constant for days at a time. We further demonstrate that T_{bath} can be reduced to -28 °C by flowing an ethylene glycol:water mixture at 0 °C through the LHE. We anticipate that our TE-cooled chiller will provide liberation from the tedious necessity to continuously monitor liquid cooling baths, while providing a cost-effective alternative to commercially available options when long cooling times and highly consistent temperatures are needed.

A.2 Experimental Methods

Fig. A.1 shows a photograph (a) and simplified cross-sectional schematic (b) of our TE-cooled chiller. As stated above, applying a voltage to the TE creates a temperature difference across the element, creating a "hot side" and a "cold side", hereafter referred to as such. The hot side was thermally bonded to the LHE using zinc oxide thermal paste, obtained from TE Technology, Inc [130]. Thermal paste improves

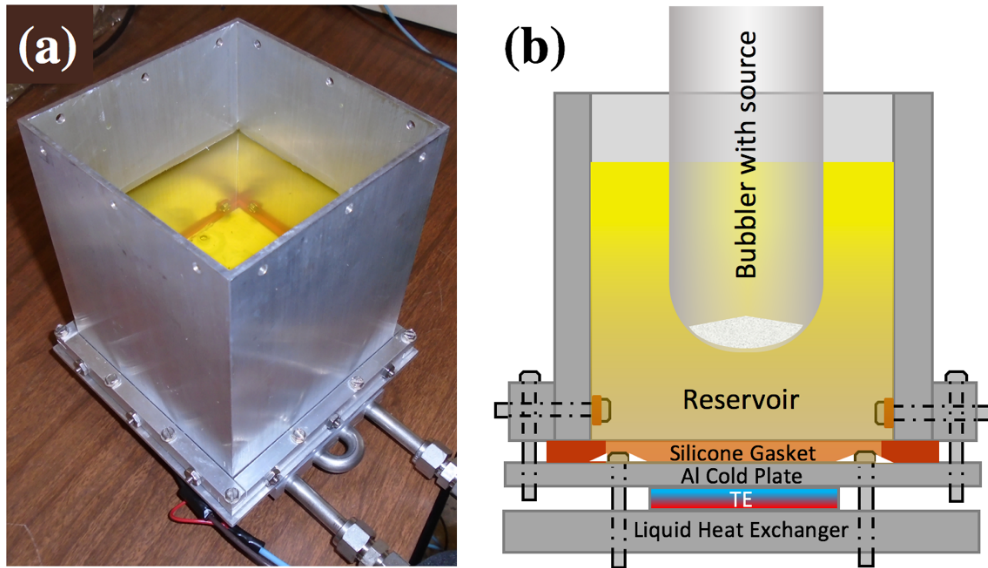

Figure A.1: (a) Photograph of the liquid bath chiller we designed, built and tested. The reservoir was filled with 1.5 L of a 2:1 ethylene glycol:water mixture, which is visible in the image. The metal tubing protruding beneath the lower right of the reservoir are the 3/8" diameter stainless steel tubes through which liquid was flowed through the liquid heat exchanger. Also visible at the bottom of the image are the electrical leads that powered the TE. (b) Cross-sectional schematic of our liquid bath chiller with a source bubbler submerged in the bath.

the thermal contact between the TE and the LHE, maximizing heat conduction away from the hot side of the TE. The cold side was likewise bonded an Al "cold plate" that formed the base of the reservoir. The cold plate and heat sink were then bolted together to the torques specified in the TE Technology application notes [131], with the TE(s) sandwiched between. Thermally insulating fiber shoulder washers were used to isolate the clamping bolts from the LHE to reduce thermal conductance.

The reservoir was built with the Al cold plate as a base. The walls were formed by a 6" length of 5" square aluminum tubing bolted to a collar that was in turn bolted to the cold plate. To prevent leaks, a home-made silicone gasket was compressed between the cold plate and the square aluminum tubing. Bolt holes below the fluid level were sealed using silicone O-rings. Those bolt holes in the cold plate used to secure it to the LHE were sealed with silicone putty.

The reservoir was filled with 1.5 L of a 2:1 ethylene glycol:H_2O mixture. The freezing point of this mixture is approximately -55 °C, which guaranteed that it would not freeze at the lowest reservoir temperatures we achieved. The liquid was continuously stirred using a neodymium-iron-boron stir bar to maintain a uniform temperature and bath composition. Because of the relatively large distance between the stir-bar and the bottom of the heat sink, commercially available stir-plates were unable to continuously stir the bath. This obstacle was overcome by custom fabricating a stirring apparatus. Two 9/16" cube, high strength neodymium-iron-boron magnets from K&J Magnetics [132], were attached 3" apart on a 4" long by 2" wide Sn strip that was mounted to a salvaged computer fan. The rotational speed of the fan was controlled using a Variac. This home-made stirring apparatus was positioned directly under the LHE and was able to

continuously stir the bath from its position 3" below the cold plate. T_{bath} was measured using a bare K-type thermocouple submersed in the bath at its geometric center. The time to achieve a minimum temperature from room temperature (RT) using only the TE for cooling was approximately 8 h, but cooling could easily be accelerated by the addition of dry ice.

Heat conduction from the ambient was reduced using polyurethane "foam rubber" for insulation. Many materials are available for insulation, but polyurethane was selected because of its low thermal conductivity, ranging from 0.0328 to 0.0495 W/(m·K) [133], depending on the bulk density, and its ready availability. The vertical walls of the reservoir were insulated using a 3" thick sheet, the cold plate and the LHE were insulated with a 1" thick sheet and a 2" thick sheet was used to cover exposed areas of the bath on the top of the reservoir. The data presented below was acquired with no thermal load to the bath, but temperature minima were verified to be unchanged with a 1.6" diameter glass tube submerged in the bath, as schematically depicted in Fig. A.1(b). To simulate actual growth conditions, we flowed 20 sccms of Ar through the tube (1 sccm represents a flow of 1 cubic centimeter per minute at 0 °C and atmospheric pressure). Using the specific heat of Ar and the 300 Torr pressure we employ during growth, this equates to a thermal load of approximately 8.9 mW.

The Bi_2Te_3 TEs used were purchased from TE Technology, Inc. We investigated the performance of two different elements: HP-199-1.4-0.8 [134], and HP-199-1.4-1.5 [135]. Potted elements were chosen over unpotted elements to avoid water absorption into the element as a consequence of condensation from the ambient. Per the manufacturer's data sheets, a single HP-199-1.4-0.8 is capable of removing

approximately 90 W of heat at a ΔT of 20 °C when operated at its optimum performance parameters. A single HP-199-1.4-1.5 is capable of removing approximately 58 W at the same ΔT. Because of this difference in the potential for heat-removal of these elements, we designate the HP-199-1.4-0.8 as high capacity (HC), and the HP-199-1.4-1.5 as low capacity (LC) TEs in the discussion that follows. Both of these elements are 40 mm square. The HC is 3.2 mm thick while the LC is 3.6 mm thick. In terms of heat removal, both of these are well above the 15 W calculated necessary for our application.

To pump heat, the TEs must be powered, which generates waste heat. At the maximum heat-pumping capacity, at a ΔT of 20 °C, the HC generates 340 W of waste heat [134], compared to 210 W for the LC [135]. This waste heat must be removed by the LHE from the hot side of the TE in addition to that removed from the reservoir. In addition to investigating single HC and single LC configurations, we also investigated mounting two of the HC or two of the LC elements in a side-by-side geometry in order to increase their contact area with the LHE to more effectively remove heat. An added benefit to this strategy is that in this "dual HC" or "dual LC" configuration the heat pumping capacity of a single element could be obtained at slightly lower waste heat generation. When two of a given element were used in a dual configuration, they were mounted approximately 4 mm apart, each with their "cold side" thermally bonded to the Al cold plate and the "hot side" bonded to the LHE. In total, we investigated 4 separate TE configurations: single and dual HC, as well as single and dual LC.

Preliminary testing was done using a single HC TE bonded to an air-cooled heat sink cooled by salvaged computer fans. The minimum obtainable cold plate temperature, 7 °C, was deemed unacceptable, and at maximum input power, an increase in the cold

plate temperature above RT was observed. This result indicated that a better method of heat transfer away from the hot side of the TE was needed. The LC-SSX1 heat exchanger, from TE Technology, Inc., was selected because of its exceptionally low thermal resistance, 0.04 K/W, above a liquid flow of 2.4 L/min, using H_2O at temperatures greater than 15 °C [136]. During data acquisition, the flow rate of liquid through the LHE was continuously monitored using a King 3C-08 in-line flow meter plumbed to the outlet of the LHE.

Investigation of how the temperature of the liquid flowing through LHE affected T_{bath} was accomplished using a Neslab RTE-111 recirculating chiller (RC), filled with a 1:2 ethylene glycol:H_2O mixture. The RC was plumbed to the LHE using 3/8" diameter polyethylene tubing insulated with 1" thick EPDM rubber tube insulation. We investigated RC chiller temperatures of 25 (roughly RT), 15, and 0 °C. Flow from the RC was held constant at 4.7 L/min, as increasing the flow beyond this point proved to have an insignificant impact on the minimum achievable temperature, as is discussed in detail below.

Many laboratories are equipped with some form of house chilled water supply. For this reason, we also tested our design using the house chilled water lines in our lab. The same 3/8" diameter insulated plumbing and flow measurement described above were used. House chilled water in our laboratory is maintained at 15 °C and is capable of a maximum flow of 9.8 L/min through our apparatus. Due to the higher flow afforded us by the house chilled water system, this set-up was used to investigate the effect of flow rate through the LHE on the minimum achievable T_{bath}. Flows from 2.6 to 9.8 L/min were investigated.

Over long running times, water condensation from the ambient caused a layer of ice to build up between the LHE and cold plate. While this ice layer did not have a measurable impact on T_{bath} during the longest runs investigated, 10 days, it is likely that repeated freeze-thaw cycles could compromise the mechanical integrity of the chiller or that the electric and thermal conduction pathways created by the ice layer could become problematic. To mitigate this difficulty, the chiller was enclosed in a plastic bag, and the air evacuated using a shop vacuum. Small gaps in the plastic at the liquid and electrical feedthrough outlets were sealed with duct tape. After this preparation, 10 days of continuous use at T_{bath} = -28 °C resulted in only a thin layer of frost on the reservoir, with no observable condensation on the cold plate or LHE. An alternative method of "floating" the plastic bag by providing a slow and continuous flow of He from the ground up also proved to be a very effective strategy for mitigating ice build-up.

Over 10 days of continuous use, we observed no fluctuation in bath temperature. The minimum bath temperatures we investigated were achieved at an input power of only 83% of the 150W max input power specified by the manufacturer. As the thermoelectric is a solid-state device with no moving parts, and since we were able to achieve our minimum temperatures at less than the maximum operating power, we expect our design to be reliable and consistent far beyond the 10 days investigated here.

A.3 Results and Discussion

We first identified which of the 4 TE configurations investigated yielded the lowest T_{bath}. For this facet of our investigation, we employed the Neslab RTE-111 RC to circulate a 1:2 ethylene glycol:water mixture at T = 0 °C through the LHE, while monitoring T_{bath} as a function of input power to the TE element(s). These results are

presented in Fig. A.2, below. Subsequent to identifying which of the TE configurations provided lowest T_{bath}, we used that configuration to explore the effect of the other experimentally accessible parameters on T_{bath}.

Fig. A.2 shows T_{bath} as a function of total power to the TE(s) for each of the 4 TE configurations. It shows that the LC TEs are able to achieve lower bath temperatures than the HC TEs. Focusing on the HC curves, we see that the minimum in the single curve is 4 °C lower than the lowest T reached by the dual configuration. The single LC TE curve behaves similarly, exhibiting a minimum before T_{bath} increases at higher input powers. This phenomenon is discussed below. Fig. A.2 shows that the dual LC configuration yields the lowest T_{bath} of -28 °C. Consequently, exploration of other experimentally accessible parameters was performed using the dual LC configuration.

The difference in shape between the dual TE and single TE configurations merits further discussion. As stated above, both single configurations show a rise in T_{bath} after a minimum is achieved. This rise indicates that, in the single configurations, waste heat is not adequately being transported away via the smaller footprints of contact with the LHE compared to that of the dual configurations. In the dual configurations, on the other hand, this rise in T_{bath} was not observed. Instead, increasing the power supplied to the dual configurations to values greater than those plotted in Fig. A.2, we observed an increase in the RC temperature without any rise in T_{bath}. No data at an increased RC temperature is presented in Fig. A.2. This difference in behavior supports the supposition that the larger contact area between the dual TE configuration and the LHE allows for more effective heat transport from the TE into the RC, which overwhelms the heat-pumping capacity of the RC before any rise in T_{bath} is observed.

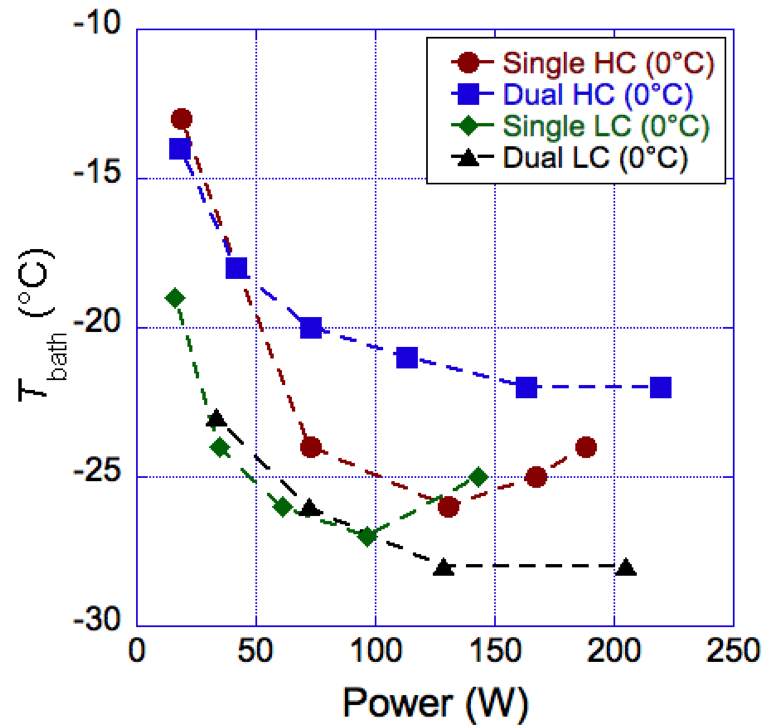

Figure A.2: T_{bath} vs. total power dissipated in the TE(s) for the 4 different TE configurations investigated. The data was acquired while flowing 1:2 ethylene glycol:H_2O at 0°C through the LHE at a flow of 4.7 L/min.

Having selected the TE configuration that gives the lowest T_{bath}, we investigated the effect of parameters that affect heat transport away from the TEs. Fig. A.3(a) shows T_{bath} as a function of total power for the dual LC configuration, at the RC temperatures 0, 15 and 25 °C. Data for this figure was obtained at a flow of 4.7 L/min through the LHE. The curves labeled 'RC' and plotted with solid lines were acquired with a 1:2 ethylene glycol:water mixture flowing through the LHE. Decreasing the RC temperature from 25 °C to 15 °C lowers T_{bath} by 5 °C. A further 13 °C decrease in T_{bath} is obtained by decreasing the RC temperature to 0°C. This result indicates a strong dependence on the temperature of liquid flowed through the LHE and the likelihood that a further decrease in RC temperature would yield an even lower T_{bath}. Our RC, however was not able to maintain lower temperatures under such a large heat load, so, lower RC temperatures could not be investigated.

Fig. A.3(a) also shows T_{bath} as a function of power for the dual LC configuration flowing house chilled H_2O at 15 °C through the LHE. The 7 °C difference between this curve and that for the RC at 15 °C flowing the 1:2 ethylene glycol:water mixture warrants discussion. A simple verification of this result was performed using the RC with pure water at 15 °C. This test gave T_{bath} values identical to those obtained with the house chilled water. Consequently, we conclude that pure H_2O is more effective at transporting heat away from the reservoir than the ethylene glycol:water mixture. This behavior is likely due to the difference in thermal conductivity between the ethylene glycol:water mixture and pure water, 0.429 and 0.547 W/(m·K) respectively [137]. The ethylene glycol:water mixture was chosen because we wanted to investigate temperatures at and

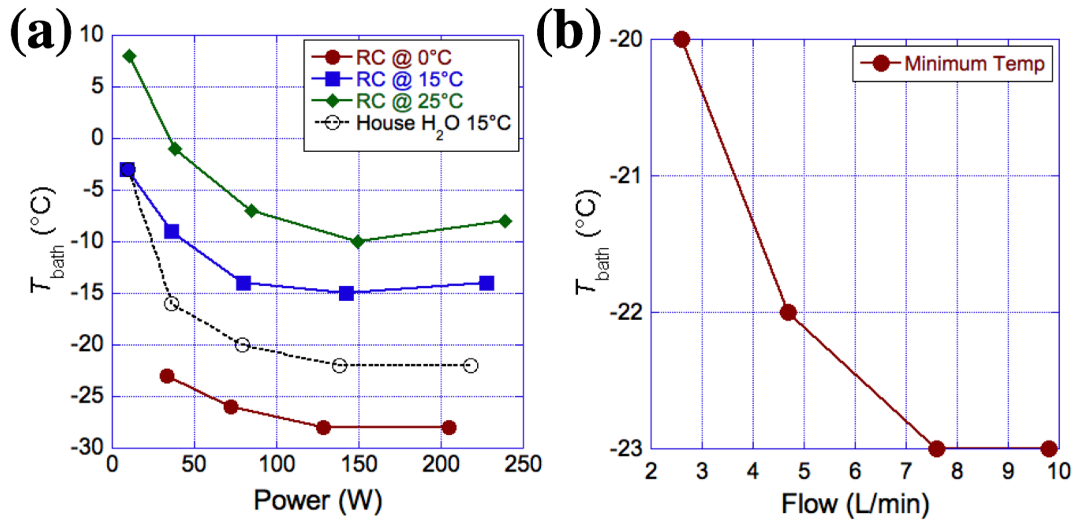

Figure A.3: (a) Plots T_{bath} vs. total power for the dual LC configuration using a 1:2 ethylene glycol:water flow of 4.7 L/min with the RC bath at 0, 15 and 25 °C. Also plotted is T_{bath} obtained while flowing house chilled water at 15 °C using the same flow rate. (b) Plots minimum T_{bath} vs. flow for the dual LC configuration using the house chilled water at 15 °C.

below the freezing point of water. At 15 °C, however, we are well above the freezing point of water and can use pure H_2O as the thermal transport liquid.

The minimum bath temperature vs. flow is shown in Fig. A.3(b). For this part of the investigation, we employed the dual LC configuration and house chilled water at 15 °C. This figure shows that by doubling the flow from the 4.7 L/min used above, the minimum is decreased by only a single degree. By reducing the flow by the same factor, the minimum is increased by 2 °C. For our purposes, this result demonstrates a very weak dependence on flow rate, so long as flows greater than 2 L/min can be used. Fig. A.3(b) is in qualitative agreement with the manufacturer's data sheet for the LC-SSX1 heat exchanger, which shows that its thermal resistance does not vary significantly for flows > 2.0 L/min at similar temperatures [136].

A.4 Conclusion

Our implementation of a thermoelectric-based liquid bath chiller is inexpensive, easy to fabricate and stably maintains temperatures normally achieved by dry ice, or liquid N_2 cooled liquid baths, while running unattended for days at a time. We have demonstrated the effect of TE capacity and configuration on the minimum achievable bath temperature. We found that parameters related to the LHE that removes heat from the hot side of the TE were key to reducing the chiller bath temperature. We explored the effects of flow rate, composition and temperature of the thermal transport liquid flowing through the LHE. Of these thermal transport liquid-related parameters, liquid composition and temperature were shown to have the greatest impact in reducing the bath temperature. We anticipate that these results will enable similar TE-based chillers to be

implemented in a variety of applications that require stable, long-term cooling of small experimental apparatus.